Continuum Level Physics-based Model on Understanding and Optimizing the Lithium Transport in High-Energy-Density LIB/LMB Electrodes

Zeyu Hui

Submitted in partial fulfillment of the
requirements for the degree of
Doctor of Philosophy
under the Executive Committee
of the Graduate School of Arts and Sciences

COLUMBIA UNIVERSITY

2022

Abstract

Continuum Level Physics-based Model on Understanding and Optimizing the Lithium Transport in High-Energy-Density LIB/LMB Electrodes

Zeyu Hui

As an efficient means of energy storage, rechargeable batteries, especially the lithium-ion batteries (LIBs) have been a vital component in solving the upcoming energy crisis and environmental problems. Recently, the development of electric vehicle market puts new requirement on the next generation LIBs, including superior energy density, safety and cycling stability, etc. Compared with experimental investigation, Physics-based models provide a surrogate method to not only tackle the underlying physics of the complex battery system, but also optimize the design of battery systems. In this thesis, I will show how I use the physics-based continuum model and cooperate with some experimental methods to understand the lithium transport phenomena inside the multiscale battery electrode systems, based on which the models are then applied to guide the experimental optimization of battery electrode design and to quantitively understand the degradation of high-performance electrodes.

The thesis is divided into three parts. First part (Chapter 2) presents a systematical model selection study on the multiscale $LiNi_{0.33}Mn0_{.33}Co_{0.33}O_2$ (NMC_{111}) electrode. Discharge and voltage relaxation curves, interrogated with theory, are used to distinguish between lithium transport impedance that arise on the scale of the active crystal and on the scale of agglomerates (secondary particles) comprised of nanoscale crystals. Model-selection algorithms are applied to determine that the agglomerate scale transport is dominant in the NMC_{111} electrode studied here.

This study not only discovers the dominant length scale for lithium transport, but also provide a validated model (the agglomerate model) for later study.

The second part (Chapter 3 & 4) talks about understanding & optimization of ion transport in porous electrodes. In Chapter 3, multi-scale physics-based models for different active material systems, which have been parameterized and validated with discharge experiments, are optimized by varying porosity and mass loading to achieve maximum volumetric energy density. The optimization results show that with a re-scaling of the current rate, the optimal results follow a general design rule that is captured in a convenient correlation. Chapter 4 extends the model to simulate the performance of advanced electrode architectures utilizing aligned channels, by quantifying the impact of aligned channel electrode structures on cell rate capability. Then the optimization algorithm in Chapter 3 is applied to these aligned-channel electrodes.

The final part (Chapter 5) shows how I use the physics-based model to quantitatively analyze the battery degradation. The validated model is applied to cycling data to obtain parameter estimates indicative of degradation modes. It's found that growth rates of interfacial impedance and active material loss are greater at 4.5 V, as might be expected. However, when charged to 4.5V, degradation rates are lower at a cycling C-rate of 1.0 h^{-1} than at 0.5 h^{-1}. Once performance changes are quantified, we use further simulation to evaluate the contribution of individual degradation modes to fade of cell performance metric such as capacity, power density, and energy density.

Table of Contents

List of Figures

List of Tables

Acknowledgments

First, I would like to thank my advisor, Dr. Alan C. West for the opportunity he gave me and his great patience, guidance, encouragement, and support on my research. During the past 4 years working with him, I learned a lot not only on scientific research skills, but also on communication, handling multiple tasks, and dealing with pressure. I also want to thank my co-advisor, Prof. Yuan Yang for bringing me into the battery field, for the help during my 1st year at Columbia and for the guidance on both research and life.

I would like to thank my family. I'd acknowledge my beloved wife Xu Yi for the companionship. I will never forget the ups and downs we spent together here in Columbia and back in China. I'd like to thank my parents, my father Lining Hui and mother Lihong Zhang and all other family members, for the numerous loves, encouragement, and guidance during the past 27 years, which allows me to chase this goal that I've never thought possible before.

I would like to thank Prof. William E. Bailey, Prof. Chris Marianetti and Prof. Alexander Urban for being my Ph.D. defense committee members. My acknowledgement also goes to all the professors that I took courses with, including Prof. Katayun Barmak, Prof. Chengjun Chen, Prof. James Im, Prof. William E. Bailey, Prof. Yuan Yang and Prof. Alan C. West. I believe the knowledge & skills they've passed to me will be a lifetime fortune.

I would like to thank the whole West group and Yang group. I'd like to acknowledge the tutoring from Dr. Nicholas W. Brady, Dr. Haowei Zhai and Pengcheng Yao. I would like to thank all the current/former group members, including Karthik Malyivahanan, Dr. Jon Vardner, Ryan Gusley, Rob Mohr, Mateo Williams, John Bernard, Kedi Hu, Cem Komurcuoglu, Charles Kim, Tianwei Jin, Dr. Qian Cheng, Dr. Aijun Li, Dr. Bingqing Xu, Dr. Bin Zhu, Dr. Xue Wang, Dr.

Wenlong Huang, Dr. Guoyu Qian, Tianyao Gong, Tianyang Wang, Qingquan Song, etc., for the discussion, cooperation, and assistance.

I would like to thank my collaborators, including Prof. Guihua Yu, Xiao Zhang and Zhengyu Ju from University of Texas Austin, Prof. Esther Takeuchi and Prof. Amy C. Marschilok from Stony Brook University for providing the excellent experimental observations, without which I cannot show the power of my model.

Finally, I would like to thank the precious friends I have made here at Columbia: Tianwei Jin, Bonan shen, Karthik Malyivahanan, Jon Vardner, Nick Brady, Zhexi Lin, Zhengyan Zhang, Xueqi Peng, Qi Zhang, Pengcheng Yao, Wenlong Huang, Qian Cheng, Wei Cao, Xiaoyan Huang, Songsheng Tao, Krystian Ganko, to name but a few.

Chapter 1: Introduction

With the surging demand of energy and rapidly depleted fossil fuel storage, the upcoming energy crisis urges large-scale adoption of renewable energy. However, renewable energy resources such as solar and wind are strictly constrained by location and are intermittent over time. Same features (non-uniform distribution and time intermittence) apply to the demand side, making it necessary to design devices that can store/release energy over time and distribute energy over space. As a means of energy storage device, rechargeable batteries, especially the lithium ion batteries (LIBs) are regarded as one of the most feasible and efficient solution, thus has gained wide application for both small-scale and large-scale utilizations.

1.1 About Battery and Lithium-ion Battery (LIBs)

1.1.1 History of Rechargeable Batteries[1, 2]

Back to 1800, Alessandro Volta designed the first electrochemical cell with Zinc and Copper, providing current through Zn oxidation and CuO reduction. Such cell converts chemical energy to electrical energy through electrochemical reactions, but the reaction is generally not reversable, making it a 'single-use' device, also called 'primary battery'. To reversibly store and release energy, Ritter pioneered the development of 'secondary (rechargeable) battery' by showing water electrolysis. Following the original discoveries, in 1850s, Wilhelm Sinsteden and Gaston Planté invented the first commercial rechargeable battery, lead-acid battery, which provides a voltage of ~ 2V through oxidizing Pb and reducing PbO_2 to $PbSO_4$, such cell has been widely adopted from its invention due to the low cost and long cycle life, despite the low energy density (20-40

Wh kg^{-1}). Inspired by the early invention, nickel-based cells, including Ni-Cd battery and Ni-Fe battery was invented, which finally enables the commercialization of Nickel-Metal Hydride (Ni-MH) battery in 1989 with improved energy density (70-100 Wh kg^{-1}). At the same time, another type of battery, the lithium-ion batteries (LIBs) came into market at the same time, characterized by much higher energy density.

1.1.2 About Lithium-ion Battery

Owing to its low equivalent weight (atomic weight = 6.94, converts to specific capacity of 3968 mAh g^{-1}) and low redox potential (-3.05V vs. SHE), the lithium chemistry has been adopted by the battery development starting from 1970s, at which time lithium metal was used as anode for primary cell, coupled with cathode such as I_2, CF_x.[3] In the late 1970s, a breakthrough towards rechargeable lithium battery was achieved by Whittingham with the discovery of 'intercalation' material such as TaS_2 and TiS_2. In 1976 he created the first rechargeable lithium battery with Li metal as anode and TiS_2 as cathode[4]. During cycling, the lithium ion can reversibly intercalate into and de-intercalate from the TiS_2 cathode, producing a voltage of ~2.2V. Four years later, Goodenough and co-workers discovered the layered transition-metal oxide cathode, such as $LiCoO_2$,[5] which severs as an important type of LIBs cathode even for today. In 1987, Yoshino and co-workers[6] at Asahi Kasei Corporation adopted the previous reported lithium battery breakthroughs and produced the first so-called 'Lithium-ion battery', in which system lithium ions shuttle between a layered $LiCoO_2$ cathode and a carbonaceous material anode, producing an operating voltage of ~3.6V and specific energy of ~ 80 Wh kg^{-1}. Such 'rocking chair' configuration

was optimized and commercialized by SONY in 1991[7], and has been serving as the classic LIBs model for the past 30 years.

1.2 Electrical Vehicle Market & Next Generation LIBs

As a viable means to solve the issue related with internal combustion engine vehicles (ICEVs), such as emissions of greenhouse gases and shortage in fossil fuel supply & storage, Electric Vehicles (EVs) starts to be accepted by the market in 2010s[8]. Although the past decade remarks a surge in EV market, additional efforts on the Electric Vehicle Battery (EVB) improvement are needed to really 'electrify' the transportation sector. For example, safety is a big concern for the state-of-the-art EVB, since it normally contains combustible organic liquid electrolyte and is easy to catch fire, even leading to explosion during the thermal runaway process. Moreover, to cut the cost of current EV and prolong its mileage, further improvement in battery energy density (specific energy & volumetric energy density) is crucial. Note here, that the improvement in battery energy density shouldn't be accompanied by the tradeoff of reduced cycle life.

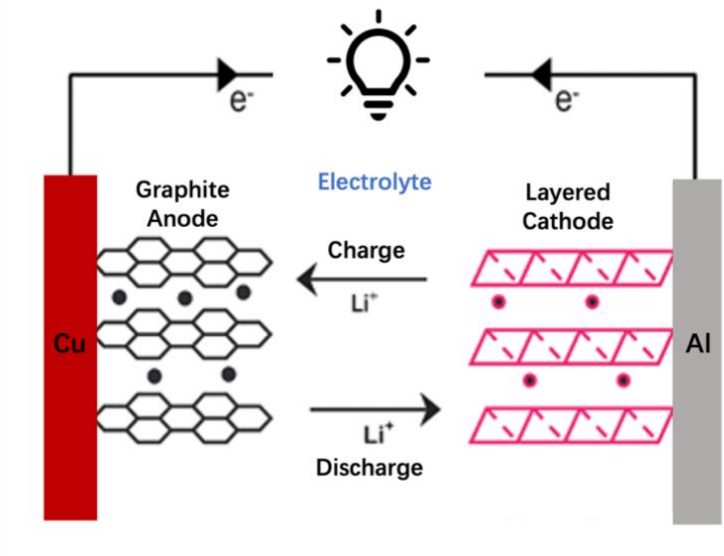

Figure 1.1 Configuration of the commercial Lithium-ion-batteries (LIBs)

There are generally two routes towards improved battery energy density. The first way is to replace the components of traditional LIBs with new chemistry. As Figure 1.1[9] shows, current LIBs normally use an intercalation cathode (positive electrode) and graphite anode (negative electrode). Organic liquid electrolyte (e.g., $LiPF_6$ in DE/DEC) is used to transport Li-ion. To improve cell energy density, the first choice is to replace the porous graphite anode by a metallic lithium[10], which improves the anode specific capacity by ~ 10-fold. In the meantime, replacing the cathode material by energy-denser material, such as sulfur (Li-S battery), could further increase cell energy density. However, reduced cycle life is often observed in these new material systems. Understanding the degradation mechanism/modes is crucial for application of the new material systems. In Chapter 5, I will show how the modeling approach is used to quantify the degradation modes of high-voltage cathode.

In addition to new materials discovery, optimizing the design of current material system could also effectively improve the cell-level energy, with additional advantage of preserving good cycle life of the mature material system. As a multi-scale system, the state-of-the-art porous battery electrodes could enable fast lithium intercalation/de-intercalation reaction by opening up more active surface area. However, such configuration creates impedances for lithium transport on multiple length scales. If we can understand the Li transport physics on different length scales, designing thick electrodes with minimum mass transport losses will be an efficient shortcut towards improved cell energy density.

1.3 Continuum-level Physics-based Model

Modeling approaches have been an important means for understanding the physics of LIBs and improving performance, with intrinsic advantage of lost cost, good reproducibility, etc. In

1990s, Newman et al.[11, 12] developed the continuum physics-based model, also called 'DFN' model, which uses differential equations (Governing Equations) to describe the electron/mass transport and reactions inside porous electrode, on the meso length scales of electrode thickness & active material particles. With input information of microscopic material properties such as open-circuit-potential and lithium diffusivity, the model has been proven to precisely simulate the macroscopic cell performance, such as charge/discharge voltage and lithium concentration profiles. With modification to the original 'DFN' model, we could apply the continuum-level physics-based model to different studies on battery research.

In this dissertation, I will focus on understanding and improving energy density and cycling stability of state-of-the-art lithium battery system. I will show how I use the experimentally validated physics-based model to understand the lithium transport phenomena inside the multiscale battery systems, to analyze the lithium transport in electrodes with advanced architecture, and then to optimize electrode design towards maximum energy density and to interpret battery degradation modes

Chapter 2: Determining the Length Scale of Transport Impedances in Li-ion Electrodes: $Li(Ni_{0.33}Mn_{0.33}Co_{0.33})O_2$*

*This work has been published: Hui, Zeyu, Karthik S. Mayilvahanan, Yuan Yang, and Alan C. West. "Determining the length scale of transport impedances in li-ion electrodes: Li ($Ni_{0.33}Mn_{0.33}Co_{0.33}$) O_2." Journal of The Electrochemical Society 167, no. 10 (2020): 100542.
The thesis writer's contribution was t model development, experimental design, data analysis and paper writing.

2.1 Introduction

Lithium-ion Batteries (LIBs) have garnered great research attention and wide commercial applications as energy storage devices on portable devices and electric vehicles (EV). [13, 14] However, the optimization of LIBs for energy and power density is still an active research area.[15, 16, 17, 18] For instance, compared with the graphite anodes (~ 372 mAh/g in specific capacity), cathode materials are lower in capacity (< 250 mAh/g)[19]. There are attempts to increase cathode mass loading (mass or capacity per area) by increasing cathode thickness or reducing porosity (roll pressing),[20] while others focus on increasing the upper limit of the voltage window, in order to gain more capacity from the cathode.[21] In both cases, transport of lithium and homogeneity of lithium intercalation/de-intercalation reaction may be crucial to battery performance.[22]

During battery operation, these processes occur at multiple length scales. Lithium ions inside liquid electrolyte diffuse through porous constructs[23], and lithium within the crystal diffuses between the surface and the center .[24] Meanwhile, charge-transfer reactions occur at the surface of the electrode material and electrolyte.[25] Any of the processes may be the performance limiting step depending on chemistry, mode of operation, and design. Accordingly, understanding the detailed mechanism and the impedance of every process is key to improve the design of batteries.

Physics-based mathematical models play an important role in data analysis. Newman *et al*[11, 12] developed an approach to couple the electrode and crystal scales. Such models have been used to answer questions that are hard to be fully understood by experiment alone. For example, Srinivasan et al[26] developed a model for a lithium iron-phosphate electrode to understand the sources of energy loss at different power densities. Brady et al[27] built a model for lithium trivanadate (LiV_3O_8) electrode using method developed by Newman but foregoing the use of a superposition integral formulation on the crystal scale in favor of a more flexible numerical

algorithm which allows inclusion of more physics. They obtained the diffusion coefficient of lithium in LiV_3O_8 and determined that transport processes within the crystal appear to be more rapid during charge than discharge.

Compared with other cathode materials, the layered transition-metal oxide $Li(Ni_xMn_yCo_{1-x-y})O_2$ (NMC) is attractive for electric vehicles because of its moderate cost and high energy density.[28, 29] As Figure 1.1a,b shows, an NMC cathode has a hierarchical structure. The ~ 400 nm primary NMC crystals tends to form spherical agglomerates with an average diameter of ~ 10 μm. Yang et al[30] used focused ion beam (FIB) to lift out NMC crystals and used EDS to observe the chemical constitutions on the crystal surfaces. The strong phosphorus signal on the grain boundary conclusively showed that the electrolyte penetrates the inside of agglomerated crystals, and the Li oxidation/reduction reaction occurs at the surface of each of the small crystals instead of at the outer edge of the agglomerate.

In addition to transport across the bulk electrode (electrode scale), there are two length-scales that may impact the transport process: the transport of lithium ion (Li^+) throughout the agglomerate (agglomerate scale), and the diffusion of Li inside NMC crystal (crystal scale). Commonly, researchers in modeling couple the electrode scale to either the agglomerate or crystal scales, but it may be difficult to know which length scale to use. If a diffusion coefficient is independently known, the characteristic times associated with potential relaxation may prove insightful[31]. Often the diffusion coefficient is not known with certainty. Furthermore, agglomerate-scale transport processes have important characteristics that are not always captured with a crystal-scale model, especially at high rates. This may not always be accounted for, and this can impact conclusions as discussed here. Since the characteristic length of the two scales may be vastly different,

interpretation of relaxation times in GITT experiments may lead to a very large variation in literature-reported diffusion coefficients.

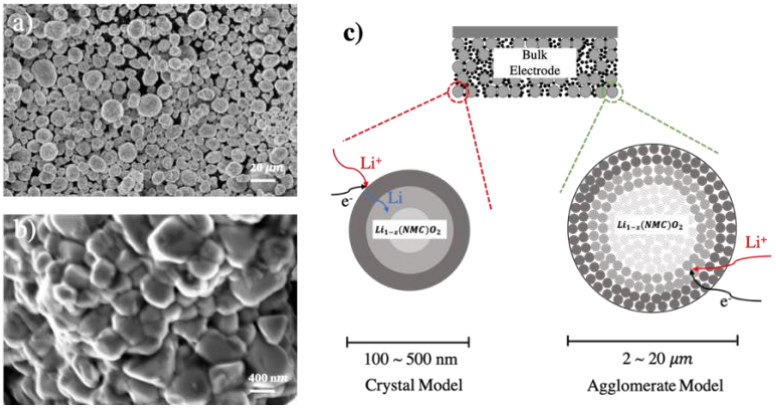

Figure 2.1 (a, b) SEM images of NMC_{111}; (c) Schematic of the assumptions of crystal model and agglomerate model, in which the limiting transport process occurs on the crystal and agglomerate length scales separately.

To determine the more important transport process, this study compares both electrode-agglomerate scales coupled mathematical model (agglomerate model) and electrode-crystal scales coupled model (crystal model) to experimental results. As Figure 2.1c shows, in both models, the assumption is made that the transport process on the other scale is fast enough, and the resulting impedance is negligible. Both models are compared under multiple current rates, and model-selection algorithms are used to identify the most important length scale in an electrode construct, at least from the point of view of transport limitations. In other words, the efficacy of models derived from hypothesizing crystal-scale transport limitations are controlling are compared to models derived from hypothesizing agglomerate-scale transport limitations are controlling.

2.2 Theory

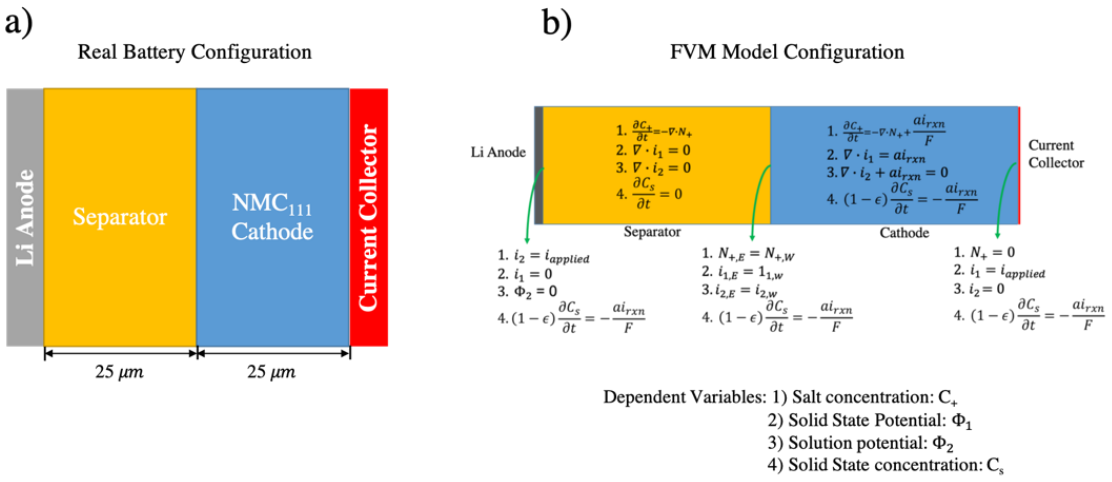

Figure 2.2 (a) Configuration of real battery. (b) Configuration of physical based continuum model, with electrode scale governing equations and boundary conditions.

2.2.1 Mathematical Model

Figure 2.2a shows the configuration of the coin cell used in this study. Two models were developed following the development by Knehr[32] et al and Brady et al.[33] In order to eliminate the electrode-scale transport limitations, thin $LiNi_{0.33}Mn_{0.33}Co_{0.33}O_2 (NMC_{111})$ cathodes (25 μm, mass loading $= 2.84\ mg/cm^2$) were used in the experimental study and in the present analysis. Both scaling arguments and simulations confirmed that electrode-scale effects were negligible.

Nevertheless, a so-called pseudo 2D modeling paradigm[34] was used to most easily connect the smaller-length scale simulations to the parameters that are controlled during fabrication. Equations describing transport of lithium inside the NMC agglomerate or crystal are coupled to the electrode scale equations. As shown in Figure 1c, in the crystal model, we assume that the transport through agglomerates is fast and do not contribute to voltage loss, thus the agglomerate scale transport loss is neglected. In contrast, crystal scale transport loss is neglected in the

agglomerate model. All the coupled equations are solved simultaneously using the BAND(J) algorithms,[35] which gives values of dependent variables as a function of position and time. Detailed governing equations and boundary conditions are shown in Table 2.1. The coefficients for the reversible potential in Table 2.1, equation (11) was obtained by fitting the expression to experimental GITT (C/10) data taken after one hour of relaxation at 11 different state of discharge. While both models describe similar physics, there are differences. For example, the description of the interfacial reaction kinetics appears as a boundary condition in a crystal-scale model but in the governing equation of an agglomerate-scale model.

Table 2.1: Governing equations and boundary conditions for mathematical model of NMC cell.

Electrode Scale Equation

	Governing Equation	Li Anode	Separator Edge	Current Collector
(1) Solid State Current (i_1)	$(1-\epsilon)\sigma\nabla^2\Phi_1 - ai_{in} = 0$	$i_1 = 0$	$\nabla \cdot i_1 = 0$	$i_1 = i_{applied}$
(2) Electrolyte Current (i_2)	$\nabla \cdot (\kappa\nabla\Phi_2) + \epsilon F(z_+D_+ + z_-D_-)\nabla^2 c_0 + ai_{in} = 0$ $(\kappa = \epsilon F^2(z_+^2u_+ + z_-^2u_-)c_0)$	$\Phi_2 = 0$	$\nabla \cdot i_2 = 0$	$i_2 = 0$
(3) Electrolyte Concentration (c_0)	$\epsilon\frac{\partial c_0}{\partial t} = -\nabla \cdot N_+ + \frac{ai_{in}}{F}$ $(N_+ = -D_+\nabla c_0 - \frac{F}{RT}z_+D_+c_0\nabla\Phi_2)$	$N_+ = \frac{i_{applied}}{F}$	$\nabla \cdot N_+ = 0$	$N_+ = 0$
(4) Solid State Concentration (c_s)	$(1-\epsilon)\frac{\partial c_s}{\partial t} = -\frac{a \cdot i_{in}}{F}$	-	-	-

Crystal Scale Equation

	Governing Equation	Crystal Center	Crystal Edge
(5) Lithium balance (${c_s}^x$)	$\frac{\partial {c_s}^x}{\partial t} = D_x\nabla^2{c_s}^x$	$\nabla {c_s}^x = 0$	$-D_x\nabla {c_s}^x = \frac{i_{in}}{F}$

Agglomerate Scale Equation

	Governing Equation	Agglomerate Center	Agglomerate Edge
(6) Solid State Current (i_1^{agg})	$\nabla \cdot i_1^{agg} = a^{agg}i_{in}^{agg}$ $(i_{surface,agg} = \frac{\partial C_s}{\partial t}FV_{agg}(1-\epsilon_{agg})/A_{agg})$	$i_1^{agg} = 0$	$i_1^{agg} = i_{surface,agg}$
(7) Electrolyte Current	$\nabla \cdot i_2^{agg} = a^{agg}i_{in}^{agg}$	$i_2^{agg} = 0$	$\Phi_2^{agg} = \Phi_2$

(i_2^{agg})			
(8) Electrolyte Concentration (c_0^{agg})	$\epsilon^{agg}\frac{\partial c_0^{agg}}{\partial t} = -\nabla \cdot N_+^{agg} + \frac{a^{agg} i_{in}^{agg}}{F}$ $(N_+^{agg} = -\epsilon^{agg} D_{agg} \nabla c_0^{agg} - \frac{F}{RT} z_+ D_{agg} c_0^{agg} \nabla \Phi_2^{agg})$	$N_+^{agg} = 0$	$c_+^{agg} = c_{bulk}$
(9) Solid State Concentration (c_s^{agg})	$(1-\epsilon^{agg})\frac{\partial c_s^{agg}}{\partial t} = -\frac{a^{agg} i_{in}^{agg}}{F}$	-	-

Electrochemical Reaction Rate

(10) Current Density (i_{in}) Exchange Current Density (i_0)	$i_{in} = i_0[\exp\left(\frac{\alpha_a F\eta}{RT}\right) - \exp\left(-\frac{\alpha_c F\eta}{RT}\right)]$ $i_0 = Fk_{rxn} c_0^{\alpha_a} c_\alpha^{\alpha_c} (c_{\alpha,max} - c_\alpha)^{\alpha_a}$	$\eta = \Phi_1 - \Phi_2 - U$

Reversible Potential

(11) $U = U_{ref} + \frac{RT}{F}\ln\left[\left(\frac{c}{c_0}\right)\left(\frac{1-\bar{c}_{max}}{\bar{c}_{max}}\right)\right] + \sum_{k=0}^{10} A_k[(2\bar{c}_{max}-1)^{k+1} - \frac{2\bar{c}_{max}k(1-\bar{c}_{max})}{(2\bar{c}_{max}-1)^{1-k}}]$ $\bar{c}_{max} = \frac{c_s - c_{s,0}}{c_{s,max} - c_{s,0}}$

Parameter	Value	Parameter	Value	Parameter	Value
$c_{s,max}(mol\ cm^{-3})$	0.0262	A_3	0.023162	A_8	-0.259945
$U_{ref}(V)$	3.868568	A_4	-0.037789	A_9	-0.589845
A_0	-0.201805	A_5	-0.330780	A_{10}	0.052014
A_1	0.112340	A_6	0.239297		
A_2	-0.048369	A_7	0.778712		

2.2.2 Parameter Estimation

The parameter estimation method follows the development of Brady *et al.*[36] A designated parameter space was sampled using Sobol sequences from Python module sobol_seq.[37] After simulations are generated using different sets of parameters from sobol sampling, the residual sum of squares (RSS) is calculated to describe how well the simulations emulate the experimental data. The RSS value of each parameter set is then fed into a Markov-chain monte-carlo (MCMC)[38] method to show statistical distributions of parameters. The parameter values are assumed to form a normal distribution, in which the mean value is the most likely parameter to emulate real electrochemical performance, and the standard deviation indicates the uncertainty in this parameter estimation.

In our study, a three-parameter space comprised of either the agglomerate or crystal scale diffusion coefficient (D_{agg} or D_x), reaction rate constant k_{rxn} of lithium intercalation inside NMC materials and contact resistance (R_{ct}) is sampled. The assumption that anode impedances can be neglected was tested to confirm the modeling approach. Results indicate that the anode overpotential is on the order of 1-2 mV for 0.85 mA/cm^2 (2C) discharge. It was concluded that the estimation of the agglomerate-scale diffusion coefficient is not impacted by inclusion of the anode overpotential.

2.3 Experimental

2.3.1 Cathode Casting

Cathodes were cast on ~ 18 μm Al foil with doctor blades using a mixture of $LiNi_{0.33}Mn_{0.33}Co_{0.33}O_2$ (MSE Supplies LLC), carbon black (Timcal), and PVDF (Arkema Kynar 761) at a mass ratio of 9:0.5:0.5, dissolved in N-Methyl-2-Pyrrolidone (NMP) (Sigma-Aldrich). The as-casted electrode was heated on a hot plate to 110 ℃ to evaporate NMP solvent and cathode with mass loading ~ 2.84 mg/cm^2 could be obtained. Such 25 μm NMC_{111} cathode contains NMC agglomerates with average diameter of 10 μm and NMC crystals with an average diameter of 400 nm.

2.3.2 Coin Cell Assembling

CR2032 Coin cells were made inside an argon filled glovebox. A commercial electrolyte, 1 M $LiPF_6$ in EC/DEC (5:5, w/w) (Gotion Inc.) was used as liquid electrolyte. 250 μm lithium metal foils were used as counter electrode. After assembly, two formation cycles at a C/10 rate were

conducted prior to the galvanostatic and GITT experiments, which were performed employing a Landt battery tester.

2.4 Results

2.4.1 Select Cathode Thickness to Eliminate Electrode Scale Transport Effect

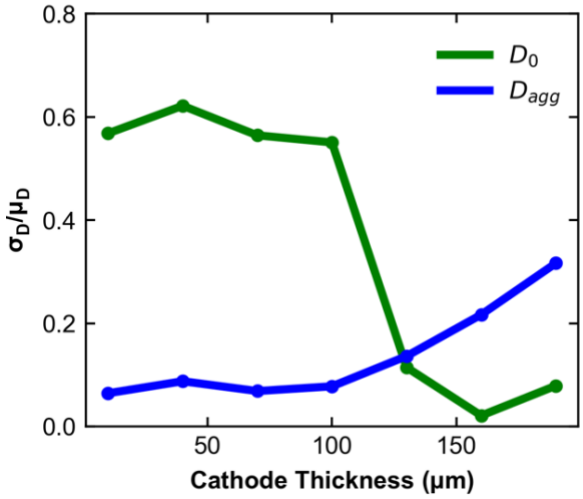

Figure 2.3 Parameter estimation results (normalized uncertainty: σ_D/μ_D) for electrode scale diffusion coefficient (D_0) and agglomerate scale diffusion coefficient (D_{agg}) at different cathode thickness.

Mass transport processes occur at a minimum of at least three different length scales inside the NMC electrode: electrode scale, agglomerate scale and crystal scale. In order to characterize the agglomerate scale and crystal scale mass transport, it is helpful to design experiments in which variations on the electrodes scale are negligible. Intuitively, this implies the use of thin electrodes, and Brady et al[36] showed that mock experiments can quantitively show when a parameter is not important. Specifically, in this case, when the simulated uncertainty σ_{D_0} of the electrode-scale

effective diffusion coefficient is large and $\sigma_{D_{agg}}$ is small, the electrode scale is not important. Figure 2.3 shows the normalized parameter estimation results for cathodes with different thickness (mock experiments). Comparing the uncertainty of electrode scale diffusion coefficient (σ_{D_0}) and agglomerate scale diffusion coefficient ($\sigma_{D_{agg}}$), the result suggests that for thick cathodes ($> 100\ \mu m$), the electrode scale mass transport is more important. While for thin electrodes, the electrode scale transport impedance is negligible. Thus, as we want to eliminate the electrode effect, a thin cathode ($25\ \mu m$) was used to obtain experimental data for further study.

2.4.2 Testing hypotheses by comparing models to galvanostatic experimental data

To compare the simulation results derived from the two alternative hypotheses, the agglomerate model and crystal model were trained using galvanostatic experiments. The cell was operated between 3.0 V and 4.3 V under 0.2 C, 0.33 C, 0.5 C, 1 C and 2 C, in which 1 C = 150 mA/g. For model training, models were fitted to discharge voltage profiles under the 5 current rates, and a single set of parameters was obtained. For the agglomerate model, the diffusion coefficient $D_{agg} = (1.2 \pm 0.2) \times 10^{-9}\ \mathrm{cm^2/s}$, which is within a reasonable range compared with others' reports[39, 40]. This low diffusion coefficient might result from the close packing of NMC crystals inside the agglomerate, which can be observed in Figure 1.1b. For the crystal scale model, a value of $D_x = (5.2 \pm 2.6) \times 10^{-12}\ \mathrm{cm^2/s}$ is obtained. The diffusion coefficient obtained from a crystal scale model is characterized by a significantly higher uncertainty. The higher uncertainty is because the parameter estimation algorithm suggests that the transport impedance is less dominant in the crystal-scale model.

Figure 2.4 shows the experimental voltage profiles and simulation results for both models. Simulation results do not extend to the experimental cutoff (2.8V) because of numerical limitations. Both models agree with experimental data for C-rates below 1 C. For the 2 C rate, the agglomerate model still agrees well with experimental performance, while the crystal model is less successful at the large depth of discharge.

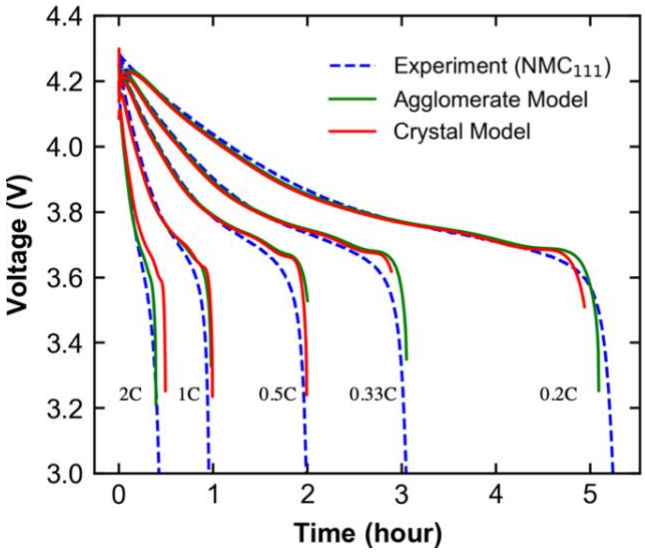

Figure 2.4 Comparison of experimental galvanostatic discharge voltage profile to agglomerate model & crystal model simulation results.

2.4.3 Check consistency of parameter values from different training sets

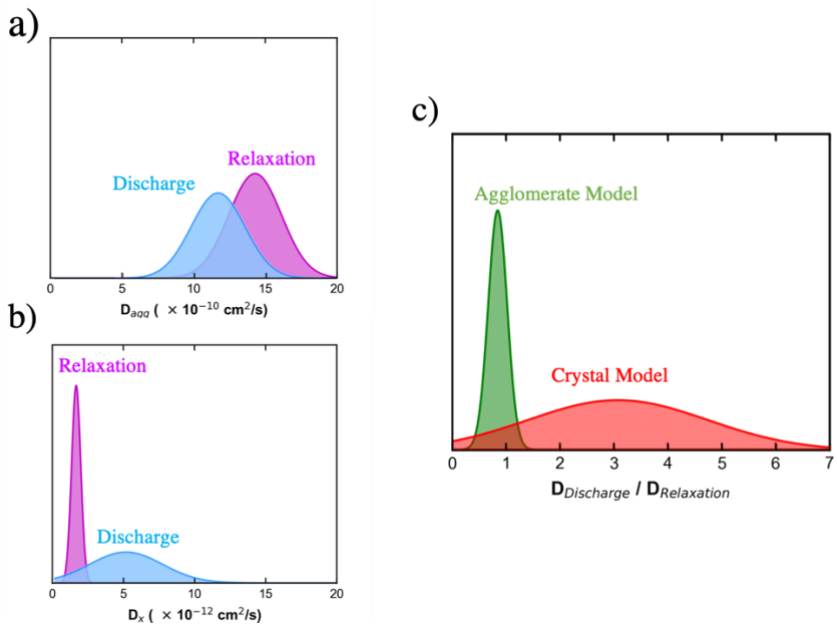

Figure 2.5 (a) and (b) Probability distribution functions of D_{agg} in the agglomerate model and D_x in the crystal model by fitting to discharge data and relaxation data respectively. (c) Distribution of $D_{discharge}/D_{relaxation}$ for agglomerate model and crystal model.

Another method for model selection or hypothesis testing is to compare parameter estimates of the two models when trained with different types of experiments. Ideally, the derived parameters are consistent. Here, models were trained by (1) galvanostatic discharge experiments and (2) relaxation (voltage recovery) experiments. Figures 2.5 show the probability distribution function for the diffusion coefficient obtained by the two models when trained with discharge data and relaxation data. The experimental variation (s_{exp}) is estimated to be 20 mV. It can be seen that for the agglomerate model, discharge and relaxation experiments yield very similar estimates. This is seen in Figure 2.5c, where $D_{discharge}/D_{relaxation} = 0.85 \pm 0.2$. In contrast, the mean crystal-scale state diffusion coefficient (D_x) estimated from discharge and relaxation is 5.2×10^{-12} cm^2/s and 1.7×10^{-12} cm^2/s. In Figure 2.5c, we see $D_{discharge}/D_{relaxation} = 3.1 \pm 1.7$ for the crystal model.

For an ideal system with experimental measurements with no variance, the ratio of diffusion coefficients should be one. In our case, for the agglomerate model, the distribution of $D_{discharge}/D_{relaxation}$ is narrow and has a mean value relatively close to 1. To be more quantitative, the agglomerate model has a 97% chance that $D_{discharge}/D_{relaxation}$ is between 0.6 and 1.4. For the crystal model, there is only a 17% chance that the ratio falls in this range. Thus, by comparing parameter values from different experimental sets for model selection, the agglomerate model has a much higher probability to be correct.

2.4.4 Comparing prediction error

Another means of model selection is to evaluate its prediction ability. Similar to leave-one-out cross validation[41], the model is trained on a combination of data sets to obtain parameters. Then the trained model is used to predict the experimental performance of a test set that is not included in the training sets. In this study, the training sets and test sets were selected from 0.1C, 0.2C, 0.33C, 0.5C, 1C and 2C discharge experiments. To start, the models were trained by the lowest rate (0.1C) to predict the performance at 0.2C. Then the models were trained using a combination of 0.1C and 0.2C to predict 0.33C performance. For the last step, all other current rates was used to predict the performance of 2C discharge. This is named 'forward prediction'. For 'backward prediction', The models are trained by 2C to predict 1C, etc. Figure 2.6 shows the average prediction error, which is the average deviation of prediction from experimental data (e_{sim}) normalized by the experimental variation ($s_{exp} = 20$mV):

$$\bar{e}_{sim} = \frac{e_{sim}}{s_{exp}} \qquad \text{(Equation 2.1)}$$

For both forward and backward prediction, the prediction errors are similar for C-rates less than 0.5C. However, the error starts to differentiate at the higher discharge rates. For 1C prediction, the backward method for the crystal model has a high normalized error ($\bar{e}_{sim}$~3), while the error for the agglomerate model is relatively low ($\bar{e}_{sim}$~ 1.2). For 2C prediction, the forward prediction by the agglomerate model has much lower error than crystal model. This further suggests that the agglomerate scale model is in better agreement with experiment than the crystal-scale model. The deviation at 2C is also seen in Figure 2.4, but perhaps in a less convincing manner.

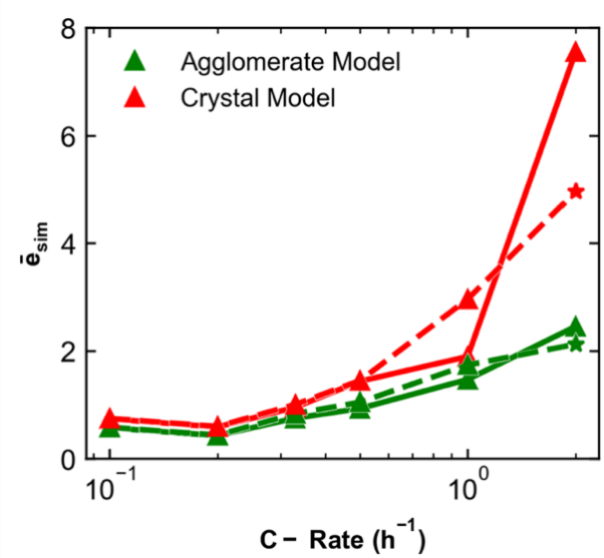

Figure 2.6 Prediction error for 'forward prediction' (solid lines) and 'backward prediction' (dashed lines). The stars are the initial fitted model errors (0.1C for 'forward prediction' and 2C for 'backward prediction') emanating from the initial parameter estimates used for predictions.

2.4.5 Comparing models to experimental dV/dQ profiles

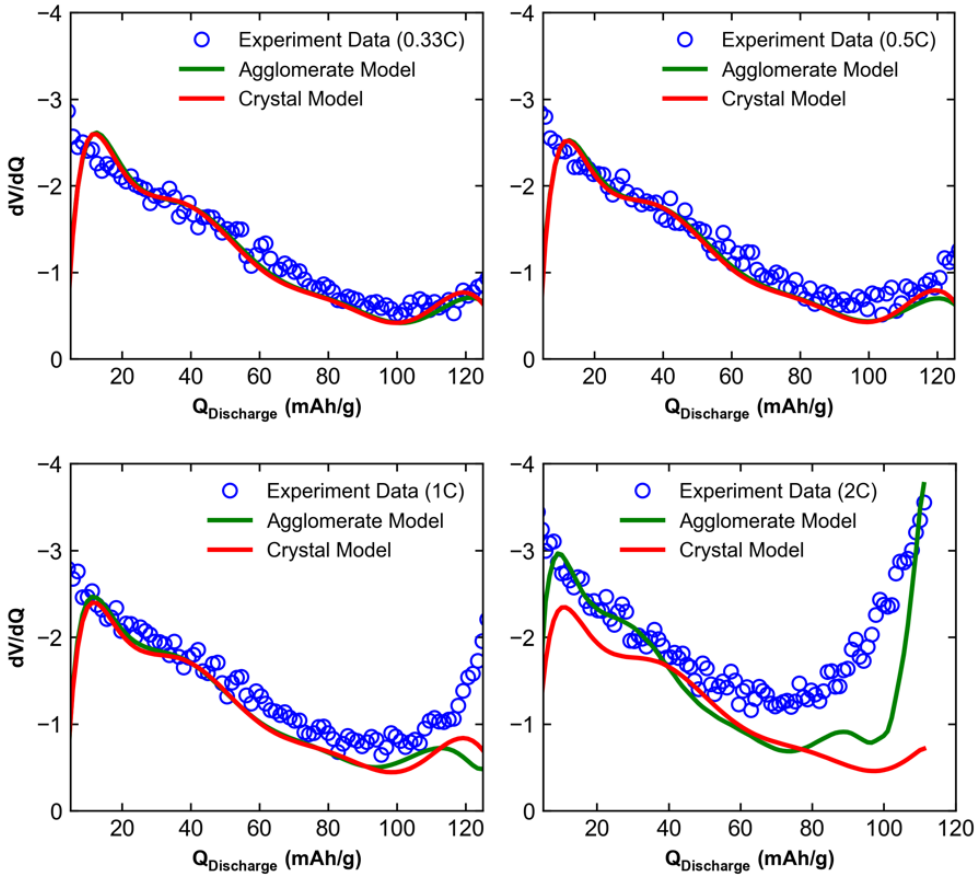

Figure 2.7 Comparison of experimental galvanostatic discharge dV/dQ profile to agglomerate model & crystal model.

In some cases, it may be desirable to predict the changes in voltage rather than the voltage, especially when an experimental uncertainty (such as a contact resistance or anode impedance in a cathode study) is difficult to eliminate. In such cases, models can be trained on for example a dV/dQ curve, which is the derivative of the voltage with respect to discharge capacity. The two models were trained using dV/dQ profiles for 0.33C, 0.5C, 1C and 2C and the resulted simulation results are shown in Figure 2.7. Just as in Figure 2.3, by fitting to dV/dQ curve, the two models are only distinct at 2C. The agglomerate model agrees better with experimental dV/dQ. Results

gave $D_{agg} = (1.2 \pm 0.2) \times 10^{-9}$ cm^2/s , identical to values obtained by fitting *V vs* time. For the crystal scale model, D_x = (5.9±2.5) $\times 10^{-12}$ cm^2/s, which are also close to values obtained by fitting *V vs* time.

2.4.6 Diffusion coefficient as a function of state of charge (SOC)

Often, experimental investigations are not closely integrated with modeling development. Thus, a broadly applied theory is often used to estimate diffusion coefficient:[42, 43]

$$\widetilde{D} = \frac{4}{\pi\tau}\left(\frac{m_B V_M}{M_B S}\right)^2 \left(\frac{\Delta E_s}{\Delta E_t}\right)^2 \quad (\tau \ll L^2/\widetilde{D}) \qquad \text{(Equation 2.2)}$$

where $\tau(s)$ is the time duration for each discharge step, m_B(g) is the mass of NMC, M_B (g/mol) is the atomic weight of NMC, $V_M(cm^3 mol^{-1})$ is the molar volume of the NMC materials, S(cm^2) is the area of electrode. $\Delta E_s(V)$ and $\Delta E_t(V)$ are the change of voltage between relaxations and during discharge.

Note that Equation 2.2 is derived assuming a crystal scale model, and the inequality constraint arises because the physics used to derive Equation 2.2 assumes semi-infinite diffusion[44]. The use of Equation 2.2 may lead to, for example, a conclusion that the diffusion coefficient is a function of the state of charge (SOC). While that is theoretically possible if not probable, whether it leads to improved agreement with experiment is a valid question.

To study the apparent SOC dependency of the diffusion coefficient, voltage recovery data from GITT experiments are used to determine the diffusion coefficient values from the two models, with results shown in Table 2.2. Instead of absolute diffusion coefficients, values of D/L^2 are shown, where L is the diffusion length. Also, D/L^2 values calculated from experimental

GITT data by Equation 2.2 are listed. Figure 8 shows D/L^2 from agglomerate model fitting, crystal model fitting and from Equation 2.2 calculation at 1C.

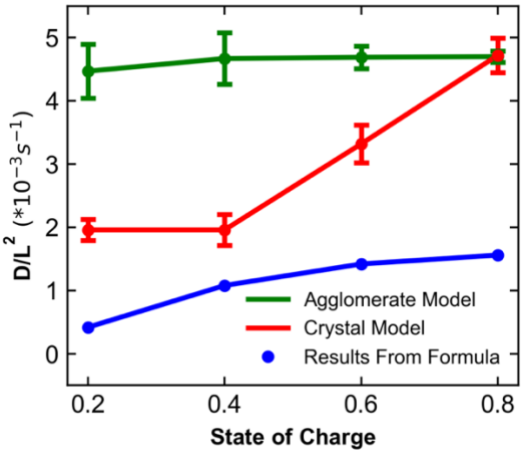

Figure 2.8 D/L^2 values for agglomerate model (Agg), crystal model (Xtal) and Equation 2.2 at 1C rate experiment.

Table 2.2 D/L^2 values from fitting agglomerate model (Agg) and crystal model (Xtal) to relaxation experiments at different SOC, and D/L^2 values calculated by Equation 2.2.

SOC	C/2			1C			2C		
	Equation 2.2	Agg	Xtal	Equation 2.2	Agg	Xtal	Equation 2.2	Agg	Xtal
83.3%	0.97	6.97	3.94						
80%				1.56	4.70	4.72			
66.7%	0.88	5.82	2.27				1.68	6.17	3.68
60%				1.42	4.69	3.32			
50%	0.77	7.03	1.64						
40%				1.08	4.67	1.96			
33.3%	0.4	6.16	0.87				0.55	5.33	2.06
20%				0.42	4.47	1.96			
μ	0.76	6.50	2.17	1.12	4.63	2.99	1.12	5.75	2.87
σ	0.22	0.52	1.13	0.44	0.09	1.14	0.56	0.42	0.81

As shown in Table 2.2 and Figure 2.8, for the agglomerate model, the D/L^2 value is relatively constant with state of charge. In short, a constant diffusion-coefficient model is consistent with experiment. The crystal scale model suggests that D_x increases with state of charge (this corresponds to decreasing D_x with increasing solid-state Li concentrations). Note however, that the value of D_x remains inconsistent with values estimated from the discharge curve (*c.f.,* Figure 2.4). Furthermore, diffusion coefficients fit through agglomerate and crystal models are consistent with values obtained by Equation 2.2 only to an order of magnitude.

2.5 Discussion

The two models are hard to distinguish at relatively low discharge rates (lower than 1C in this paper), without simultaneously considering GITT relaxation data. This was unexpected based on previous experience[32]. Design of experimental conditions that allow for a distinction between the two models is possible. In this experimental design, the diffusion coefficient is assumed to be known. Thus, the problem explores whether a crystal model, which is fitted to agglomerate model simulations, can predict agglomerate models results under new conditions. If it can, then the models are indistinguishable.

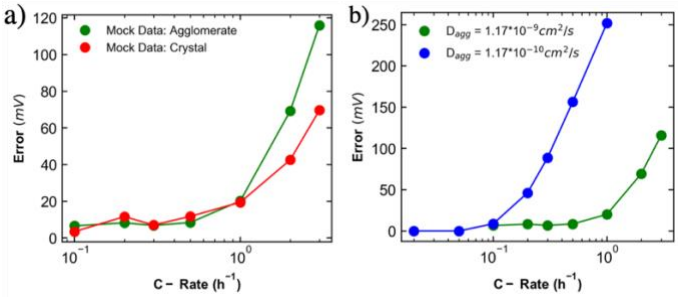

Figure 2.9 (a) Prediction error as a function of current rate, using agglomerate model (green) and crystal model (red) to generate 'Mock experiments', respectively. (b) Prediction error when using agglomerate model with different D_{agg} to generate 'Mock experiment'.

The algorithm works the same as the prediction test of Figure 2.6, except it is now applied to mock data. For example, the agglomerate model is fitted to low C-rate crystal model results, and then used to predict performance at higher rates. The resulting error (red curve) is shown in Figure 2.9a. At high C-rates, the models are distinguishable as evidenced by the growing error. The reverse is also shown, where the green curve corresponds to applying the crystal model to agglomerate model results. In both cases, the errors grow after 1C, indicating that the 1C rate is the critical current rate in this system. ***In other words, for current rates above 1C, the two models perform differently.***

In contrast to the NMC cathode, when Knehr[32] et al applied model selection to multi-scale magnetite cathodes, crystal and agglomerate models were distinguishable at all tested C-rates. This indicates that the critical current rate is dependent on the intrinsic properties of the materials studied. To explore further, mock experiments were generated using the agglomerate model, with smaller D_{agg}. As shown in Figure 2.9b, the critical current rate to distinguish between two models is 0.1C. In an attempt to generalize this problem, a dimensionless C-rate given by

$$\bar{C}_{rate} := C_{rate} \cdot \frac{L_{agg}}{D_{agg}} \cdot L_x \qquad \text{(Equation 2.3)}$$

where L_{agg} is the mean radius of the agglomerate and L_x is the mean radius of the crystal, was introduced.

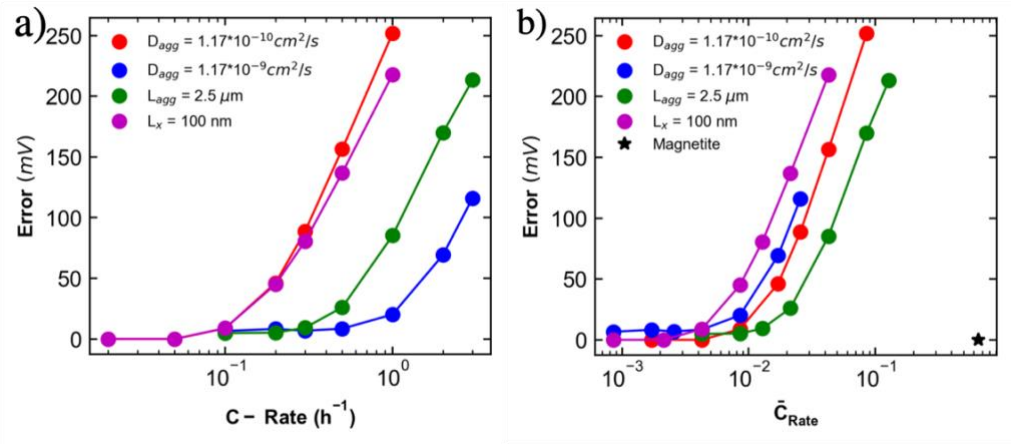

Figure 2.10 (a) Prediction Error as a function of absolute current rate, 'Mock experiments' generated by agglomerate model with different material parameters. (b) Prediction Error as a function of dimensionless current rate. For red 'Mock experiments', $D_{agg} = 1.17 \times 10^{-10}\ cm^2$, $L_{agg} = 5\ \mu m$ and $L_x = 200\ nm$. Each of other 'Mock experiments' have one parameter with different value. For magnetite, only dimensionless current rate is shown here to compare with NMC cathode in this study.

Figure 2.10a shows the prediction error with different materials properties (applied on agglomerate 'Mock Data'). The absolute critical current rate is dependent on D_{agg}, L_{agg} and L_x. When using dimensionless current rate ($\bar{C}_{rate}$), the errors start to increase near $\bar{C}_{rate} \sim 10^{-2}$, as shown in Figure 2.10b. Due to the complexity of the multiscale model, in which modeling details are chemistry specific, we did not attempt further analyses to collapse the error to a single curve. The black star in Figure 2.10b shows the dimensionless current rate of magnetite calculated using parameters from the study by Knehr[32] et al. The value of $\bar{C}_{rate}$ for C/200 was greater than 0.1 for magnetite, explaining why the models were easily distinguishable even at very low C-rates. This result indicates that the critical current rate to distinguish between agglomerate and crystal model depends on size of agglomerate (L_{agg}), the size of crystal (L_x) and the diffusion coefficient on one of the two smaller scales (D_{agg} here).

2.6 Conclusion

Model selection approaches can be used to determine whether an agglomerate-scale or crystal-scale model is more consistent with experiment. Model-guided design of experiments can be used to test hypotheses. At low C-rates, crystal scale and agglomerate scale models are indistinguishable if the diffusion coefficient is assumed to be an unknown fit to experiment. For NMC_{111} material, agglomerate scale diffusion, which is the diffusion of lithium across the secondary particles was determined to be rate limiting. This conclusion is supported by multiple algorithmic approaches that test consistency between experiments and the prediction efficacy of the models.

2.7 List of Symbols

Electrode Scale Symbols

a	Specific surface area (cm^{-1})
c_0	Concentration of lithium in the electrolyte (mol cm^{-3})
c_{bulk}	Concentration of lithium in the bulk electrolyte, 1×10^{-3} (mol cm^{-3}) in study.
$i_{applied}$	Applied current density (A cm^{-2})
D_0	Diffusion coefficient for lithium ions in bulk electrolyte, 1×10^{-6} (cm^2 s^{-1}).
$D_{0,eff}$	Effective electrolyte diffusion coefficient (cm^2 s^{-1})
$L_{cathode}$	Thickness of NMC cathode, 25 (μm) in experiment
$L_{separator}$	Thickness of separator, 25 (μm) in experiment
N_+	Flux of lithium ions in electrolyte (cm^{-2} s^{-1})
ϵ	Void fraction of porous electrode (porosity), 0.673 in experiment.
σ	Solid state conductivity (S cm^{-1})
κ	Solution conductivity (S cm^{-1})
z_i	Species charge
u_i	Species mobility (cm^2 s mol J^{-1})
Φ_1	Solid state potential (V)
Φ_2	Solution potential (V)

Crystal Scale Symbols

$c_s^{\ x}$	Concentration of lithium in NMC_{111} inside crystals (mol cm^{-3})
D_x	Diffusion coefficient for lithium in the NMC_{111} crystals
L_x	Average radius of NMC_{111} crystals, 200 (nm) in experiment

Agglomerate Scale Symbols

a^{agg}	Specific surface area inside agglomerate (cm^{-1})
A_{agg}	Average cross-sectional area of agglomerates (cm^2)
V_{agg}	Average volume of agglomerates (cm^3)
$c_0^{\ agg}$	Concentration of lithium in the electrolyte inside agglomerate (mol cm^{-3})
$c_s^{\ agg}$	Concentration of lithium in NMC_{111} inside agglomerate (mol cm^{-3})
D_{agg}	Diffusion coefficient for lithium ions in the NMC_{111} agglomerate (cm^2 s^{-1})
L_{agg}	Average radius of NMC_{111} agglomerates, 5 (nm) in experiment
$N_+^{\ agg}$	Flux of lithium ions in electrolyte inside agglomerate (cm^{-2} s^{-1})
ϵ^{agg}	Void fraction inside agglomerate
$\Phi_1^{\ agg}$	Solid state potential (V)
$\Phi_2^{\ agg}$	Solution potential (V)

Reaction Thermodynamics and Charge Transfer Kinetics Symbols

F	Faraday's constant (96,485 C mol^{-1})
k_{rxn}	Reaction rate constant for insertion of lithium inside NMC (cm$^{5/2}$ mol$^{-1/2}$ s^{-1})
i_{in}	Local current density for lithium insertion (A cm^{-2})
i_0	Exchange current density for lithium insertion (A cm^{-2})
R	Ideal gas constant (8.314 J mol^{-1} K^{-1})
T	Temperature, 298(K) in experiment
U	Reversible potential for lithium insertion reaction(V)
α_a	Anodic charge transfer coefficient, 0.5 in experiment
α_c	Cathodic charge transfer coefficient, 0.5 in experiment
η	Overpotential for lithium insertion reaction (V)

Chapter 3: Optimal Electrode-Scale Design of Li-Ion Electrodes: A General Correlation[†]

[†]This work has been published: Hui, Zeyu, Karthik S. Mayilvahanan, Krystian Ganko, Yuan Yang, Xiao Zhang, Zhengyu Ju, Kenneth J. Takeuchi et al. "Optimal electrode-scale design of Li-ion electrodes: A general correlation." Energy Storage Materials 39 (2021): 176-185.
The thesis writer's contribution was the model development, data analysis and paper writing. The electrochemical data for LVO is provided by Qing Zhang from the Marschilok-Takeuchi Research Group at Stony Brook University. The electrochemical data for FEO and VOPO4 is provided by Xiao Zhang and Zhengyu Ju from Yu Group at University of Texas, Austin.

3.1 Introduction

Energy storage is a key technology to enable widespread adoption of intermittent, renewable energy sources.[45-47] Lithium ion batteries (LIBs) are widely used because they are characterized by high energy density, high power density, and good cycle life.[48] Nevertheless, new applications often place new requirements on LIBs. Broad application of LIBs on the electric vehicle (EV) market requires the current batteries to have higher energy density, in order to cut cost and prolong mileage.[49, 50] Improvements can be achieved by new intercalation materials[15, 19, 51] as well as by optimizing cell design.

Among the different factors that limit the improvement of battery energy density, transport impedances are crucial.[52, 53] Transport impedances may arise on different length scales.[54] For example, as depicted in Figure 1, transport of lithium ions may take place on multiple length scales inside the $Li_xNi_{1/3}Mn_{1/3}Co_{1/3}O_2$ (NMC_{111}) electrode. During battery operation, lithium ions inside the liquid electrolyte not only diffuse through the porous electrode (electrode scale), but also diffuse through secondary agglomerates formed by crystals (agglomerate scale). Meanwhile, intercalated lithium must also diffuse from the crystal surface to its center (crystal scale). It may be difficult to determine whether transport impedances are more important on the agglomerate or crystal scale.[55] It may be however more straightforward to design electrodes where electrode-scale transport impedance is minimal, and this can be an important strategy in laboratory investigations of agglomerate and crystal scale transport,[56, 57] also a widely adopted method to increase cell energy density.

Newman and collaborators reported the application of a physics-based model on cell energy density optimization and design.[12, 58] Fuller *et al.*[12] constructed the dual-insertion model and simulated the performance of the graphite/$LiMn_2O_4$ cell, optimizing the specific energy and

specific power of such cell by varying cathode thickness and porosity. However, only one parameter was changed at a time in this study. Srinivasan *et al.*[26] used a model to perform simultaneous optimization of anode and cathode thicknesses and porosities to improve energy density of graphite/$LiFePO_4$ cells. Appiah *et al.*[59] applied a similar approach to graphite/$LiNi_{0.6}Co_{0.2}Mn_{0.2}O_2$ cells, optimizing for cathode porosity and thickness. De *et al.*[60] extended such algorithm to simultaneous optimization of different numbers of parameters, including porosities and thicknesses for cathode and anode. All of the previous studies focused on optimizing the electrode design of a specific type of active material.

In this study, we optimize electrode-scale design parameters and show that agglomerate and crystal scale transport properties do not significantly affect the values of the electrode-scale design parameters needed to optimize energy density. Results are generalized to consider four different cathode active materials, and we show with a re-scaling of the current rate, the optimal design parameters follow a general design rule, captured in a convenient correlation.

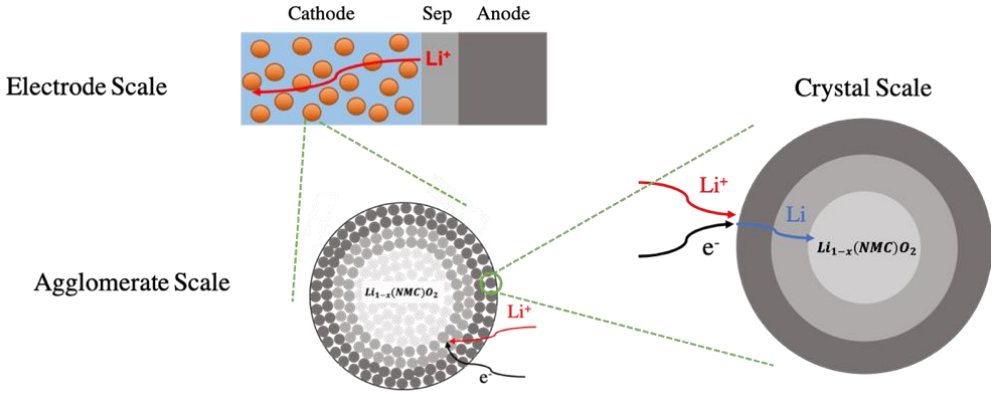

Figure 3.1 Schematic illustration of lithium transport on different length scales of an NMC_{111} electrode. Most physics-based models couple the electrode scale with either an agglomerate or crystal scale description of transport processes.

3.2 Theory and Methods

Physics-based models, validated by comparison with experimental discharge voltage profiles, are used to determine the optimal cathode design through sampling approaches that leverage high performance computer resources.[61] The physics-based continuum model used in this study followed the development by Newman et al,[11] except it uses a finite-volume numerical method that allows for a more general treatment of the smaller scale, including phase change reactions as well as agglomerate and crystal-scale models. A detailed description of the NMC cathode model is given in the study by Hui et al.[55] A so-called pseudo 2D (P2D) modeling paradigm[62] was used to connect the smaller-length scale simulations to the parameters that are controlled during fabrication on the electrode scale. Equations describing transport of lithium inside the agglomerate or crystal are coupled to the electrode scale equations.

For thick electrodes relevant to high energy density applications,[63] the performance of electrodes is strongly dependent on electrode-scale transport processes. To minimize the electrode scale transport loss and get highest energy density, the electrode porosity and active material loading were optimized by sampling in two-dimensional space. The tortuosity of the electrode is the major source of uncertainty in optimization, as that is strictly an electrode scale effect, difficult to measure directly. Applicability of the proposed approach when considering this uncertainty in tortuosity is discussed.

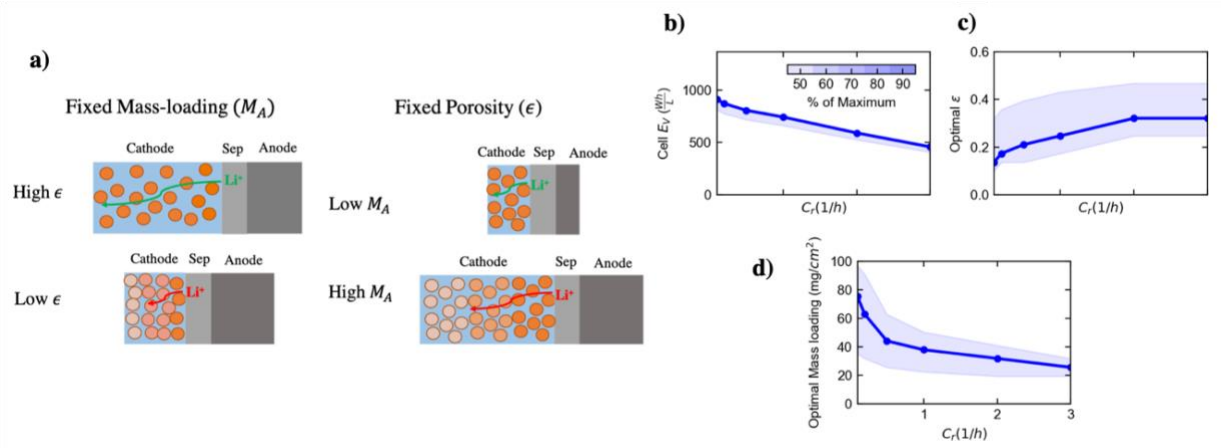

Figure 3.2 (a) Schematic illustrating the key design parameters, mass loading and porosity. The thickness of the electrode is determined by these variables. (b) Optimal volumetric energy densities (E_V) over a range of discharge rates from C/10 to 3C (1C = 150 mA g^{-1}). (c,d) The optimal porosity and mass loading with which electrodes can be fabricated to achieve that E_V. The shading shows the parameter value regions to reach 90 % of maximum E_V.

As shown in Figure 3.2a, to maximize the volumetric energy density (E_V) of a cell at a given current, there are two competing directions to be considered. While increasing areal mass loading of active material or making the electrode denser (less porous) tends to increase volumetric energy of the cell by using the space more efficiently, it leads to sluggish ion transport into the electrode, which decreases the utilization of electrode material. On the contrary, using thin and porous electrodes helps the electrode retain full utilization, but given that the thickness of the current collectors and separator are fixed, such design leads to low E_V because a large portion of the volume is occupied by inert components. Consequently, finding the balance between improving electrode utilization and increasing mass loading (or reducing electrode porosity) becomes the key of optimizing cell E_V.

The electrode scale optimal design followed the algorithm from Mayilvahanan et al.[64] Taking $Li_xNi_{1/3}Mn_{1/3}Co_{1/3}O_2$ (NMC_{111}) electrode as an example, the optimal result is shown in Figure 3.2bcd. In addition to active material, electrodes may be comprised of other solid materials to

impart mechanical integrity (e.g., binder) and to impart electronic conductivity (e.g., 10 % in volume of super C_{65}). Since such materials do not store Li ions, the optimal volume fraction of the component should be minimized, at for example a volume fraction slightly exceeding the percolation threshold.[65, 66] Here, it is assumed that $V_{AM}/(V_{AM} + V_{inert}) = 0.9$. In all cases, while a finite electronic conductivity is considered, it is sufficiently large that electronic resistances are minimal. Thus, optimal design is dependent primarily on the electrode porosity ($\epsilon = 1 - V_{AM} - V_{inert}$) and electrode areal mass loading (M_A in mg cm^{-2}).

Parameter sets obtained from a grid sampling among the 2D parameter space were fed to the model to simulate performance. The volumetric energy density E_V is given by

$$E_V = \frac{E_A}{L_{cathode} + L_{anode} + L_{BOC}} \qquad \text{Equation 3.1}$$

where the energy per area E_A is given by

$$E_A = \int_0^{t_{dchg}} V(t)\, i_{applied}\, dt \qquad \text{Equation 3.2}$$

The thickness of cathode ($L_{cathode}$) is calculated by

$$L_{cathode} = \frac{M_A}{\rho_{AM} V_{AM}} \qquad \text{Equation 3.3}$$

in which V_{AM} is the volume ratio between active material and the whole electrode (including volume of pores). The graphite anode is assumed to be capacity matched at a 1:1 ratio with cathode, given by

$$L_{anode} = \frac{Q_{cathode}\, M_A}{Q_{anode}\, (1-\epsilon_{anode})\, \rho_{graphite}} \qquad \text{Equation 3.4}$$

in which the graphite anode porosity (ε_{anode}) is assumed to be fixed at 0.35. It is further assumed that the thickness of Balance of Cell L_{BOC} (assumed to be 50 μm) is given by the sum of separator and current collector thicknesses:

$$L_{BOC} = L_{separator} + L_{cc}^{anode} + L_{cc}^{cathode} \qquad \text{Equation 3.5}$$

The optimal volumetric energy density E_V is shown in Figure 3.2b as a function of the current, given as a C rate (C_r). The corresponding optimal mass loading and porosity are shown in Figures 3.2c and 3.2d and follow expected trends. The optimal ε increases while the optimal mass loading drops with increasing C_r, indicating that electrode should be more porous and also thinner to retain good utilization. The shaded regions provide an estimate of sensitivity of E_V to the design parameters, showing the range of values of one parameter that leads to 90% of the maximum achievable cell E_V when the other parameter is set at its optimal value. For example, if one synthesizes electrodes with mass loading of 38 mg cm^{-2}, any porosity in the range of 0.17-0.43 will yield an E_V that is within 90% of the optimum at C_r = 1C.

3.3 Results

3.3.1 Optimal cell E_V affected by smaller scale parameters

Battery performance is impacted by the transport impedance on both the electrode scale and the smaller scales. Previous work[55] has shown that the agglomerate scale may be the dominant smaller length scale for Li transport in NMC_{111} electrodes, and thus an agglomerate model most faithfully replicates experiments. Depending on the fabrication processes and the choice of material, the agglomerate size (L_{agg}) and the effective diffusion coefficient (D_{agg}) through the agglomerate may vary. The impact of these parameters on performance is simulated and shown in Figure 3.3a, which again shows optimal energy density as a function of C_r. The optimal energy

density improves with increasing D_{agg} or decreasing L_{agg}. Changing L_{agg} leads to greater impact on optimal E_V than changing D_{agg} because the time constant for lithium diffusion $\tau_{agg} = \frac{L_{agg}^2}{D_{agg}}$.

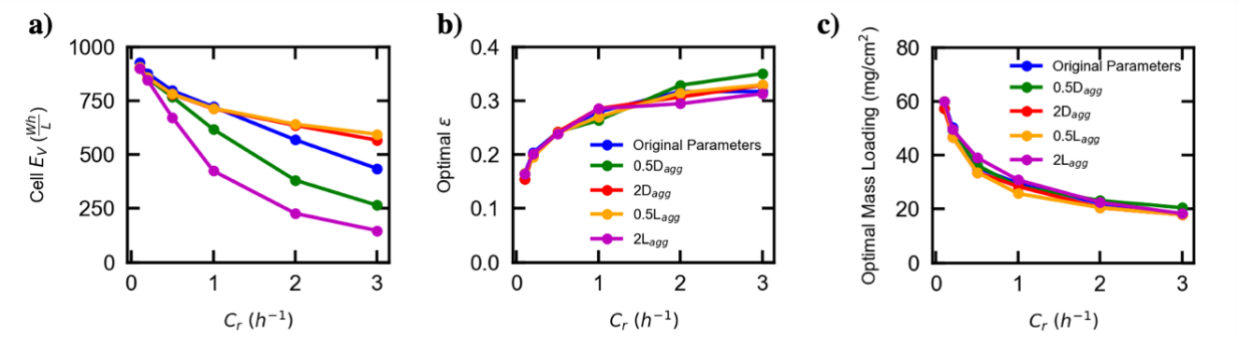

Figure 3.3 (a) Optimal E_V obtained for different L_{agg} and D_{agg}. The original parameter refers to L_{agg} = 5 μm and D_{agg} = 1.4 × 10^{-9} cm^2 s^{-1}. (b,c) Optimal ε and M_A resulting from the assumed L_{agg} and D_{agg}.

3.3.2 Optimal electrode scale design does not depend on smaller scale parameters

Although the smaller scale transport impedance significantly impacts the optimal E_V, it does NOT appear to affect the optimal choices of electrode-scale design parameters. As shown in Figure 3.3b and 3.3c, although curves with different colors have various agglomerate scale parameters, the optimal ε and optimal M_A all overlap, indicating that optimization with different agglomerate scale properties leads to identical electrode-scale design in order to maximize E_V. Given that electrode-scale design is not affected by smaller scale properties, it is possible to generalize optimization of electrode-scale design parameters, even if each different active material has different smaller scale properties.

3.3.3 The electrode tortuosity impacts optimum

The electrode tortuosity (τ) may be dependent on multiple parameters, including porosity, the shape of the active materials, as well as the type of conductive filler and binder. Furthermore, the tortuosity may depend on the details of the fabrication processes.[67] Optimization results show that the optimal porosity and mass loading are strongly dependent on tortuosity. However, tortuosity may be difficult to estimate in practice. Commonly, a Bruggeman relationship[68] for spherical particles (Equation 3.6) is used to estimate the tortuosity as a function the electrode porosity.

$$\tau = \epsilon^{-0.5} \qquad \text{Equation 3.6}$$

However, significations deviations from Equation 3.6 are often found. For example, an electrode comprised of 2D nanosheets will have higher tortuosity at a given porosity if the sheets stack perpendicular to the diffusion direction.[69]

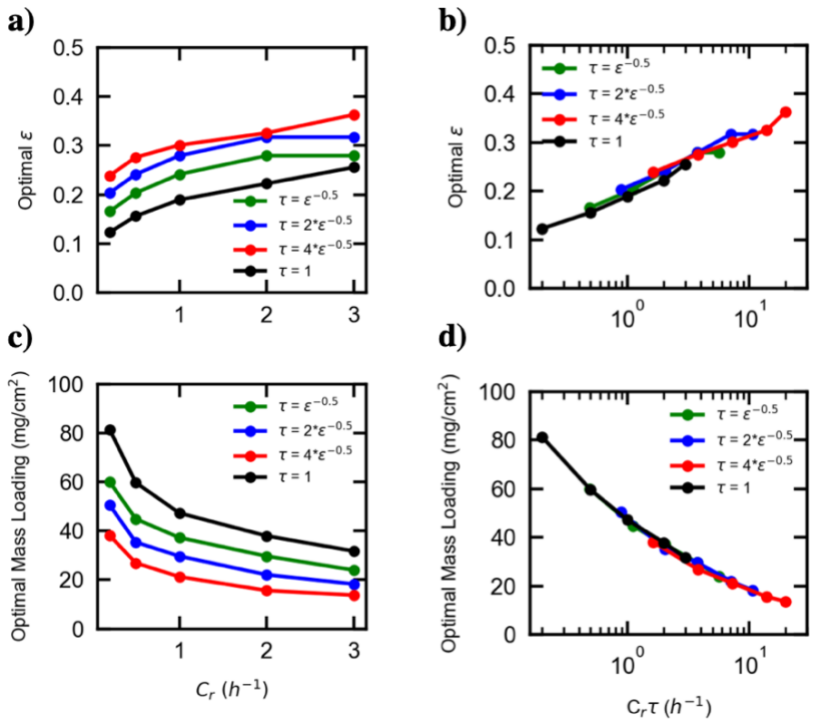

Figure 3.4 Optimal electrode parameters depend strongly on the assumed tortuosity (ac). However, if the C_r is multiplied by τ, the optimal ε and M_A follow a single curve (bd).

Figure 3.4a and 3.4c show the optimal porosity and mass loading for assumptions of Bruggeman-like relationships that vary tortuosity by up to a factor of four. Also shown is an extreme case where tortuosity is one for all porosities (black lines). With increasing tortuosity, the effective diffusion coefficient of the electrolyte decreases, and this results in a larger optimal porosity and lower optimal mass loading to retain good electrode utilization. However, if the C-rate (C_r) is multiplied by τ, the optima fall on a single curve, as shown in Figures 3.4b and 3.4d.

3.3.4 Generalize the difference in electrolyte property

For different materials, the intrinsic electrolyte properties may also vary by changing the Li salt concentration and solvent. Various electrode materials may be paired with different electrolytes due to chemical stability considerations. As shown in Figure 3.5a and 3.5c, an electrolyte with a lower bulk diffusivity (D_0) or lower salt concentration (c_0) leads to higher optimal porosity and lower optimal mass loading. We found the optima overlap if the C_r is multiplied by $\frac{1}{FD_0c_0}$, as shown in Figure 3.5b and 3.5d. In summary, after rescaling C_r with $\frac{\tau}{FD_0c_0}$, the effect of variations in electrode tortuosity and electrolyte properties can be accounted for with a single curve for the case of NMC. The underlying physical explanation of such rescaling is discussed in the next section.

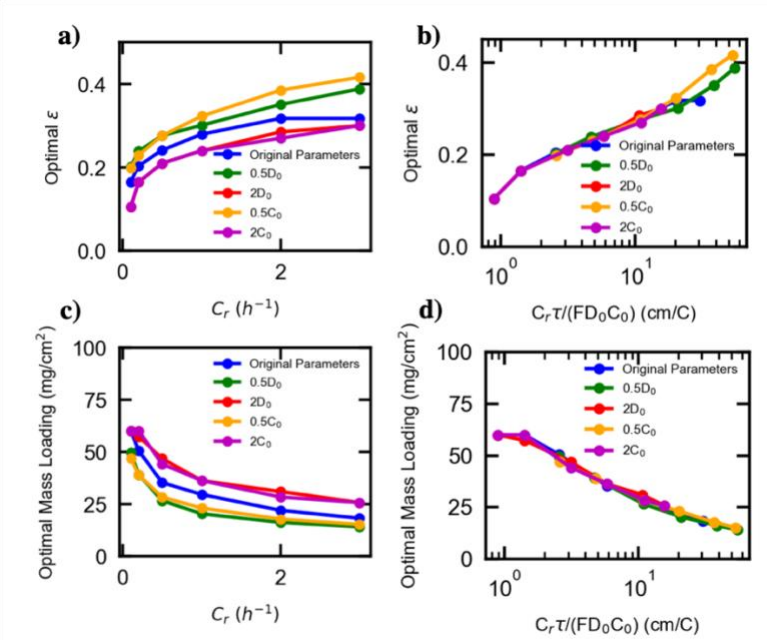

Figure 3.5 The optimal electrode parameters depend on electrolyte. For original parameters, D_0 = 1×10^{-6} cm^2 s^{-1}, c_0 = 1.0 M, $\tau = \epsilon^{-0.5}$, and results are shown in (ac) by varying diffusion coefficient or salt concentration. (bd) When plotted as a function of $C_r\tau/(FD_0c_0)$, the optimal ε and M_A follow a single curve.

3.4 Discussion

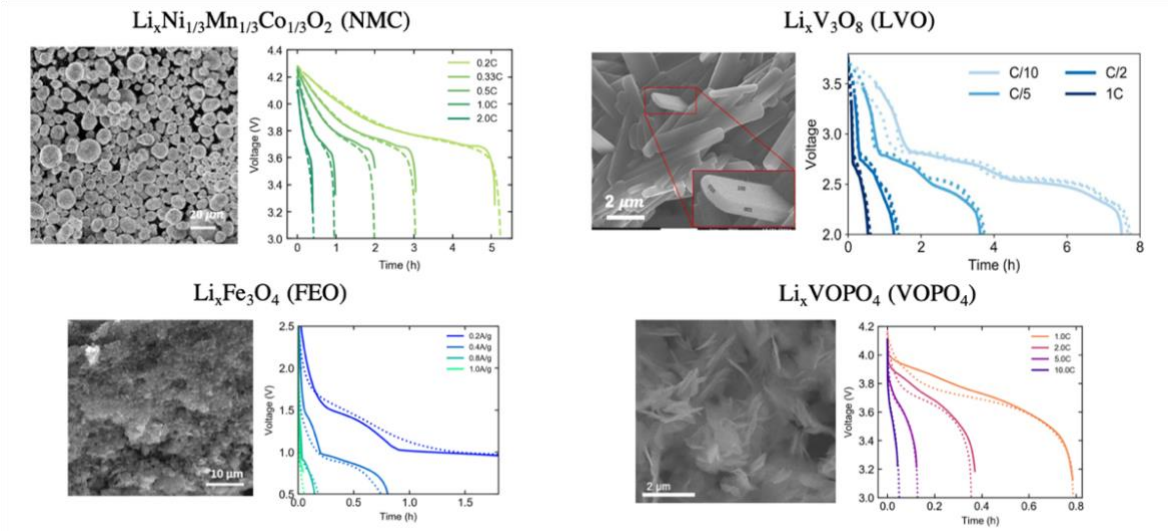

Figure 3.6 SEM images of different material.[55, 64, 70-72] Voltage profiles show the agreement between simulations (solid lines) and constant current discharge experiments (dashed lines). The

SEM image for LVO are reproduced under terms of the CC BY NC ND License.[70] Copyright 2018, Brady et al., published by ECS. The Voltages profiles for LVO are reproduced under terms of the CC BY License.[64] Copyright 2020, Mayilvahanan et al., published by IOP.

Table 3.1 Physical properties, tortuosity assumptions and sources of models as well as experiments that models were validated against for different electrodes. For FEO, only capacities above 1V were considered. For $VOPO_4$, the model is newly constructed, and the detailed information is shown in Appendix.

Active material	Density (g cm^{-3})	Specific Capacity (mAh g^{-1})	Tortuosity assumption	References
NMC	4.6	150	$\tau = \epsilon^{-0.5}$	Hui et al.[55]
LVO	3.15	362	$\tau = \epsilon^{-0.5}$	Mayilvahanan et al.[64]; Brady et al.[70]
FEO	5.15	350	$\tau = \epsilon^{-0.5}$	Zhang et al.[71]; Knehr et al.[32]
$VOPO_4$	2.31	166	$\tau = 14.2\epsilon^{-0.266}$	Ju et al.[72]

3.4.1 Smaller scale structures and physics-based models of different electrodes

Figure 3.6 shows four distinct electrode materials that have been characterized and modeled. Table 3.1 provides the sources for model construction. As seen in the SEM micrographs, NMC and FEO have nanometer sized crystals that agglomerate into secondary particles (agglomerates), while the smaller-scale transport impedance for LVO and $VOPO_4$ is dominated by the crystal scale with lateral size of microns. Such structural differences lead to varying small-scale impedances. Moreover, LVO and FEO undergo a reversible phase change during lithiation and de-lithiation, shown by the voltage plateaus on discharge voltage profiles.

Following the procedure outlined for optimization of NMC electrodes in the previous section, optimization of electrode-scale design of each of these cathode materials was conducted using previously validated physics-based models[32, 55, 64], for which agreement with experiments are

shown in Figure 3.6. The P2D models have significantly different physics on the smaller scale, but electrode-scale descriptions are identical. Table 3.1 lists the parameters used in those P2D models.

3.4.2 Summary for different electrodes

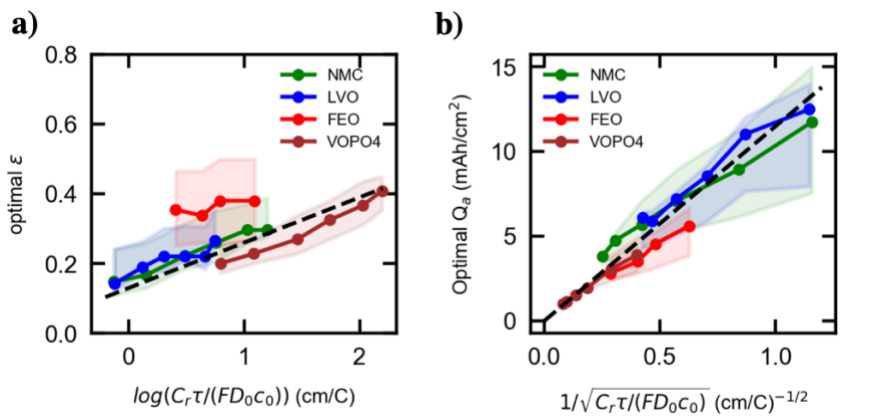

Figure 3.7 Optimal design results for 4 different materials, plotted vs rescaled current rate. Assumptions: $D_0 = 1 \times 10^{-6}$ cm^2 s^{-1}, $c_0 = 1.0$ M for all electrodes. Optimal ε and Q_a are shown by solid lines. Shaded regions indicate sensitivity of the parameter values by showing region to achieve 95% of the maximum E_V. Black dashed lines indicate the general correlation between rescaled C_r and optimal designs.

Figure 3.7 shows the optimization results of cells with different materials as the cathode, assuming graphite as an anode with an n/p capacity ratio (ratio between graphite electrode capacity and positive electrode capacity) of 1 and with a fixed anode porosity of 0.35. Again, it is assumed that $V_{AM}/(V_{AM} + V_{inert}) = 0.9$.

In Figure 3.7b, the loadings of active material are given as capacity loading Q_a $\left(= \frac{M_A Q_{cathode}}{10^3}\right)$. The solid lines in Figure 3.7ab present the optimal design parameters to achieve highest E_V, while the shaded regions give sensitivity, indicating a range that allows for

achievement of 95% of the maximum E_V. The optimal Q_a results on Figure 3.7b follow a (dashed) trend line. The optimal porosity ε is in Figure 3.7a. Despite the outlier FEO, the optimal ε of all other materials overlap, especially accounting for the 95% sensitivity contours. This suggests ***a generalized correlation, which is independent of the active material***.

3.4.3 General Correlations

As shown by the black dashed lines on Figure 3.7, two relations describing the relation between general design optimal parameters and generalized C_r were obtained:

$$\epsilon = 0.13 \log_{10}\left(k_\epsilon \frac{C_r \tau}{F D_0 c_0} \right) \qquad \text{Equation 3.7}$$

$$Q_a = k_Q / \sqrt{k_\epsilon C_r \tau / (F D_0 c_0)} \qquad \text{Equation 3.8}$$

where the constant k_ε = 11.94 C cm^{-1} and k_Q = 38.03 mAh cm^{-2}. Since electrode tortuosity τ is anticipated to be dependent on porosity (Bruggeman relation for spherical particles for example), one may need to solve Equation 3.7 and the known$\tau = f(\epsilon)$ relation simultaneously to obtain optimal ε, and then to use Equation 3.8 to estimate the optimal areal capacity loading Q_a. Figure 3.8 shows the results of optimal ε and Q_a calculated using Equations 3.7 and 3.8 (dashed lines), which agrees well with numerical optimization results (solid lines), especially with the 95% sensitivity contours, as shown by the shaded regions in Figure 3.7.

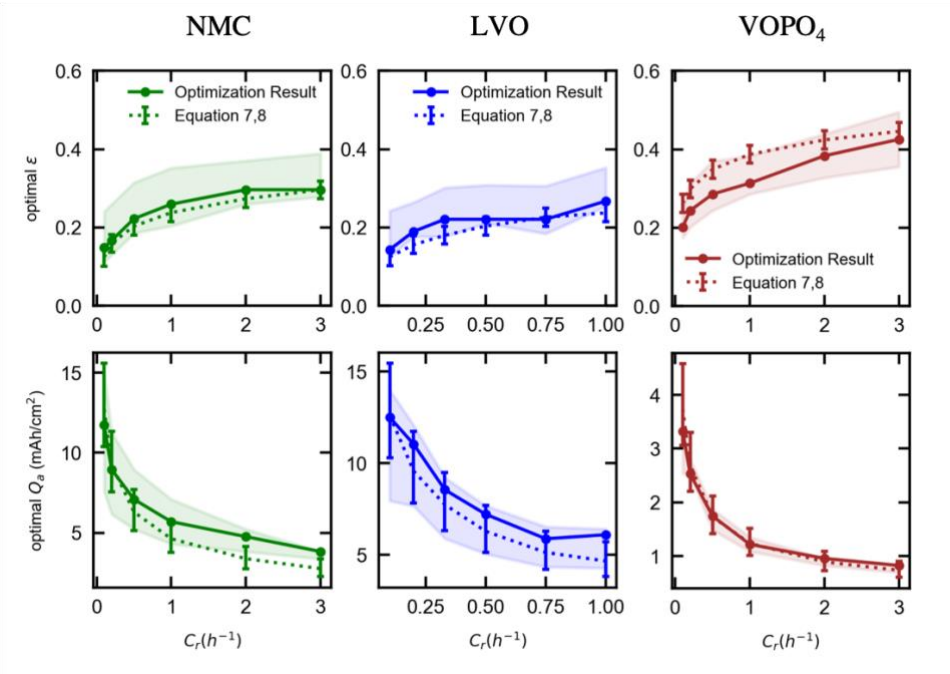

Figure 3.8 Simulated optimal design results and correlation predictions as a function of C_r. Solid lines show optimization results, and the shaded regions indicate parameter values to achieve 95% of maximum E_V. The dashed lines are calculated using Equation 3.7, 3.8, combined with material specific properties. Error bars describe the optimization results with an assumption of $\pm$ 50 % uncertainty in tortuosity.

As a means of understanding Equations 3.7 and 3.8, a dimensional analysis on a representative model[55] was conducted, and the dimensionless capacity is given by

$$\overline{Q_a} = \frac{C_r Q_a L_{cathode} \tau}{D_0 c_0 F \epsilon} \qquad \text{Equation 3.9}$$

where $L_{cathode}$ can be replaced using Equation 3.3,

$$\overline{Q_a} = \frac{C_r \tau Q_a^2}{V_{AM} D_0 c_0 F Q_{cathode} \rho_M \epsilon} \qquad \text{Equation 3.10}$$

Physically, $\overline{Q_a}$ can also be understood as an applied current density normalized by a limiting current density. Rearranging Equation 3.10 suggests the correlation 3.8, in which Q_a is inversely proportional to $\sqrt{k_\epsilon C_r \tau/(F D_0 c_0)}$.

The practical use of Equations 3.7 and 3.8 may be problematic when the porosity-tortuosity relation is not known with certainty. We explored through simulations how a poorly characterized tortuosity may create uncertainty in the optimal porosity and loading. In Figure 3.8, the uncertainty in the optimal design parameters assuming a 50% uncertainty in τ are represented by error bars, and the results are overlaid on the optima as determined by the physics-based modeling results, on which the correlation was trained. In most cases, the resulting range of recommendations from the correlation lie still within 95% of the maximum achievable E_V, designated by the shaded regions in Figure 3.8.

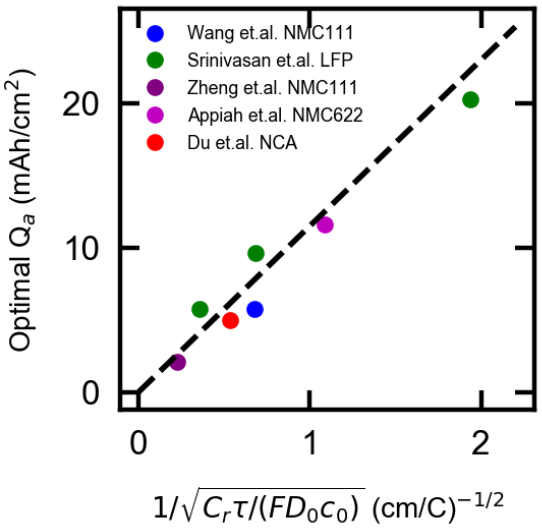

Figure 3.9 Compare general design results on optimal Q_a (same black dashed line in Figure 3.7b) with optimization results on specific material from others' study. Legend shows the source of study, the type of active material been optimized and the performance metric that they optimized for.

Figure 3.9 shows the comparison between Equation 3.8 and optimization results on specific electrode reported by others[26, 59, 73-75]. Equation 3.8 suggests optimal Q_a that is close to previously reported results, even for optima derived with slightly different constraints. Also, the correlation

seems to apply also to NCA, NMC_{622}, and LFP not studied directly in the development of the present correlation.

3.4.4 Assuming limitation on low porosity

According to Figure 3.7a, the optimal porosities for cells at low C_r are less than 0.2, which may be hard to reach due to practical limitations. For instance, for close packed solid spherical particles, the lowest porosity is 0.26. Thus, at the lower C_r, the low, optimal porosities may not be readily achievable. Therefore, Figure 3.10 shows the optimization results obtained if the porosity is assumed to be fixed. The optimal cell E_V for a fixed porosity of 0.26 and 0.35 (Figure 3.10a) is normalized by the value obtained by varying both porosity and loading, as in Figure 3.2. It is seen that the loss in performance is minimal at high C_r, and is less than 10 % at low C_r. Figure 3.10b shows that the optimal capacity loading deviates significantly from the results in Figure 3.2 (reproduced as the red line) at low C_r. However, as suggested in Figure 3.2, the optimal cell E_V is relatively insensitive to porosity and loading at low C_r. Practically, setting Q_a = 20.21 mAh cm^{-2} at C/10 when fixing porosity at 0.35 instead of using Q_a = 11.74 mAh cm^{-2} for freely varying ε, diminishes E_V only by 8.68 %.

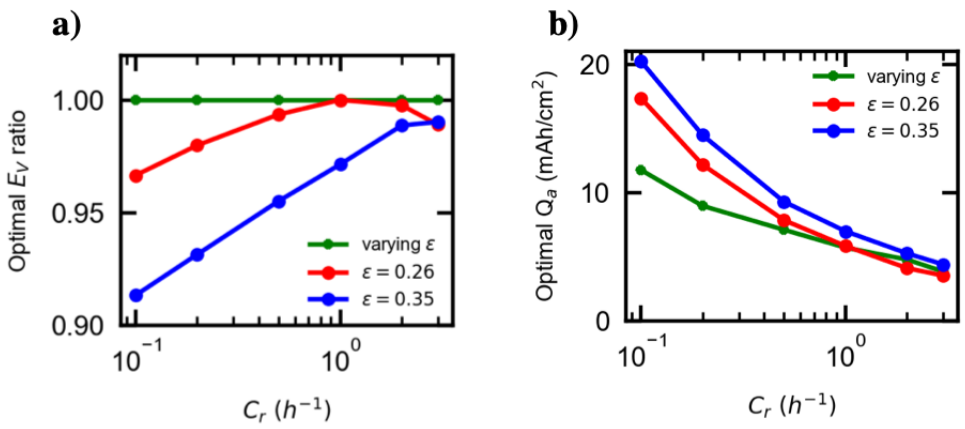

Figure 3.10 (a) (Optimal cell E_V assuming ε is constant) / (Optimal cell E_V assuming ε is free to vary). (b) Optimal capacity loading under different ε assumptions.

3.5 Conclusions

Batteries are complex, multi-scale systems, and transport impedances on different scales affect performance. With experimentally validated multiscale physics-based models, this work reveals that the optimization of battery's electrode-scale ion transport is not affected by the material properties on the smaller scales. Taking into account the salt diffusivity, salt concentration and electrode tortuosity, generalized electrode-scale optimization is applied to multiple electrodes, obtaining a simple correlation. Results show that the tortuosity is important to optimal design, but optimizations can be performed with reasonable certainty when the tortuosity estimation is in error by 50%. Correlations obtained in the present investigation can provide a guide for optimal design of other materials, as shown by comparison with the literature.

3.6 List of Symbols

c_0	Concentration of lithium in the electrolyte [mol cm^{-3}]
C_r	Current rate, 1/time need to fully charge/discharge the cell [h^{-1}]

D_0	Diffusion coefficient for lithium ions in bulk electrolyte, 1×10^{-6} [$cm^2\ s^{-1}$].
D_{agg}	Diffusion coefficient for lithium ions in secondary agglomerates [$cm^2\ s^{-1}$].
E_V	Volumetric energy density [$Wh\ L^{-1}$]
E_A	Areal energy density [$Wh\ cm^{-2}$]
F	Faraday's constant, 96485 [$C\ mol^{-1}$]
$i_{applied}$	Applied current density [$A\ cm^{-2}$]
k_ϵ	Constant in general correlation expression, 11.94 [$C\ cm^{-1}$]
k_Q	Constant in general correlation expression, 38.03 [$mAh\ cm^{-2}$]
L_{anode}	Thickness of anode [μm]
L_{agg}	Agglomerate size [μm]
$L_{separator}$	Thickness of separator, 25 [μm]
$L_{cc}^{cathode}$	Thickness of cathode current collector [μm]
L_{cc}^{anode}	Thickness of anode current collector [μm]
L_{BOC}	Total thickness of inert components (balance of cell), 50 [μm]
$L_{separator}$	Thickness of separator, 25 [μm]
M_A	Active material mass loading of cathodes [$mg\ cm^{-2}$]
Q_a	Capacity loading of electrodes [$mAh\ cm^{-2}$]
$Q_{cathode}$	Theoretical capacity of cathode material [$mAh\ g^{-1}$]
Q_{anode}	Theoretical capacity of anode material [$mAh\ g^{-1}$]
t_{dchg}	Discharge time [h]
V(t)	Cell Voltage as a function of time [V]
V_{AM}	Volume fraction of active material in terms of total electrode volume
V_{inert}	Volume fraction of inert additives in terms of total electrode volume
ϵ	Void fraction of porous electrode (porosity)
ϵ_{anode}	Porosity of graphite anode, 0.35
ρ_{AM}	Density of cathode active material [$g\ cm^{-3}$]
$\rho_{graphite}$	Density of graphite, 2.2 [$g\ cm^{-3}$]
σ	Electronic Conductivity [$S\ cm^{-1}$]

τ	Tortuosity of electrode
τ_{agg}	Characteristic time for agglomerate scale diffusion of lithium ion [s]

3.7 Supplementary Information

Table 3.2 Detailed information used in $VOPO_4$ model. For model fitting, The parameter estimation method followed the development of Brady *et al*[76]. A designated parameter space was sampled using Sobol sequences[37] and the residual sum of squares (RSS), describing how well the simulations emulate the experimental data, of each parameter set is summarized to show statistical distributions of parameter values.

[a)]Reversible Potential

$$U = U_{ref} + \frac{RT}{F}\ln\left[\left(\frac{c}{c_0}\right)\left(\frac{1-\bar{c}_{max}}{\bar{c}_{max}}\right)\right] + \sum_{k=0}^{11} A_k\left[(2\bar{c}_{max}-1)^{k+1} - \frac{2\bar{c}_{max}k(1-\bar{c}_{max})}{(2\bar{c}_{max}-1)^{1-k}}\right] \qquad \bar{c}_{max} = \frac{c_s - c_{s,0}}{c_{s,max} - c_{s,0}}$$

Parameter	Value	Parameter	Value	Parameter	Value
$c_{s,max}(mol\ cm^{-3})$	0.0120	A_3	-0.054168	A_8	0.434320
$U_{ref}(V)$	3.7679866	A_4	0.173909	A_9	0.377995
A_0	-0.234325	A_5	0.067128	A_{10}	-0.247347
A_1	-0.022042	A_6	-0.422896	A_{11}	-0.307939
A_2	-0.078171	A_7	-0.214427		

Parameter	Description	Value
[b)]$\boldsymbol{L_x}$	Crystal size (nm)	500
[c)]$\boldsymbol{D_x}$	Diffusion coefficient for lithium inside crystal ($cm^2\ s^{-1}$).	6.3×10^{-12}
[c)]$\boldsymbol{k_{rxn}}$	Reaction rate constant for charge transfer and insertion of lithium inside crystals ($cm^{5/2}\ mol^{-1/2}\ s^{-1}$)	3.3×10^{-7}

[a)]Measured by GITT experiments; [b)]Obtained from SEM; [c)]Obtained from model fitting

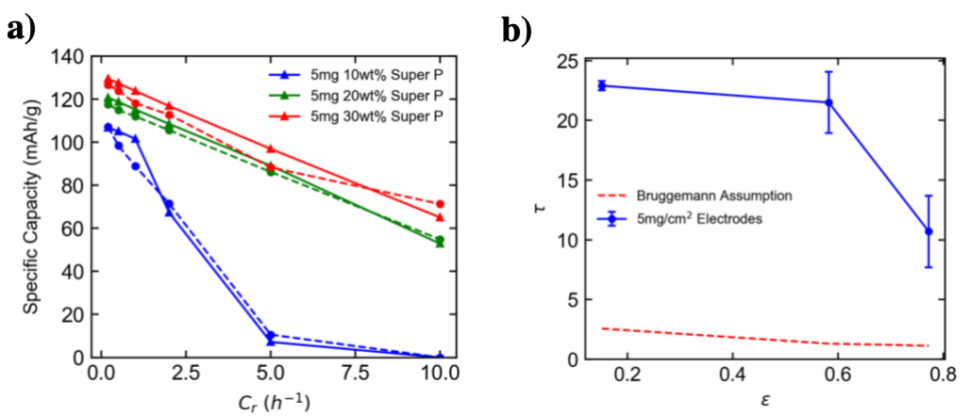

Figure 3.11 (a) Comparison of simulation results (solid) with experimental observations (dashed) on rate capability of $VOPO_4$ electrodes with mass loading of 5 mg cm^{-2} and with different wt% of Super P additive. (b) Tortuosity values measured by fitting model to discharge data with mass loading of 5 mg cm^{-2} and different wt% of Super P additive. Electrode porosity increases with increasing Super P additive fraction.

For construction of the $VOPO_4$ model (electrode-crystal P2D model), the same formulations in previous work[55] were adopted. Equations describing transport of lithium inside the $VOPO_4$ crystal are coupled to the electrode scale equations and solved simultaneously. The detailed thermodynamic potential as well as other parameters are shown in Table 3.2. Model was first fitted to discharge profiles (0.2C - 10C, 1C = 166 mA g^{-1}) of thin (29 μm, 1mg cm^{-2} mass loading) and porous (ε = 0.77) electrode (30 wt% Super P) to measure D_x and k_{rxn}, with results shown in Table 3.2. Then the model with known D_x and k_{rxn} were fitted to discharge profiles for electrodes with 5 mg cm^{-2} material loading and with different Super P fraction to measure the electrode tortuosity.

The agreement between experiment and simulations on electrodes' rate performance are shown in Figure 3.11a. The results of tortuosity estimation are shown in Figure 3.11b. Fitting a Bruggeman type relation to the porosity-dependent tortuosity results, we obtain:

$$\tau = 14.2 * \epsilon^{-0.266} \qquad \text{Equation 3.11}$$

This result was compared with ionic conductivity calculated by ionic resistances measurement by Ju *et al*[72] on the same electrodes. The back-calculated tortuosity from ionic resistance measurement agrees well with our estimation. For electrode with 5 mg cm^{-2} and 30 wt% Super P, the tortuosity calculated from ionic resistance measurement is 11.6, whereas our estimation suggests $\tau = 10.7 \pm 3.0$.

Chapter 4: Transport in and Optimization of Aligned-Channel Li-ion Electrode Architectures[‡]

[‡]This work has been published: Hui, Zeyu, Xiao Zhang, Karthik S. Mayilvahanan, Zhengyu Ju, Kenneth J. Takeuchi, Amy C. Marschilok, Esther S. Takeuchi, Guihua Yu, and Alan C. West. "Transport In and Optimization of Aligned-Channel Li-Ion Electrode Architectures." Journal of the Electrochemical Society 168, no. 10 (2021): 100536.
The thesis writer's contribution was the model development, data analysis and paper writing. The electrochemical data for the Li/aligned-channel electrode cells is provided by Xiao Zhang from Yu Group at University of Texas, Austin.

4.1 Introduction:

As high-performance renewable energy storage devices[45, 77], lithium-ion batteries (LIBs), commercialized in the early 1990s[78], have gained broad application in portable electronics[79] due to their high energy & power density, decent cycle life and environmental friendliness[14, 15, 80, 81]. Recently, the surging electric vehicles (EVs) market poses further requirements for the battery system[8, 82, 83]. Higher power density is required for high speed and fast acceleration[84], whereas higher energy density is needed to prolong cruising mileage[85] and to lower costs[86]. Improvements in battery power & energy density can be achieved by new active material sets[51, 87-89] and also by optimization of electrode design.

Optimizing electrode architectures[90-92] provides the opportunity of improving achievable cell energy & power density even in existing chemistries. For a battery with thick (high loading) porous electrodes, energy loss due to the transport limitations of lithium ions through a tortuous pathway may be significant[20, 93]. Accordingly, electrode-morphology designs providing low tortuosity electrolyte transport pathways have been actively explored[63]. Billaud et al.[94] adopted an Fe_3O_4 decorated graphite anode and used a magnetic field to form an out-of-plane aligned structure, which offers straight channels for Li^+ ion transport. Zhu et al.[95] reported evaporation-induced assembly of $VOPO_4$ 2D nanosheets. Li et al.[96] used Fe_3O_4 nanoparticles as a sacrificial phase to create aligned pores inside $LiCoO_2$ electrodes under external magnetic field. Lu et al[97] made use of woods as templates and created uniform straight channels inside $LiCoO_2$ electrodes. Zhang et al.[71] adopted an ice-templating method to produce vertically aligned Fe_3O_4 electrodes.

These studies produced low tortuosity aligned channels for lithium transport and successfully improved active material loading and cell-rate performances. However, introducing a large volume percentage of aligned channels also reduces the overall electrode density, leading

to tradeoffs in cell volumetric energy density[98]. Consequently, understanding the relationship between aligned channel electrode morphology and ion transport rate is key to optimization of the design towards the highest energy density.

In this study, an experimentally validated physics-based P2D model is used to interpret the lithium transport rate inside the positive electrodes with complex pore architectures. By parameterizing the electrode-scale ion transport coefficients M_{eff} of electrodes with aligned pores, a relation between electrode morphology and the ion transport coefficient is shown to be in agreement with experiment. The resulting correlation is used for numerical optimization, and this provides insights into when aligned-channel electrode architectures may be practically beneficial.

4.2 Theory:

The physics-based continuum model used in this study follows the development by Doyle and Newman et al.[11], modified by a finite-volume numerical method that allows for a more general treatment of the multi-scale transport. A detailed description and validation of the NMC cathode model is given by Hui et al[55], and that model is used without modification to charge-transfer or thermodynamic parameters. Furthermore, a model of $VOPO_4$, described in the authors' previous study[99], is used for analysis of $VOPO_4$ aligned channel measurements.

4.2.1 $VOPO_4$ aligned-channel electrode

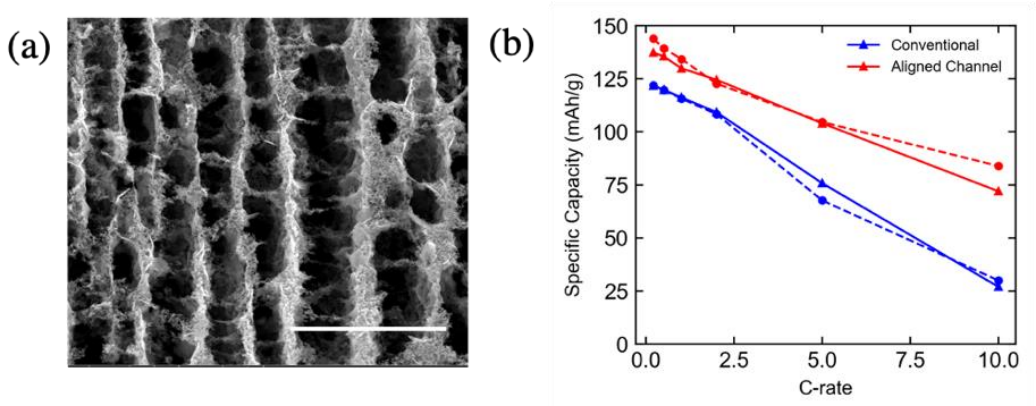

Figure 4.1 (a) Morphology of aligned channel $VOPO_4$ electrode via ice-templating. Scale bar is 25 μm. (b) Rate performance of conventional electrode and an aligned-channel electrode with morphology as shown on (a). Dashed lines are experimental observations, and solid lines are model predictions, where 1C = 166 mA g^{-1}.

Figure 4.1a shows the morphology of aligned-channel electrodes that use $VOPO_4$ nanosheets as the active material, with experimental details listed in a previous study, with details discussed in Chapter 2[72]. By introducing aligned channels via an ice-templating technique, significant improvement in rate performance was observed (Figure 4.1b), presumably due to the facilitated electrode-scale ion transport along the straight ice channels. To quantify the improvement, the model was first trained by discharge voltage profiles of Li/Conventional $VOPO_4$ electrode half-cell to estimate values of effective electrode-scale lithium diffusion coefficient D_{eff}, crystal-scale lithium diffusion coefficient D_x, and reaction rate constant k_{rxn}. The detailed simulation voltage profiles are shown in Appendix. As shown in Figure 4.1a, the aligned-channel electrode has wide straight channels for electrolyte transport, leading to a higher D_{eff}. Assuming that the ion transport across the thin solid material wall (~1-2 μm) has negligible impedance, the electrode scale lithium-ion effective diffusion can be expressed as:

$$D_{eff} = \frac{\epsilon_{ch}}{\tau_{ch}} * D_0 \qquad \text{Equation 4.1}$$

where ϵ_{ch} is the volume fraction of aligned channels (0.9 for the $VOPO_4$ electrode), τ_{ch} is the tortuosity of the channel (assumed to be 1.0) and D_0 is the bulk diffusivity of the lithium salt (assumed to be $1 \times 10^{-6}\ cm^2/s$). A model is established from measurements of a cathode with active material mass loading (10 mg/cm^2) and thickness (800 µm) of the aligned channel electrode, with the same reaction-rate parameters and crystal-scale diffusivity derived from conventional electrodes, and Equation 4.1 to describe the electrode-scale mass transport. As shown in Figure 4.1b, the model gives good prediction on the rate performance of the aligned channel electrode.

4.2.2 Tunable aligned-channel architecture

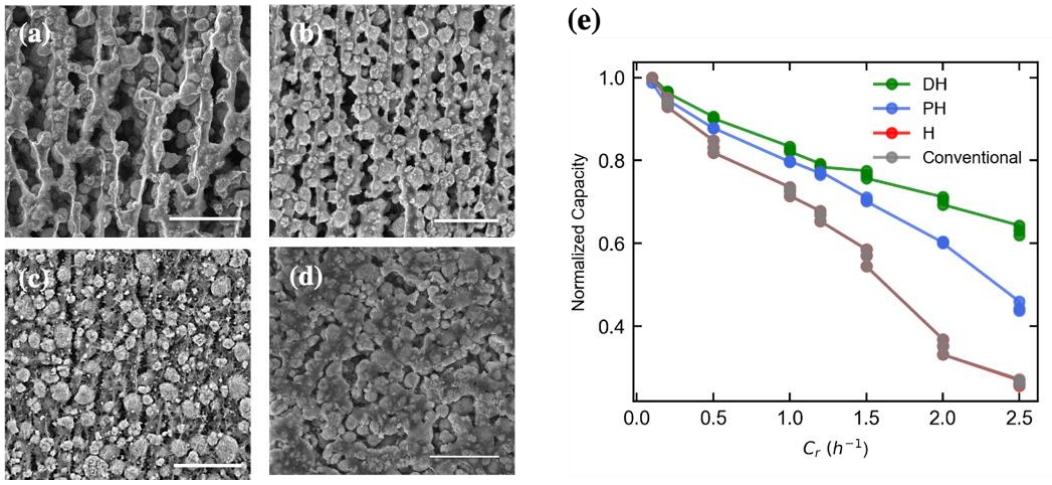

Figure 4.2 (a)-(d) Morphology of NMC111 electrodes prepared conventionally and under different ice-formation conditions (a): DH, (b): PH, (c): H, (d): Conventional electrodes. The scale bar is 50 μm. (e) Rate performance of different electrodes. The discharge capacity is normalized by the discharge capacity at C/10 rate. 1C = 150 mA g^{-1}.

Equation 4.1 was not applicable when the width of the porous channel walls increased significantly because the ion transport impedance through the wall cannot be neglected. As Figure

4.2 a-c shows, aligned-channel electrodes with different channel and porous wall widths were fabricated via ice-templating, using $Li_xNi_{1/3}Mn_{1/3}Co_{1/3}O_2$ (NMC111) as active material. By mixing water with different organic solvents, the ice growth rate and surface tension was tuned, thus forming different architectures. The electrode with DMSO-H_2O mixed solvents (DH, Figure 4.2a) yields wide channels (10-20 μm) with walls between 5 and 10 μm, while a 1-propanol-H_2O mixed solvent (PH, Figure 4.2b) creates thicker walls (10-20 μm) with similar channel widths (10-20 μm). In comparison, thick walls (>20 μm) and small channels (5-10 μm) were observed in samples that use H_2O solvent (H, Figure 4.2c). Differing architectures lead to different electrochemical rate performance shown in Figure 4.2e, with the DH electrodes having the best rate performance and the H electrodes showing no obvious improvement over drop-cast electrodes.

4.2.3 Three-domain ion transport & Dimensional Analysis

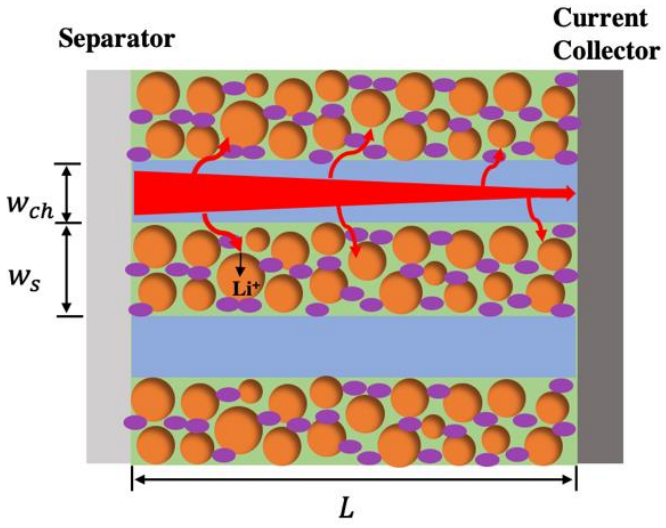

Figure 4.3 Schematic diagram of electrode-scale ion transport on different length scales of the aligned channel structure. The walls contain orange-spheres representing the active material NMC and purple structures representing binder. Aligned channels (light blue) are primarily comprised of electrolyte.

As illustrated by Figure 4.3[100], mass transport over three domains is considered to be possibly limiting performance. Channel transport (large red arrow) refers to the transport of ions inside the aligned channels. Wall transport (small red arrows) describes the diffusion of Li through the porous material walls. Agglomerate scale transport (black arrow) has been well characterized in previous work and is the transport of lithium through secondary agglomerates formed by primary crystals. A dimensionless current ($\bar{I}$) can compare the transport rate of lithium over each pathway[101]. Physically, $\bar{I}$ can be understood as the applied current density along a given path normalized by the diffusional limiting current density, with a higher value indicating a more sluggish ion transport process. Detailed equations to calculate dimensionless currents are listed in Table 4.1.

Table 4.1 Equations for calculating dimensionless current on three length scales.

$\bar{I}^x = \frac{i_{app}^x}{i_{lim}^x}$	**Channel Transport**	**Wall Transport**	**Agglomerate Scale Transport**
Applied Current	$i_{app}^{ch} = Q_a * C_r$	$i_{app}^{s} = \frac{i_{app}^{ch}(w_s + w_{ch})}{2L}$	$i_{app}^{agg} = \frac{Q_a * C_r L_{agg}}{3L(1-\epsilon_{ch})}$
Diffusional Limiting Current	$i_{lim}^{ch} = F * \left(\frac{\epsilon_{ch} D_0 c_0}{L}\right)$	$i_{lim}^{s} = F * \left(\frac{\epsilon_s D_0 c_0}{\tau_s w_s/2}\right)$	$i_{lim}^{agg} = F * \left(\frac{D_{agg} c_0}{L_{agg}}\right)$

Table 4.2 Dimensionless current on three length scales at 1.0 C. $Q_a = 150\ mAh\ g^{-1} * 20\ mg\ cm^{-2} = 3\ mAh\ cm^{-2}$. $\tau_s = 40$. w_{ch} and w_s value ranges are obtained from the SEM images of different electrodes. $\epsilon_{ch} = w_{ch}/(w_{ch} + w_s)$.

	L (μm)	w_{ch} (μm)	w_s (μm)	L_{agg} (μm)	ϵ_{ch}	ϵ_s	$\bar{I}_{ch}$ @1.0C	$\bar{I}_s$ @1.0C	$\bar{I}_{agg}$ @1.0C
DH	270	10-20	5-10	5	0.5-0.8	0.2-0.65	1.05-1.68	0.04-0.08	1.72
PH	270	10-20	10-20	5	0.5-0.67	0.55-0.65	1.26-1.68	0.06-0.14	1.72
H	270	5-10	20-80	5	0.06-0.33	0.7-0.8	2.54-14.0	0.10-0.98	1.72

Table 4.2 shows the detailed dimensionless current results. The increasing trend in $\bar{I}_{ch}$ from DH to PH and H indicates the rising impedance of ion transport through the aligned channels due to the reduction in channel width (w_{ch}). Moreover, because of the increasing porous wall width (w_s), ion transport impedance through porous wall ($\bar{I}_s$) is also seen to increase. The increasing values of $\bar{I}_{ch}$ and $\bar{I}_s$ are the sources of deteriorating rate performance from DH to PH and H electrodes.

The analysis is insightful, but mass-transfer pathways are distributed throughout the complex electrode architecture, and the wall and channel mass-transfer resistances may not be simply described as being connected in either series or parallel. For this reason, an electrode-scale ion transport factor M_{eff} is introduced, with a value obtained by fitting to experimental constant current discharge data at different current rate:

$$D_{eff} = \frac{D_0}{M_{eff}} \qquad \text{Equation 4.2}$$

Values of M_{eff} describe some combination of the wall and channel mass-transfer resistances, which is connected to channel morphology (w_{ch} and w_s) in the Discussion section.

4.3 Results

4.3.1 Fitting model to DH

D_{agg} and M_{eff} were estimated using discharge voltage profiles of a Li/DH half-cell and the P2D model. The reaction rate constant k_{rxn} is assumed not to change. In addition, the electronic conductivity σ is assumed to be reasonably high ($3.0 \times 10^{-2}\ S/cm$) given that enough conductive

carbon is added, exceeding the electronic percolation limit[65, 66]. Under such conditions, the precise value of σ does not impact performance.

The resulting estimated parameter values for DH electrode are $D_{agg} = (14 \pm 2) \times 10^{-10}\ cm^2/s$ and $M_{eff} = 16.5 \pm 2.1$. Figure 4.4 shows the agreement between simulations and experimental observations. Solid curves in Figure 4.4 are the simulation results assuming the most probable value of D_{agg} $(14 \times 10^{-10}\ cm^2/s)$ and M_{eff} (16.5), while the shaded contours illustrate the uncertainty region resulting from uncertainty of parameter estimation. Most of the experimental voltage profiles agree well with simulation results, falling in the zones of parameter uncertainty.

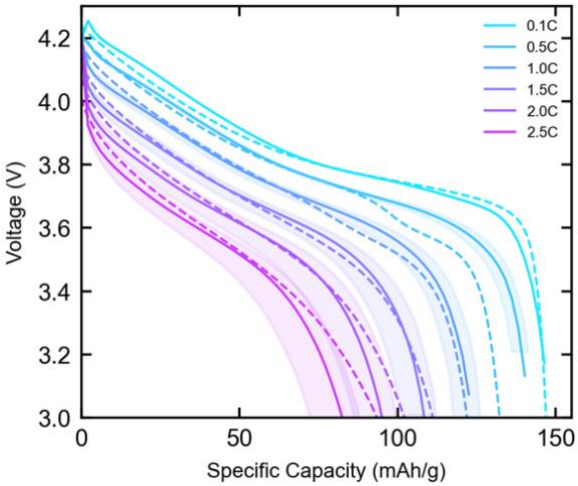

Figure 4.4 Discharge voltage profiles for Li/DH half-cell. The DH electrode has a loading of 20 mg/cm^2 and thickness of 270 μm. Dashed lines are experimental observations, and solid lines are simulation results. Shaded contours are the uncertainty region from the uncertainty of parameter estimations listed in Table 4.2.

The estimated D_{agg} agrees well with our previous study[55], indicating that the improved performance of aligned channel structures comes from the facilitated electrode-scale ion transport,

with agglomerate scale unaffected. Accordingly, simulations on PH, H, and conventional slurry cast electrodes use the same D_{agg} value and only vary M_{eff}.

4.3.2 PH, H and Conventional electrodes

Table 4.3 Model estimated M_{eff} for different electrodes.

Electrode	M_{eff}
DH	16.5 ± 2.1
PH	22.0 ± 2.3
H	42.5 ± 4.1
Conventional	47.9 ± 5.0

The M_{eff} values of PH, H and conventional electrodes were then estimated by comparing simulations with discharge data of PH, H and conventional electrodes half-cells (vs. Li metal) with the same active mass loading (20 mg/cm^2). Simulation results are shown in Figure 4.5 a-c, and the resultant M_{eff} are listed in Table 4.3. Figure 4.5d plots the simulated capacity of different electrodes to compare with experiment. The results in Table 4.3 show a rising trend in the electrode-scale mass transport coefficient M_{eff} from DH to PH and H, suggesting an increasingly sluggish electrode-scale ion transport. As introduced in the previous section, this results from a combining effect of rising $\bar{I}_{ch}$ due to reduced channel width w_{ch} and increasing $\bar{I}_s$ due to increased porous wall width w_s. The conventional electrode illustrates an extreme case, with zero w_{ch} leading to the highest M_{eff}.

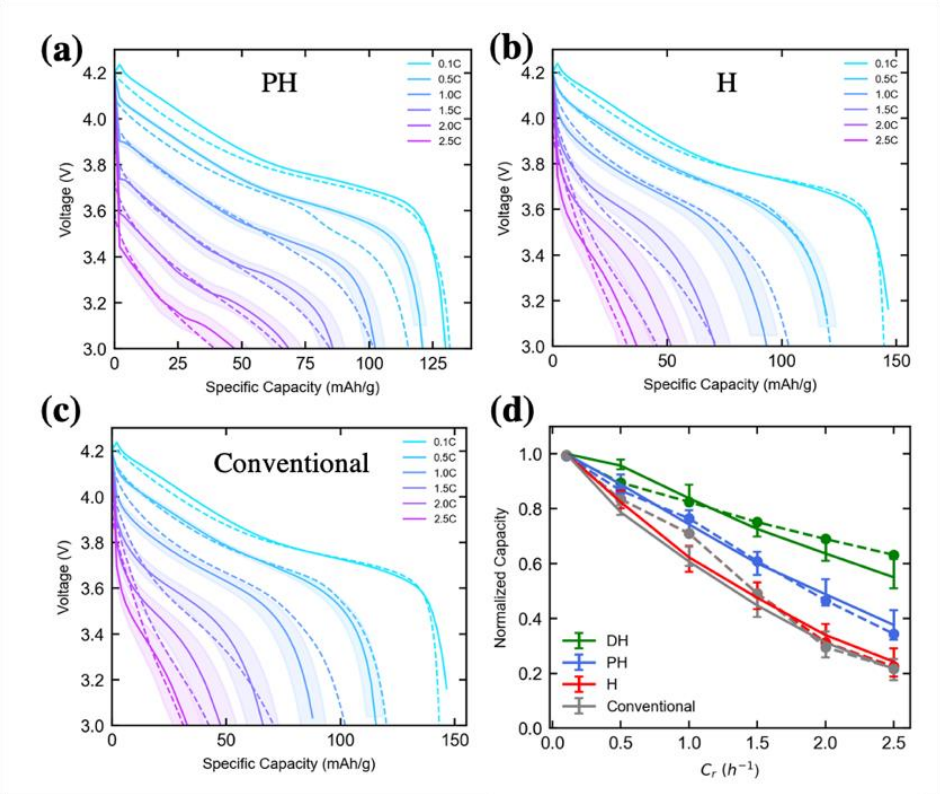

Figure 4.5 (a)-(c) Discharge voltage profiles of PH, H and Conventional half-cell. For PH electrode, the electronic conductivity is measured to be $1.3 \times 10^{-3}\ S\ cm^{-1}$, which is 23 times lower than the other electrodes. (d) Rate performance of different electrodes. The discharge capacity is normalized by the discharge capacity at C/10 rate. All the dashed lines are experimental data, and solid lines with error bars corresponding to shaded regions on the other figures are simulation results.

4.4 Discussion

4.4.1 Higher ϵ_{ch} not always favorable

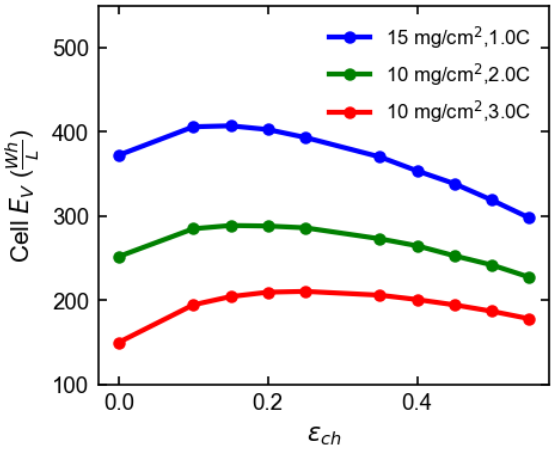

Figure 4.6 Simulated Cell E_V as channel fraction ϵ_{ch} changes. Assumptions: $\tau_s = 30$ and $\epsilon_s = 0.625$. Counter electrode: graphite electrode with a porosity of 0.35 and total capacity equal to the cathode. The NMC cathode mass loadings shown in the legend are the mass loadings leading to highest E_V for each c-rate. Total thickness of separator and current collectors is set to be 50 μm.

The previous section shows that the electrode-scale mass transport impedance (represented by M_{eff}) depends on the aligned channel structure. Wider channels with thinner walls lead to lower M_{eff}. However, the introduction of wide aligned channels also reduces the volume fraction of active material, thus potentially reducing cell volumetric energy density (E_V). This leads to an optimal volume fraction of channels. As Figure 4.6 shows, the energy density E_V initially increases with ϵ_{ch}, and then decreases. The channel volume fraction that gives the maximum E_V is also seen to be a function of applied current rate (C-rate). Note that the assumed mass loading at 1C is less than it is at 2C and 3C because the optimal mass loading also varies with C-rate. Simultaneous optimization of the architecture parameters is discussed below. Generally, the numerical

optimization of aligned-channel electrode design requires a correlation between M_{eff} and the electrode architecture.

4.4.2 Correlation between M_{eff} and electrode architecture

As shown by Figure 4.2, if we assume that the wall and channels are resistances in series[100, 102], we obtain

$$\frac{1}{D_{eff}} = \frac{w_{ch}+w_s}{w_{ch}D_{eff,ch}+w_sD_{eff,s}} \qquad \text{Equation 4.3}$$

where $D_{eff,ch}$ & $D_{eff,s}$ are effective ion diffusion coefficients in each phase, related to morphology parameters by:

$$D_{eff,ch} = \frac{D_0}{\tau_{ch}} \qquad \text{Equation 4.4}$$

$$D_{eff,s} = \frac{\epsilon_s D_0}{\tau_s} \qquad \text{Equation 4.5}$$

in which τ_{ch} & τ_s are unknown effective tortuosity in each phase and ϵ_s is the wall porosity. When w_{ch} = 0, then $D_{eff} = D_{eff,s}$, which is the effective ion diffusion coefficient in a conventional electrode, and

$$M_{eff,0} = \frac{D_0}{D_{eff,s}} = \frac{\tau_s}{\epsilon_s} \qquad \text{Equation 4.6}$$

Combining Equations 4.2-4.6, the correlation between M_{eff} and morphology parameters is expressed as:

$$M_{eff} = \epsilon_{ch} * \tau_{ch} + (1-\epsilon_{ch})M_{eff,0} \qquad \text{Equation 4.7}$$

where the volume fraction of aligned channel is assumed to be given by $\epsilon_{ch} = \frac{w_{ch}}{w_{ch}+w_s}$.

The value of $M_{eff,0}$ for the conventional electrode ($\epsilon_{ch} = 0$) is large, suggesting an apparently high tortuosity ($\tau_s = 30$) of the conventionally prepared electrodes, and the exact cause of this higher tortuosity is not known but a key feature in the electrode fabrication is the use of a water-soluble binder. Previous works indicate that optimization of the binder may significantly impact electrode performance.[103, 104] Because of the large value of $M_{eff,0} = 48$, the precise value of channel τ_{ch} does not impact the slope and is indeterminant from this study. Assuming that the tortuosity of aligned channel τ_{ch}=1.0, we compare the Equation predicted M_{eff} (dashed line) of DH, PH and H electrodes with M_{eff} values (points) measured by the P2D model (Table 4.3). As Figure 4.7 shows, the M_{eff} values are predicted by Equation 4.7. This correlation is then used in guiding the design of aligned channel structure towards optimal energy density, as discussed in the next section.

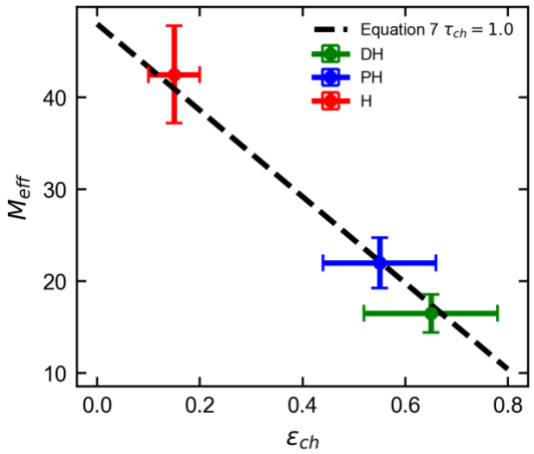

Figure 4.7 Comparison of M_{eff} values measured by the model (colored dots with error bar) and M_{eff} values predicted by Equation 4.7 (Black dashed line), assuming $M_{eff,0} = 48$. The error bars of M_{eff} come from the uncertainty in parameter estimations, as shown in Table 4.3, while the error bars of ϵ_{ch} are due to the uncertainty in measuring the volume fraction of aligned channels.

4.4.3 Optimize aligned-channel electrode design

Adopting the optimization approach introduced in a previous study[64, 99], we optimize the design of Graphite/NMC111 cells assuming conventional electrodes and aligned-channel electrodes, respectively. For simplicity, we assume that the wall porosity (ϵ_s) of aligned channel electrodes is not adjustable, but the channel volume fraction ϵ_{ch} and mass loading can be controlled. Equation 4.7 is used to estimate M_{eff} from ϵ_{ch}, assuming $\tau_{ch} = 1$, which maximizes the improvement of M_{eff} by the channels.

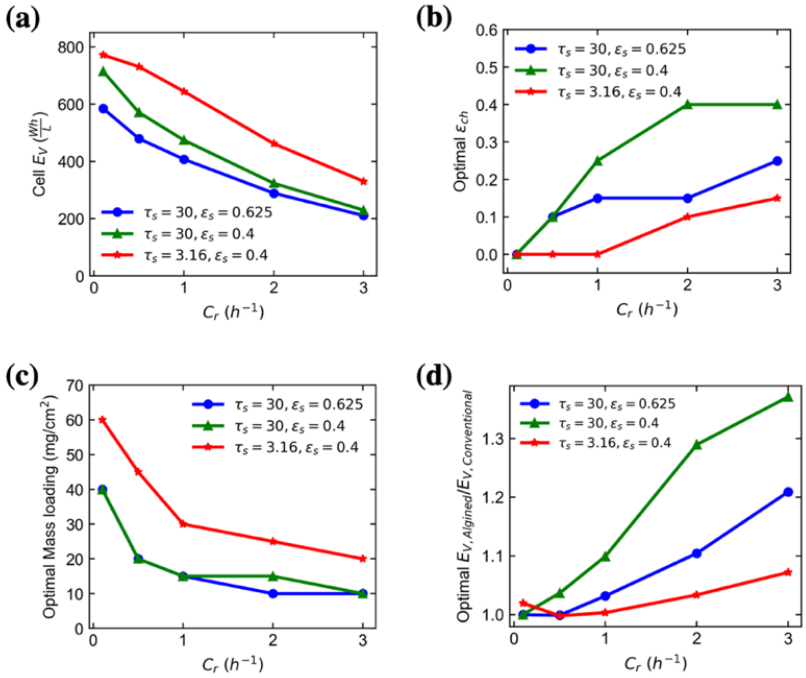

Figure 4.8 (a)-(c) Comparison of optimization results on aligned-channel electrodes with different assumptions on the wall transport. w_s is assumed to be 6 μm in Aligned channel electrodes. Colors correspond to different assumptions of τ_s and ϵ_s in the porous wall (material walls for aligned-channel electrodes). (d) The ratio between optimal cell E_v of aligned channel electrodes and optimal conventional electrodes as a function of C-rate.

The optimization results for mass loading and channel volume fraction are shown in Figure 4.8. Blue curves show the results assuming $\tau_s = 30$ and $\epsilon_s = 0.625$, derived for the DH electrode.

Figure 4.8d plots the ratio of optimal cell E_V between aligned channel cells and conventional slurry-cast cells. Aligned channels (with optimal volume fraction ϵ_{ch} in Figure 4.8b) allow for higher loading electrodes without severe ion transport loss. For example, the optimal mass loading for a conventional cell at 2.0 C is 7.5 mg/cm^2, while the addition of aligned channels (optimal $\epsilon_{ch} = 0.15$) increases the optimal mass loading to 10.0 mg/cm^2. Such improvement in optimal loading increases the overall cell E_V (Figure 4.8d) given the constant volume of inert components. As Figure 4.8d also shows, the increasing optimal E_V ratio with current rate suggests that aligned-channel architectures are more effective for high power applications.

The green curves in Figure 4.8 a-c show results obtained by lowering $\epsilon_s = 0.4$, keeping an apparently high wall tortuosity ($\tau_s = 30$), which results in a higher $M_{eff,0} = 75$. A higher optimal ϵ_{ch} is observed, with minimal changes in optimal mass loading. As electrode fabrication methods are optimized, it may be possible to tune the porosity of the walls.

By optimizing fabrication, it is likely that the porous walls can be produced with a lower tortuosity τ_s, and this impacts both optimal ϵ_{ch} and mass loading, as shown by the red curves of Figure 4.8. Figure 4.8b shows that the optimal ϵ_{ch} is lower when the wall tortuosity decreases, which indicates that for low tortuosity electrodes, the improvement in optimal cell E_V by adding aligned channels is less pronounced, as also shown by Figure 4.8d. Thus, the properties of the porous walls are important in optimizing design of aligned channel structure. Reducing the porosity inside porous walls does not affect the optimal mass loading but leads to a larger optimal channel fraction (ϵ_{ch}), while the reduction in wall tortuosity changes both the optimal ϵ_{ch} and optimal mass loading.

4.4.4 Generalized optimization on material loading (Q_a)

Study in Chapter 3[99] showed that for a variety of cathode materials, the optimal capacity loading is given by a general correlation. Furthermore, the correlation was derived by a two-parameter optimization (Q_a and ϵ_s) and was shown to apply independent of the tortuosity dependence on porosity; it was also shown to be applicable to literature optimization results for a large range of cathode materials. We have since shown that correlation holds if ϵ_s is prescribed and a single parameter optimization on Q_a is performed.

By modifying the correlation in our previous study, the optimal Q_a for both conventional and aligned channel electrodes is given by

$$Q_{a,opt} = k_Q/\sqrt{k_\epsilon C_r M_{eff}/(F D_0 c_0)} \qquad \text{Equation 4.8}$$

where the constants $k_\epsilon = 11.94\ C\ cm^{-1}$, and $k_Q = 86.39\ mAh\ cm^{-2}$. Figure 4.9 shows that the optimal mass loadings follow the correlation (black dashed line) well, assuming M_{eff} is given by Equation 4.7. Results are shown for conventional electrodes and aligned channel electrodes, for two of assumed wall $M_{eff,0}$. Again, when the wall properties are more tortuous, the optimal ϵ_{ch} increases and optimal Q_a decreases.

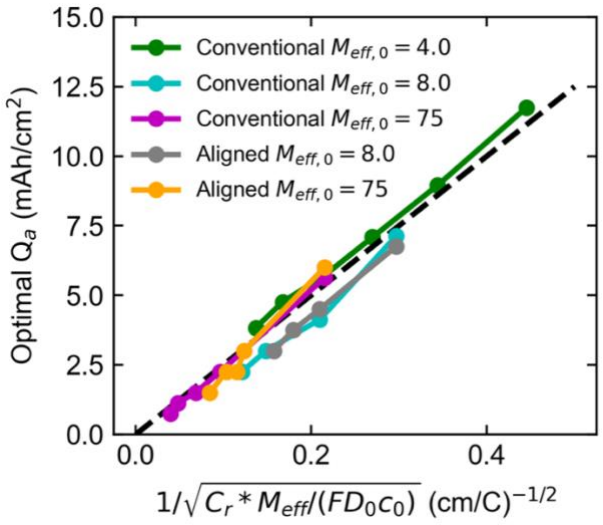

Figure 4.9 The optimal capacity loading as a function of the rescaled C- rate. Colors indicate different assumptions on τ_s. ϵ_s for all electrodes is assumed to be 0.4.

4.4.5 When is aligned-channel electrode helpful

Figure 4.8 demonstrates that the gains in E_V by using aligned-channel architectures depend on the transport properties of the porous wall $M_{eff,0}$ (assumed to be similar here to that of conventionally prepared electrodes). Figure 4.10a quantifies how the improvement in E_V is more significant for electrodes with higher $M_{eff,0}$. Furthermore, the improvement is more pronounced for cells running at higher current rates. Figure 4.10b shows the optimal channel volume fraction as a function of the electrode transport property $M_{eff,0}$. Combining Figure 4.10a and 4.10b, one can analyze the viability of introducing aligned channels from an economic perspective. For low $M_{eff,0}$, electrodes operating at low rates, the slight improvement in cell E_V by aligned channels could result in significant increase in the manufacturing cost.

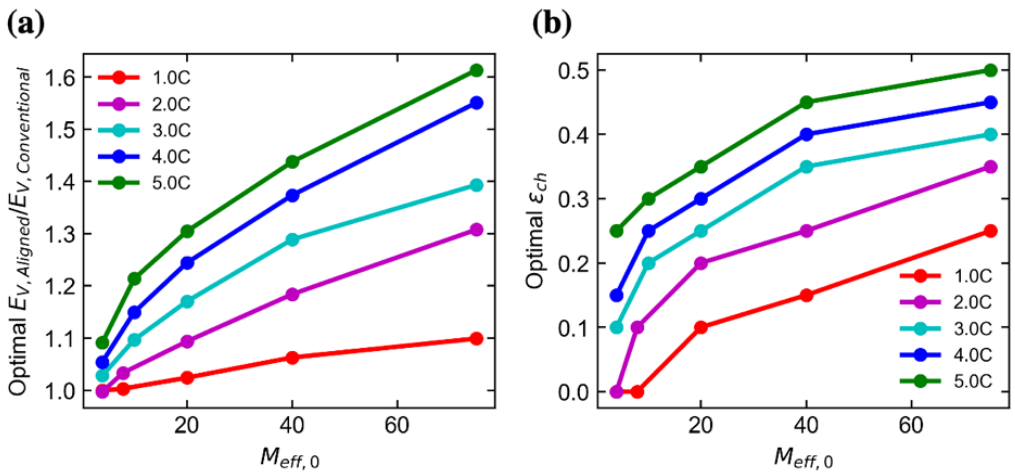

Figure 4.10 (a) Improvement in optimal cell E_V by aligned channel assuming different wall ion transport parameters for 1C to 5C. For both aligned channel and conventional electrodes, ϵ_s is assumed to be 0.4. The aligned channel electrodes are optimized by changing ϵ_{ch} and mass loading simultaneously, and conventional electrodes only varies mass loading. (b) Optimal ϵ_{ch} as a function of the wall transport property.

4.5 Conclusion

The impact of aligned channels on electrode-scale transport can be quantified by comparing battery performance data to P2D models. At least as a first approximation, the underlying results can be readily reconciled by mass-transfer resistances on the electrode scale as being comprised of two domains (aligned channels and porous material walls) in series. The correlation allows for the facile numerical optimization of aligned-electrode architectures. Results lead to optimal capacity loading and channel volume fraction. Optimal aligned-channel designs can achieve significant improvements in energy density for high power applications. Improvements are more pronounced when the apparent tortuosity of the electrode is higher.

4.6 Experimental

$VOPO_4$ Synthesis. Bulk $VOPO_4 \cdot 2H_2O$ was synthesized according to previous literature.[105] Briefly, a mixture of V_2O_5 (1.0 g), HNO_3 (69% 10 mL), H_3PO_4 (85%, 5 mL), and H_2O (20 mL) was refluxed at 115 °C for 16 h. The resulting yellow precipitate was collected by centrifugation, washed with acetone three times, then dried in open air for more than 24 h. $VOPO_4$ NSs were obtained by exfoliation of bulk $VOPO_4 \cdot 2H_2O$ in IPA. Typically, 200 mg bulk $VOPO_4 \cdot 2H_2O$ were dispersed in 100 mL IPA with a concentration of about 2 mg/mL. The yellow dispersion was ultrasonicated for 60 min in cold water until it turned to a light yellow and transparent dispersion. Then, IPA was removed by heating at 40 °C in a vacuum oven overnight and the resulting yellow powder was collected for further characterization.

Preparation of Drop-Cast $VOPO_4$ Electrodes. The drop-casted $VOPO_4$ electrodes were prepared by adding various amount of Super P as a conductive additive. First, 50 mg $VOPO_4$ NS powder was redispersed in 5 mL IPA with the help of ultrasonication for 30 min, forming a yellow transparent dispersion. Then, a specific amount of Super P was added and ultrasonicated for another 30 min to form a homogeneous mixture. After stirring to remove excess IPA, the mixture was thoroughly mixed in a Thinky centrifugal mixer to form a homogenous slurry, which was then cast on aluminum foil (1.13 cm^2) and dried in open air. The weight ratios of $VOPO_4$ NS/Super P are 7:3, 8:2, and 9:1, respectively.

Preparation of Ice-Templated $VOPO_4$ Electrodes. Ice-templated $VOPO_4$ electrodes were prepared by mixing $VOPO_4$ NS, Super P, and CMC-Na. ($VOPO_4$ NS/Super P/CMCNa = 7:2:1). First, 5 wt % CMCNa solution and Super P was added into deionized water/IPA (85:15 v/v) and mixed for 30 min in a Thinky centrifugal mixer. After that, $VOPO_4$ NS were added and mixed for another 15 min. The slurry was cast on the ozone-pretreated Al foil and placed on a copper plate,

followed by freezing with liquid nitrogen. Electrodes were then transferred to a lyophilizer and ice was removed under 5 bar at −48 °C for over 24 h.

NMC111 Electrode Slurry Preparation. NMC111 ($LiNi_{1/3}Co_{1/3}Mn_{1/3}O_2$) (density 2.3 g/cm^3) and Super P (density 1.8 g/cm^3) were purchased from MTI Corp. NMC111 powder was subjected to 800 ºC calcination in air for 1h before use. CMC-Na (sodium carboxymethyl cellulose) was purchased from Sigma-Aldrich (density 1.6 g/cm^3). To prepare electrode slurries, 400 mg 5% wt CMC-Na aqueous solution was mixed with 10 mg Super P in the Thinky Mixer for 30 min. 300 mg NMC powder and 20 mg Super P were grinded in mortar. The mixed NMC/Super P powder was added to CMC-Na/Super P slurry and the resulting mixture was subjected to Thinky Mixer for 5 min. For DH, PH and H electrodes, 20 μL of DMSO, 1-propanol and H_2O were added to the resulting electrode slurry and then mixed in Thinky Mixer for another 2 min, respectively. For the slurry-cast thick film electrodes, the slurry only using H_2O as solvent was directly casted onto Al foil and dried.

Ice-Templating Process. The slurry was coated onto pre-cut Al foil current collectors and subjected to a PDMS wedge on a cold finger, where the bottom of the cold finger was immersed into liquid nitrogen. After the freezing process was completed, the electrode samples were freeze-dried overnight, followed by vacuum oven drying at 90 ºC overnight.

Cell assembly. CR2032 coin cell assembly was carried out in an argon-filled glovebox with lithium metal as anode and reference electrode. Celgard 2320 was used as separator between cathode and anode. The electrolyte was 1.0 M $LiPF_6$ dissolved in a mixture of ethylene carbonate and diethylene carbonate with 1:1 ratio. All electrochemical tests were conducted at room temperature (25 °C) with a voltage range 2.8-4.25 V.

Sample characterization. Scanning electron microscope, STEM (Hitachi S5500) and SEM (TESCAN VEGA3) were used to characterize the morphology of the samples. Rate performance and cycling tests of the as-assembled coin cells were performed using a Neware battery tester (BTS 4000).

4.7 Acknowledgments

This research was supported as part of the Center for Mesoscale Transport Properties, an Energy Frontier Research Center supported by the U.S. Department of Energy, Office of Science, Basic Energy Sciences, under award #DE-SC0012673 for financial support. EST acknowledges the William and Jane Knapp Chair of Energy and the Environment.

4.7 List of Symbols

c_0	Lithium concentration inside the electrolyte, 0.001 [mol cm^{-3}]
C_r	Current rate, 1/time need to fully charge/discharge the cell [h^{-1}]
D_0	Diffusion coefficient for lithium ions in bulk electrolyte, 1×10^{-6} [cm^2 s^{-1}].
D_{agg}	Diffusion coefficient for lithium ions in secondary agglomerates [cm^2 s^{-1}].
D_{eff}	Effective diffusion coefficient of lithium ions through the electrode [cm^2 s^{-1}].
$D_{eff,ch}$	Effective diffusion coefficient of lithium ions through the channels [cm^2 s^{-1}].
$D_{eff,s}$	Effective diffusion coefficient of lithium ions through the wall [cm^2 s^{-1}].
D_x	Diffusion coefficient for lithium in primary active material crystals [cm^2 s^{-1}].
E_V	Volumetric energy density [Wh L^{-1}]
F	Faraday's constant, 96485 [C mol^{-1}]
$\bar{I}$	Dimensionless Current
i_{app}	Applied current density for different steps [A cm^{-2}]
i_{lim}	Diffusional limiting current density for different steps [A cm^{-2}]

k_{rxn}	Reaction rate constant for delithiation / lithiation [$cm^{5/2}$ $mol^{-1/2}$ s^{-1}]
k_Q	Constant in general correlation expression, 86.39 [mAh cm^{-2}]
k_ϵ	Constant in general correlation expression, 11.94 [C cm^{-1}]
L	Thickness of electrode [μm]
L_{agg}	Agglomerate size [μm]
M_{eff}	Electrode-scale ion transport coefficient
$M_{eff,0}$	Ion transport coefficient in porous material wall
Q_a	Capacity loading of electrodes [mAh cm^{-2}]
$Q_{a,opt}$	Capacity loading of electrodes that gives optimal E_V [mAh cm^{-2}]
R	Ideal gas constant [8.314 J mol^{-1} K^{-1}]
R_{ion}	Electronic resistance of electrode [Ω cm^{-2}]
T	Temperature [298 K]
t_+	Cation transference number [0.5]
t_-	Anion transference number [0.5]
w_{ch}	Average width of aligned channel [μm]
w_s	Average width of porous material wall [μm]
ϵ_{ch}	Volume fraction of aligned channels (porosity)
ϵ_s	Porosity inside the porous material wall
κ	Electrolyte ionic conductivity [S cm^{-1}]
σ	Electronic conductivity [S cm^{-1}]
τ_{ch}	Average tortuosity of aligned channels
τ_{agg}	Characteristic time for agglomerate scale diffusion of lithium ion [s]

4.8 Supplementary Information

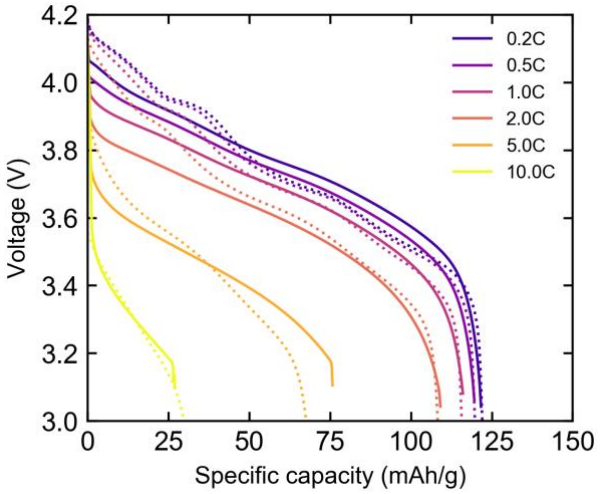

Figure 4.11. Voltage profiles of Li/$VOPO_4$ (conventional slurry-cast) cell at different current rates. Dashed lines are experimental observations. Solid curves are simulation results. Mass loading of $VOPO_4$ electrode is 10 mg/cm^2. Thickness is 190 μm.

The model for Li/$VOPO_4$ electrode uses the formulations in Chapter 2, which couples electrode-scale equations to agglomerate-scale equations describing lithium transport on the crystal scale. Figure 4.11 show the simulation results (solid lines), which give good prediction on experimental performance (dotted lines).

Chapter 5: Electrochemical Characterization of Degradation Modes of High-Voltage NMC Electrodes

5.1 Introduction

With the recent surge of electric-vehicle (EV) market[8, 106, 107], the next-generation lithium battery is required to have improved energy density[2, 108], safety[109, 110] and longevity[111, 112]. To improve the energy density of current LIBs system, a major focus has been put on the negative electrode side, by replacing the graphite anode with a stable lithium metal foil[10, 113-115]. In the meantime, pairing a high-voltage cathode to the lithium metal anode can further increase cell energy density [116, 117]. Recently, significant efforts have been devoted to developing high-voltage, deep-charging cathodes[118-120]. Although charging cathode materials (e.g. NMC type, layered $Li_xNi_yMn_xCo_{1-y-z}O_2$) to higher voltage improves the cell capacity and initial energy density, a reduced cycling stability is commonly observed. For example, Zhu et al.[121] cycled single-crystal Li/NMC cells to different upper cutoff voltages and saw significant reduced cycle life for higher voltage cycling. Efforts to advance high-voltage cathodes can benefit from identifying degradation modes.

Researchers have used various experimental methods to characterize the degradation mechanisms of high-voltage cathodes. Lin et al.[122] used synchrotron XAS coupled with atomic-scale STEM-EELS to study the surface reconstruction of NMC layered cathode. Li et al.[123] tried to visualize the parasitic side-reaction product at the cathode-electrolyte interface using TOF-SIMS; Heenan et al.[124] adopted X-ray CT to keep track of the active material cracking; Quilty et al.[125] characterized the transition metal dissolution and shuttling to the anode through X-ray Fluorescence (XRF) Mapping and used SECM to map the lithium anode surface morphology. According to these efforts, the major sources of degradation of high-voltage cathode includes: active material cracking & detaching; non uniform growth of the cathode electrolyte interface and active material loss due to parasitic side reaction; irreversible surface reconstruction of NMC

layered material, lithium anode degradation due to transition metal dissolution from cathode side.[126, 127] These studies all provide important insights into degradation, yet it may often be difficult to correlate observations (degradation mechanisms) to electrochemical performance.

Recently, machine learning (ML) techniques have been applied to estimating the SOH (state of health)[128, 129] and RUL (remaining of useful life)[130, 131] of batteries. Although these techniques are proven efficient and accurate, a large training dataset is often required[132, 133]. Applications of models to identify degradation modes (i.e., why is SOH changing) have also been reported. The work by Birkl et al. [134] has described a methodology for identifying loss of active material in electrodes and loss of Li in the electrolyte. Their approach compares low-C-rate measurements with reversible potentials of the anode and cathode to effectively estimate loss in active material of the electrodes as well as loss of lithium from the electrolyte.

This chapter will introduce a methodology applied to higher C-rate data that allows for physical interpretation of changes in the electrode performance with cycle number based on a physics-based model that also incorporates transport processes. The approach allows for the estimation of transport and kinetic modes of degradations (such as apparent change in Li diffusion coefficient or growth of interfacial impedance). Such parameters have minimal impact at lower C-rates and are thus indeterminate from low C-rate cycling data.

Cathodes were designed with high porosity and low thickness to ensure electrode-scale transport processes were not important. Cycling experiments were conducted to ensure the investigation focuses on cathode degradation, with minimal impacts from anode degradation. The approach complements the aforementioned methods and has an advantage of exploiting cycling data while testing quantitatively hypotheses regarding the impact of degradation modes on

performance. Moreover, the model is used to identify degradation modes but also to assign the impact of each mode to changes in cell capacity, energy density, and power density.

5.2 Method

5.2.1 Experimental

System Design: The $Li/Li_xNi_{0.33}Mn_{0.33}Co_{0.33}O_2$($NMC_{111}$) cells are cycled at room temperature at two C-rates and two cutoff voltages. Using previous experimental and simulation studies [55, 99, 101], NMC electrodes were designed to avoid electrode-scale heterogeneity through the thickness of the electrode, which permits the isolation of agglomerate-scale transport effects, facilitating analysis. The thickness of the electrode was set to be low (~25 μm). Moreover, the areal active material loading is low (~ 0.7 mAh/cm^2), corresponding to an electrolyte porosity of ~0.6. At moderate cycling current rate (0.5 & 1.0 C), simulations show that electrode-scale heterogeneities are not anticipated. The low mass loading and low C-rate also results in low stripping/plating current density on the lithium metal anode, mitigating anode degradation, at least for early cycles. In some cases, the cycled lithium anode was replaced with a fresh Li metal, in an attempt to identify the range of cycles where performance degradation was dominated by the cathode. Using the early cycles of the system, the cell design enables a focus on the positive electrode degradation. Lastly, to minimize the effect of loss of lithium ion in the electrolyte, excess amount of electrolyte (~ 100 μL, which normalized by active material loading to ~100 g $(Ah)^{-1}$) is also added to cells.

Cycling Procedure: Cells were cycled under 4 conditions: 0.5C (1C = 150 mA g^{-1}) cycling between 2.8V and 4.3V, 0.5C cycling between 2.8V and 4.5V, 1.0C cycling between 2.8V and 4.3V, 1.0C cycling between 2.8V and 4.5V. We used CCCV (constant-current followed by

constant-voltage) charge and CC discharge to cycle the systems. For 1.0 C cycling, a slow rate (C/10) cycle was conducted after every ten 1C cycles. The C/10 cycle was followed by a GITT experiment. The details of GITT pulse experiments can be found in the Appendix. The C/10 cycle and GITT experiments were used to test conclusions drawn from model-characterized results, as discussed in the Results section.

5.2.2 Theory

Physics-based model: The physics-based continuum model used in this study follows the development by Doyle and Newman et al. [11], modified by a finite-volume numerical method that allows for a more general and conservative treatment of the multi-scale transport. A detailed description and validation of the NMC cathode model is given by Hui et al[55], and that model is used without modification to charge-transfer or thermodynamic parameters for cells with a 4.3V voltage cutoff. For analysis of cells cycled to a cutoff voltage of 4.5 V, the range of the published model was extended, and this required measurements of the thermodynamic open-circuit potential in the high potential range, measured by a GITT test on a Li/NMC coin cell, with low discharge current rate (C/10). The detailed open-circuit potential of cells charged to different voltages are included in Appendix.

Model Characterization of Cycling Data: The physics-based model (PBM) was applied to the cycling data to characterize the evolution of physical parameters. With the designed experimental system, three degradation modes were possible: active material loss (%AM), a change in agglomerate-scale lithium transport (D_{agg}), and a change in interfacial impedance

(R_{int}). The PBM was thus reformulated to determine these parameters as a function of cycle number by fitting the PBM to each discharge curve. Active material is modeled through determination of an apparent change in mass loading and active surface area from the initial value. Physically this might result from multiple mechanisms, such as loss of electronic connectivity of the agglomerate to the electrode. The change in agglomerate-scale transport was tracked by estimating changes in the agglomerate scale lithium effective diffusivity D_{agg} with cycle number. In the parameter estimation procedure, the characteristic time for solid lithium diffusion (L_{agg}^2/D_{agg}) is effectively determined. In the results reported here, we assume L_{agg} is fixed, thus using D_{agg} to represent the change in solid lithium diffusion. The apparent change in D_{agg} might be due to particle cracking (D_{agg} increase) for example. D_{agg} change might also be attributed to volume expansion of primary particles or interfacial layer growth from parasitic side reactions (D_{agg} decrease) that impacts diffusion through the agglomerate on primary particles. Change in interfacial impedance (R_{int}) was tracked by estimating the potential change at the solid/electrolyte interface ($\eta_{int} = i_{applied}R_{int}$), and is possibly due to growth of interfacial layer from side-reaction products. In the PBM model, the formulation to correlate change in interfacial impedance to change in cell voltage is:

$$V_{cell} = V_{cathode} + i_{applied}R_{int} - V_{anode} \qquad \text{Equation 5.1}$$

Where V_{cell} (V) is the measured cell potential, $V_{cathode}$(V) and V_{anode} (V) are the potentials of positive (NMC_{111}) and negative (Li metal) electrode and $i_{applied}$ ($A\ cm^{-2}$) is the applied current density (>0 for charge, <0 for discharge).

It was indicated by numerical simulations that 5000 sampling points using a Sobol Sequence[37] were sufficient to estimate the three parameters %AM, D_{agg}, and R_{int}. The sampling simulations

were fit to experimental discharge voltage profiles, and parameter confidence intervals were evaluated. [36, 135] The parameter estimation method was applied to all discharge curves, allowing the evaluation of parameters as a function of cycle number.

5.3 Results

5.3.1 Cycling Performance at 0.5C

To investigate the cycling performance of Li/NMC cells charged to different upper cutoff voltages, we cycled 6 coin-cells with constant current (0.5C), with three cells cycled between 2.8V and 4.3V and an additional three cells cycled between 2.8V and 4.5V.

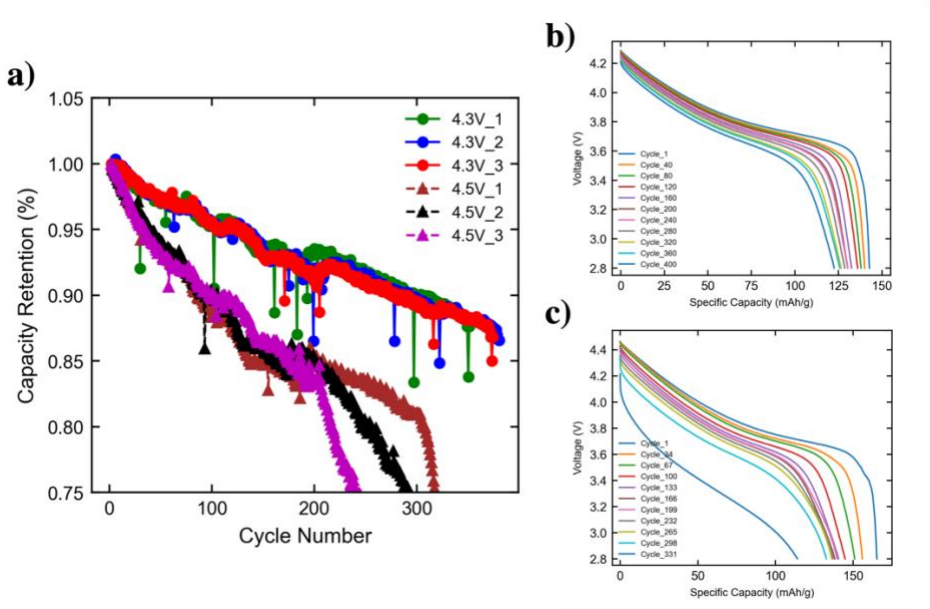

Figure 5.1 Experimental cycling performance for Li/NMC cells cycled at 0.5C (1C = 150 mA g^{-1}). (a) Discharge capacity retention vs. cycle number for cells cycled at 0.5C, charged to 4.3V or 4.5V. (b) Discharge voltage profiles for 4.3V_1 cell. (c) Discharge profiles for 4.5V_1 cell.

As shown in Figure 5.1a, three cells charged to 4.3V show reproducible cycling performance over the entire cycle life, which maintain ~90% discharge capacity after 300 cycles. Moreover, reproducible performance could also be observed for the cells charged to higher voltage (4.5V), for the first 200 cycles. Although these cells' discharge capacity starts to diverge after 200 cycles, they degrade more quickly. By replacing cycled lithium metal with fresh anode (Figure 5.8), followed by continued cycling of the cell, the discharge capacity recovers and the capacity evolution after replacing lithium follows the degradation trajectory observed at lower cycle number. This suggests that the accelerated degradation at late cycles corresponds to lithium metal electrode degradation, which is believed to be due to the dissolution and shuttling of transition metal from the NMC cathode side[136, 137]. To focus the study on degradation of the positive electrode, we only apply the model characterization to the first 200 cycles, before fast Li metal degradation.

Figure 5.1 shows an expected result at 0.5C that capacity fade is faster at the higher cutoff voltage. Figure 5.1b and c show the discharge voltage profiles for different cycles. The voltage profiles of both cells shift to lower capacity, with increased voltage losses. The profiles of cell cycled at 0.5C to 4.5V (Figure 5.1c) show a sudden shift down between 298 and 331 cycle, which is attributed to fast deterioration of the anode.

5.3.2 Identification of Degradation Mode

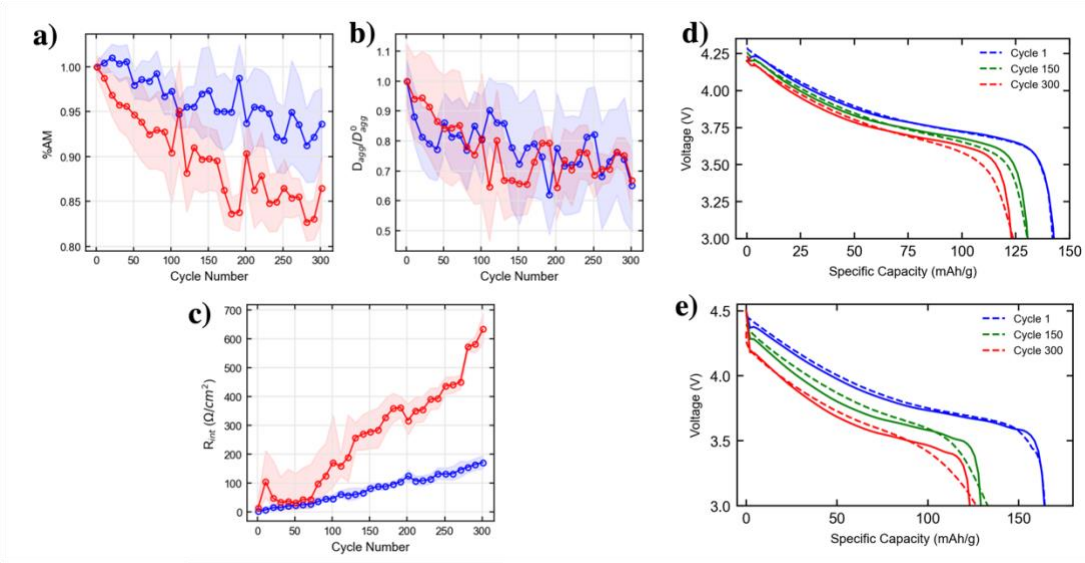

Figure 5.2 (a)-(c): Parameter estimations for cells charged to 4.3V (blue) and 4.5V(green) at a cycling rate of 0.5C. Open dots are the most probable parameter values. The shaded regions indicate the confidence intervals of the parameter estimation. (d): Simulation results (solid) using most probable parameter values in (a), (b) and (c) are compared to experiment (dashed) for three cycles of cell charged to 4.3V. (e): Simulation results (solid) and experiments (dashed) of cell charged to 4.5V.

The evolution of model-estimated parameter values with cycle number is shown in Figure 5.2a, b and c. The shaded contours illustrate the confidence intervals of the parameter estimates (assuming a constant experimental variation of 20mV). Figure 5.2d compares the experimentally observed voltage profiles with model simulations for select cycle numbers. The results for cells charged to 4.3V show an ~10% active material loss after 300 cycles (Figure 5.2a). Furthermore, the cells appear to show also an ~40% reduction in agglomerate-scale Li diffusion coefficient (Figure 5.2b) and a 200 $\Omega\ cm^2$ growth in interfacial impedance (Figure 5.2c).

When cells were cycled to 4.5V, results show more active material loss (~18%) and a similar degree of D_{agg} reduction (~40%) after 300 cycles. In contrast, the increase in interfacial

impedance (~ 600 $\Omega\ cm^2$) is significantly larger, with the rate of change per cycle increasing with cycle number. As the cells are charged to high voltage, more Li^+ is removed from the NMC active materials, leading to increased volume change and residual stress, which could potentially result in active particle cracking or detaching from the conductive matrix. Moreover, the elevated voltage may result in increased electrolyte side reactions at the cathode/electrolyte interface. The electrolyte breakdown products could form passivation layers, which may increase interfacial electronic resistance and also passivate the active particle from reaction, thus causing active material loss.

5.3.3 Cycling Performances at 1.0C:

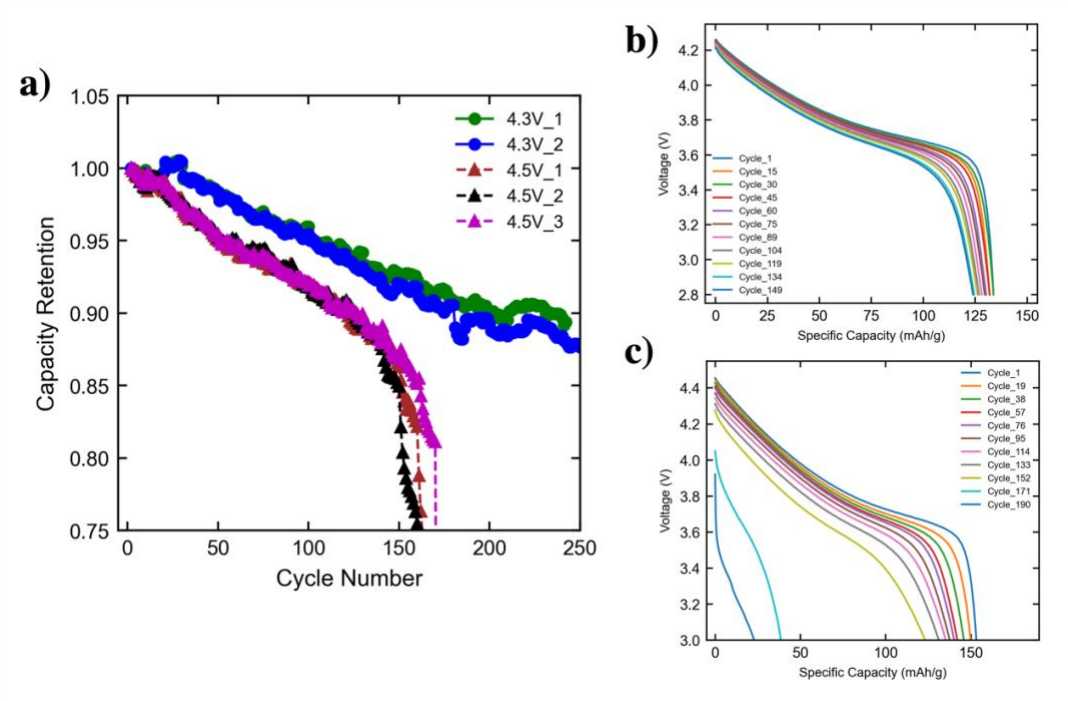

Figure 5.3 Experimental cycling performance for Li/NMC cells cycled at 1.0C. (a) Discharge capacity retention vs. cycle number for cells charged to 4.3V and 4.5V. (b) Discharge voltage profiles for 4.3V_1 cell. (c) Discharge profiles for 4.5V_1 cell.

As Figure 5.3a shows, when same type of cells are cycled at 1.0C, cells charged to 4.3V and 4.5V also show reproducible cycling performances. At a cutoff voltage of 4.3V, cells maintained ~90% initial capacity after 250 cycles, while the cells charged to 4.5V show faster capacity fading, with ~87% capacity retention after 150 cycles. As observed when cycled at 0.5C, the cells cycled at 1C also experience a sudden capacity drop after 150 cycles, corresponding to fast lithium metal degradation. Figure 5.3b and 5.3c show discharge voltage profiles of individual cycles. Interestingly, during the first 150 cycles, cells cycled at 1C to 4.5V have higher capacity retention compared with cells cycled at 0.5 C to 4.5V (Figure 5.1a), which is 87% vs. 84%.

5.3.4 Degradation Mode Characterization at 1.0C:

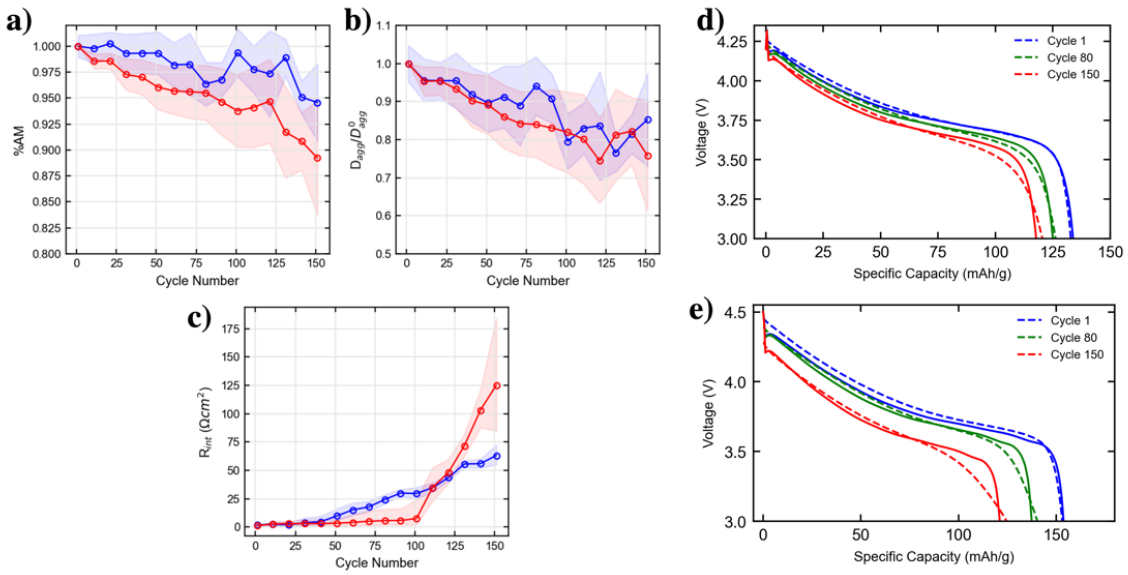

Figure 5.4 (a)-(c): Parameter estimates for cells charged to 4.3V (blue) and 4.5V(green) at a cycling rate of 1.0 C. Open dots are the most probable parameter values. The shaded regions indicate the confidence intervals of the parameter estimation. (d): Simulation results (solid) using most probable parameter values in (a), (b) and (c) are compared to experiment (dashed) for three cycles of cell charged to 4.3V. (e): Simulation results (solid) and experiments (dashed) of cell charged to 4.5V.

Parameter estimates for 1C cycling are shown in Figure 5.4. Figure 5.4d and 5.4e demonstrate that the model agrees well with experimental discharge profiles at all cycle numbers. In Figure 5.4a, it is seen that the cells cycled to 4.5V experience 11% active material loss after 150 cycles, compared to 5% active material loss when cycled to 4.3V. Nevertheless, the AM loss at 1C is generally less than when cycled at 0.5C when charged to 4.5V. According to Figure 5.4c, the interfacial impedance growth of cells cycled to 4.5V are initially close to cells cycled to 4.3V, at least for the first 100 cycles. After 100 cycles, the interfacial impedance grows quickly. Similar to the cells cycled at 0.5C, Figure 5.4b shows no obvious change in the variation of D_{agg} with cycle number with cells cycling at 1.0C and charged to different upper cutoff voltage.

5.3.5 Validation of Parameter Estimations

Previous work[133, 134] indicates that the loss of active material can be well estimated from low C-rate measurements. Furthermore, the changes in the interfacial resistance can be determined by investigating rapid voltage changes when the current is pulsed. These additional measurements were taken as a means of validating parameter estimates.

As reported by previous study and validated by our own simulation, low current cycling leads to minimum ion transport, electron transport, and charge transfer overpotential. Thus, only the active material percentage (%AM) significantly impacts the measured capacity. Accordingly, one C/10 charge/discharge cycle was added after every ten cycles of 1.0 C tests to monitor the active material loss. The C/10 provides a direct estimate of %AM vs. cycle number for comparison with parameter estimates from 1.0C cycling. As shown in Figure 5.5a, for cells charge to 4.3V and

4.5V, the model-characterized %AM agrees well with C/10 measurement, and this helps to confirm that the PBM can estimate %AM by simply fitting to constant current voltage profiles.

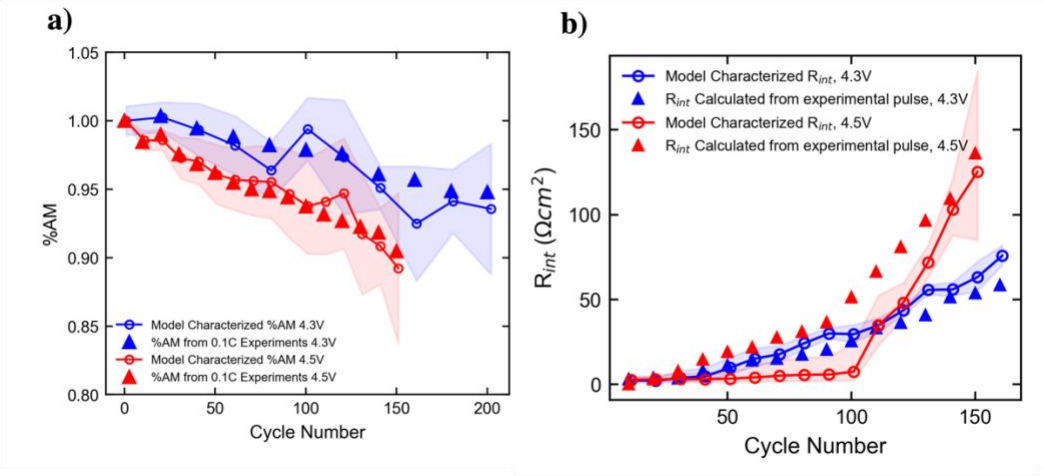

Figure 5.5 (a): Parameter estimates from cycling of AM loss (open dots with shades) and 0.1C measured results (triangles) for cells cycled at 1.0 C and charged to 4.3V (blue) and 4.5V (red). (b): Parameter estimates of interfacial impedance growth (open dots with shades) compared to estimates from pulse experiment for cells cycled at 1.0C and charged to 4.3V(blue) and 4.5V (red). For 4.3V group, $i_{applied} = 0.77\ mA\ cm^{-2}$; For 4.5V group, $i_{applied} = 0.7\ mA\ cm^{-2}$.

Moreover, a previous study[55] showed that a current interrupt experiments can distinguish between interfacial and mass transport overpotentials. To measure the increased cell interfacial impedance during cycling, we designed discharge-rest (GITT) pulse experiments after every ten cycles of 1.0C. The instantaneous voltage jumps between current on and current off can be expressed by:

$$\eta_0 = \eta_{ct} + \eta_{int} \qquad \text{Equation 5.2}$$

Where η_0 is the instantaneous voltage jump (V), η_{ct} is the cell's initial charge transfer overpotential (V) and η_{int} is the interfacial electronic overpotential (V, includes increased charge-transfer and electron-transport overpotential) due to growth of interfacial impedance. Under constant current charge/discharge, the interfacial impedance R_{int} ($\Omega\ cm^2$) can be expressed by:

$$R_{int} = \frac{\eta_{int}}{i_{applied}} \qquad \text{Equation 5.3}$$

Combining Equation 5.2 and 5.3, the increased interfacial impedance during cycling compared to cycle 1 (ΔR_{int}) can be calculated from:

$$\Delta R_{int} = \frac{\Delta \eta_0}{i_{applied}} \qquad \text{Equation 5.4}$$

In the 1.0C cycling studies, pulse experiments were introduced after every ten cycles, as a means of independently measuring ΔR_{int}. Figure 5.5b shows comparison between the pulse-measured R_{int} ($\Delta R_{int} = R_{int}$ given the model estimated R_{int} at Cycle 1 is negligible according to Figure 5.4c) and results obtains by fitting the PBM to discharge date. Similar trends are observed, suggesting that the PBM estimates provide an effective means of quantifying interfacial impedance growth.

The study above supports the parameter estimation results by adding low-rate cycling and pulse experiments in between normal cycles. Alternatively, if no model is applicable for use in degradation analysis, a cycling protocol that interjects an intermittent low C-rate cycle, followed by a GITT analysis, may be effective. If the number of degradation modes to be tested is large, such protocols, can also be used to reduce the dimensionality of the parameter space that is used to fit the physics-based models to cycling data.

5.4 Discussion

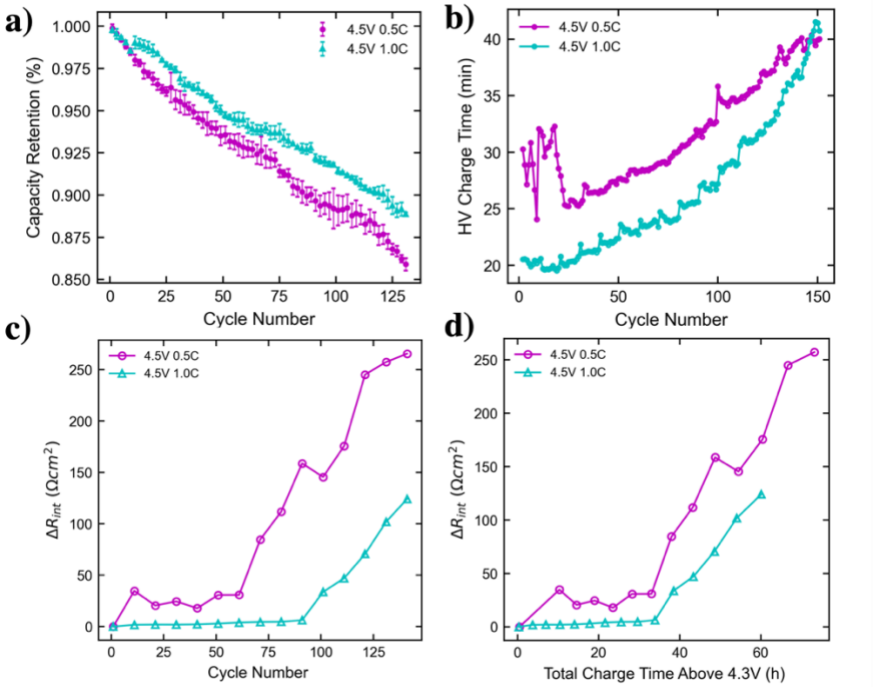

Figure 5.6 (a): Capacity retentions for cells charged to 4.5V, cycled at 0.5C & 1.0C. Error bar indicates the experimental variations among parallel cells. (b): The time spent during charge above 4.3V for cell cycled at 0.5C and cell cycled at 1.0C. (c): Interfacial impedance growth for cell cycled charged to 4.5V, cycled at 0.5C or 1.0C. (d): Interfacial impedance growth plotted as a function of total charge time the cell spent above 4.3V.

Figure 5.6a compares the cycling performance of cells cycled at 0.5C and 1.0C, charged to 4.5V. The 0.5C cycling shows faster degradation compared to 1C cycling. According to Figure 5.2 and Figure 5.4, the model also estimates increased active material loss and increased impedance growth for cell cycled at 0.5C. Possibly, the higher degradation rate at 0.5C is because the cells spend more time per cycle above high voltage (>4.3 V) than they do at 1C, and this is shown by Figure 5.6b. We hypothesize that the longer high-voltage time results in more electrolyte breakdown at cathode-electrolyte interface, and this reduces active material percentage and increases the interfacial impedance. Figures 5.6c and 5.6d show the model-estimated interfacial

impedance growth as a function of cycle number and total time cell spent at high voltage. In Figure 5.6d, it is seen that ΔR_{int}, for both cycling rates, begins to increase significantly after ~30-40 h, regardless of cycling rate.

The results above focus on identifying the parameters that correlate with measured variations in performance with cycle number. However, that is not the same as quantifying the impact of the parameters on capacity fade, for example. The PBM can be used as a means of determining the importance of each mode by evaluating the degree by which capacity is loss by. In short, the performance metric is quantified by sequentially adding fading of R_{int}, AM%, and then D_{agg}. The percent contribution of each degradation mode to the performance loss is quantified as a function of cycle number.

In theory, the relative impact of each parameter on performance loss depends on cycle number. We however did not find significant variations over cycle number, and thus report averages over the life of the cells. Figure 5.7 indicates that loss of active material and the decline in Li mobility both contribute to capacity fade, with loss in mobility more important at higher C-rates. Figures 5.7b and d, which summarizes results obtained at a higher cutoff voltage, shows a similar trend, with loss of active material being a more substantial contributor to capacity fade. Similar qualitative observations are seen for the loss in energy density. For loss in cell average discharge power, it is mostly dominated by interfacial impedance growth, regardless of the cycling conditions.

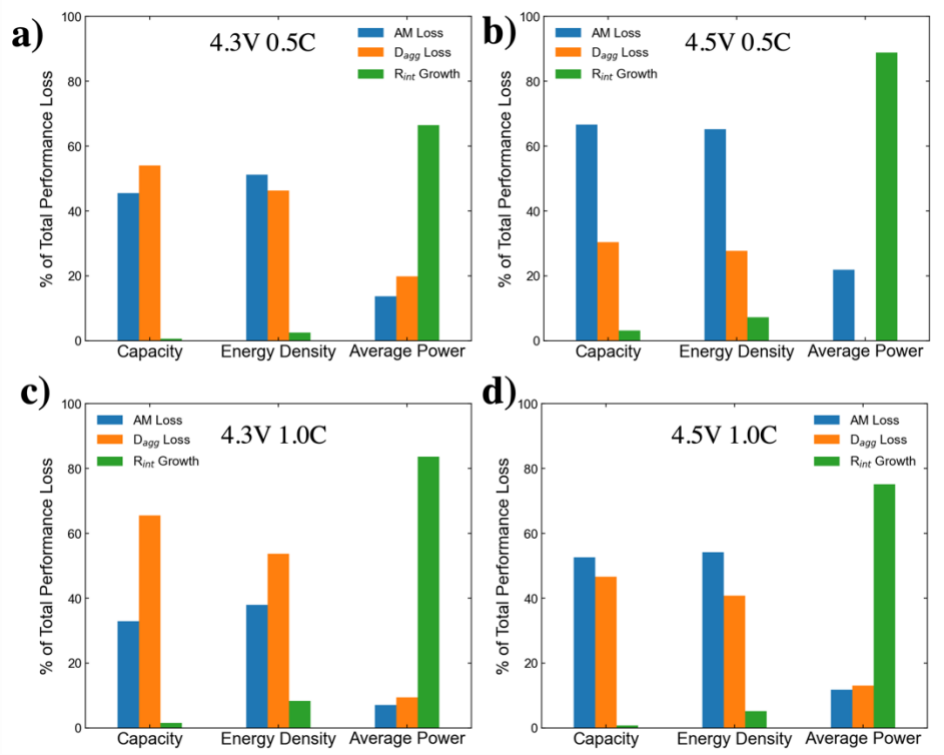

Figure 5.7 Contribution of individual parameters (AM loss, D_{agg} reduction and R_{int} growth) to reduction of discharge capacity (mAh g^{-1}), energy density (Wh kg^{-1}) and average power (W kg^{-1})). The fractional contributions are averaged over the whole cycle life of the cell. The equations for calculating cell energy and power density are listed in Appendix.

5.5 Conclusion

Physics-based models fit to cycling data provides a viable means of characterizing degradation modes of cells. This approach has several advantages, including facile, readily available experimental data and a means of quantifying impact on performance. Parameter estimation indicates, that when a Li/NMC cell is charged to 4.5V (instead of 4.3V), faster active material loss and interfacial impedance growth are observed. There is also an observed decline under all conditions in Li-ion mobility. This decline is largely independent of cutoff voltage. Loss of active material and reduction of Li-ion mobility are significant contributors to capacity fade and

a loss in energy density. The fading in power density is dominated by growth in interfacial impedance

5.6 List of Symbols

%AM	% active material (NMC_{111}) left compared with fresh electrode
D_{agg}	Diffusion coefficient of lithium ions in agglomerates [$cm^2\ s^{-1}$].
η_{ct}	Charge transfer overpotential [V]
η_{int}	Interfacial electronic overpotential [V]
η_0	Instantaneous voltage jump between current on and current off [V]
R_{int}	Interfacial impedance [$\Omega\ cm^2$]
$i_{applied}$	Applied current density [A cm^{-2}]
L_{agg}	Agglomerate size [μm]
V_{athode}	Cell anode potential [V]
$V_{cathode}$	Cell cathode potential [V]
V_{cell}	Cell Voltage [V]

5.7 Supplementary Information

5.7.1 Details of PBM Model

In our study, the Li/NMC_{111} model adopted the formulation listed in Chapter 2. Electrode-scale equations were coupled with agglomerate-scale equations. For the cells charged to 4.5V, the

OCP function is obtained from GITT measurement at C/10. The polynomial-fitted OCP function is:

Table 5.1 Governing equations and boundary conditions for mathematical model of NMC cell.

Reversible Potential for NMC_{111} for Cells Charged to 4.5V

(12) $U = U_{ref} + \frac{RT}{F}\ln\left[\left(\frac{c}{c_0}\right)\left(\frac{1-\bar{c}_{max}}{\bar{c}_{max}}\right)\right] + \sum_{k=0}^{14} A_k[(2\bar{c}_{max}-1)^{k+1} - \frac{2\bar{c}_{max}k(1-\bar{c}_{max})}{(2\bar{c}_{max}-1)^{1-k}}]$ $\bar{c}_{max} = \frac{c_s - c_{s,0}}{c_{s,max} - c_{s,0}}$

Parameter	Value	Parameter	Value	Parameter	Value
$c_{s,max}(mol\ cm^{-3})$	0.0286	A_4	-0.344876	A_{10}	3.518708
$U_{ref}(V)$	3.897918	A_5	-1.092397	A_{11}	17.52025
A_0	-0.343458	A_6	1.910821	A_{12}	1.275711
A_1	0.141308	A_7	5.967700	A_{13}	-7.821986
A_2	-0.042377	A_8	-4.481530	A_{14}	-2.196664
A_3	0.000829	A_9	-15.02123		

5.7.2 Replacing Cycled Li Metal Anode

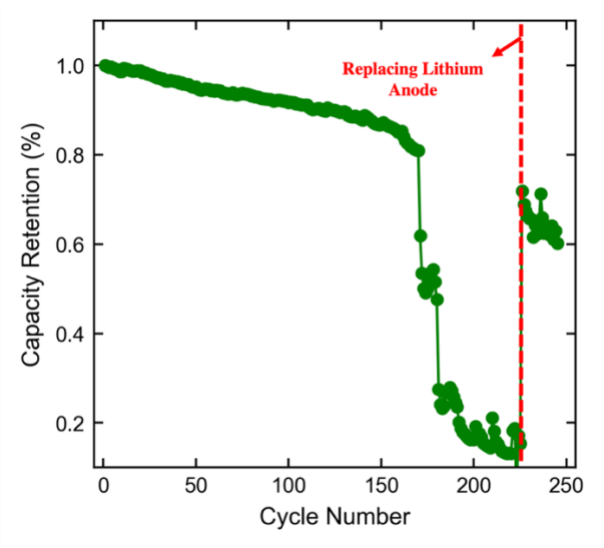

Figure 5.8 Cycling performance of Li/NMC_{111} cell, cycled at 1.0C, charged to 4.5V (4.5_3 in Figure 5.3). Red vertical line shows the cycle number at which the cycled lithium metal is replaced with a fresh one.

As Figure 5.8 shows, by replacing cycled lithium metal with a fresh anode, the cell discharge capacity recovers, and the capacity evolution after replacing lithium follows the degradation trajectory observed at lower cycle number (<150 cycles).

5.7.3 GITT Experiments

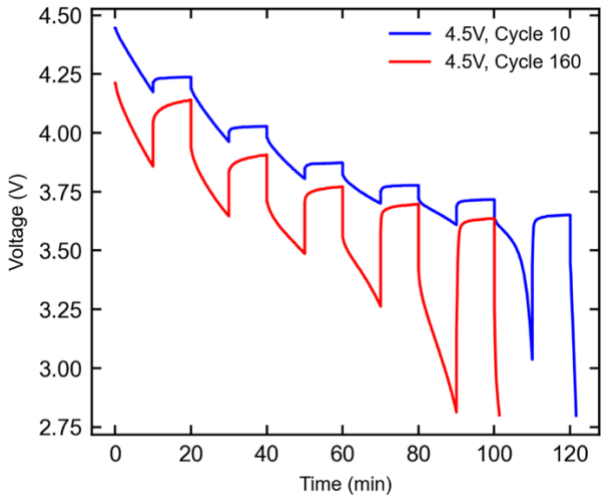

Figure 5.9 GITT pulse experiments after every 10 cycles of 1.0C constant-current cycling. Cell is charged to 4.5V.

Figure 5.9 shows the voltage profiles of the GITT pulse experiments. During constant current discharge, the current is interrupted to let the cell voltage to recover to OCP at different state-of-(dis)charge. The voltage recovery contains an instantaneous portion and a time-dependent portion, as shown above. The instantaneous voltage recovery (η_0) is related to electronic overpotentials and can be used to characterize the interfacial impedance growth. Comparing the GITT profiles after 10th and 160th cycle, a clear increase in η_0 is observed.

5.7.4 Calculation of Cell Performance Metrics

Cell energy density (E_M, Wh kg^{-1}):

$$E_M = \frac{\int_0^{t_{max}} V_{cell}(t) i_{applied} A dt}{Cell\ Total\ Mass} \qquad \text{Equation 5.5}$$

Cell Average power ($\overline{P_{Cell}}$, W):

$$\overline{P_{Cell}} = \frac{\int_0^{t_{max}} V_{cell}(t) i_{applied} A dt}{t_{max} * Cell\ Total\ Mass} \qquad \text{Equation 5.6}$$

Where V_{cell} is the cell voltage (V), $i_{applied}$ is applied current density (A cm^{-2}), A is the electrode area (cm^2), t_{max} is the total discharge time for each cycle. Cell Total Mass indicates the total mass of all components inside the cell:

$$Cell\ Total\ Mass = m_{cathode} + m_{anode} + m_{separator} + m_{current\ collector} \quad \text{Equation 5.7}$$

Here we use Li metal foil (thickness=200μm) as anode, 16μm thick Al foil as cathode current collector and Celgard 2325 separator (25μm thick, porosity=0.39).

Chapter 6: Conclusion

In this dissertation, I've shown how we use the physics-based continuum model to help guide the optimization of electrode design and interpret cell degradation, in an attempt to understand the underlying physics of the LIBs systems and push the state-of-the-art lithium-ion-battery towards superior energy density and cycle life.

Chapter 2 shows the process of model selection, which not only enables the determination of the critical length scale for lithium transport in the NMC_{111} electrode, but also provides an experimentally validated model (Li/Agglomerate NMC_{111} model) for later studies. Chapter 3 studies the optimization of slurry-casted electrode design. We found that the optimization of electrode-scale lithium transport in different material systems follows a general trend. With material-specific information provided, such 'General Design Rule' could dramatically reduce the workload in practical electrode design optimization. Chapter 4 uses the physics-based model to analyze the ion transport phenomena in aligned-channel architecture, a 'hot topic' in recent study on thick electrode fabrication. We hope the relation we found between electrode architecture and ion-transport rate could help further optimization of aligned-channel design. Finally, I use Chapter 5 to show another application of the model: degradation analysis. The highlight in this chapter is that we compare the model-characterized degradation modes with experimentally measured results and get good agreement. This not only confirms the accuracy of the model-characterization approach, but also makes the point that some simple 'in-situ' galvanostatic/galvanostatic-interruptive experiments could effectively keep track of the change of physics during cell cycling.

Finally, here are some extra remarks that I hope the readers could keep in mind:

1. During my study, I realized that the electrode tortuosity (τ) is a key parameter in thick electrode design and optimization. Nevertheless, the relation between electrode architecture (e.g., porosity) and tortuosity has not been fully understood. Further investigation in electrode tortuosity understanding/characterization is crucial to commercialization of thick electrode.
2. Although I've shown that the mathematical model is an efficient means to understand the physics of battery system and guide the optimization, the full potential has not been leveraged yet. For example, machine learning method could be applied to the physics-based model, which is able to accelerate the parameter estimation process and could also take account for the imperfectness of the model.
3. To ensure accuracy of mathematical model in solving real problems, well-designed simple experiment is preferred as training set or validation set for the model.

List of Author's Publications as a Result of Thesis

Chapter 2:

Z. Hui, K. S. Mayilvahanan, Y. Yang, and A. C. West, *Journal of The Electrochemical Society,* **167** (10), 100542 (2020).

Chapter 3:

Z. Hui, K. S. Mayilvahanan, K. Ganko, Y. Yang, X. Zhang, Z. Ju, K. J. Takeuchi, A. C. Marschilok, G. Yu, E. Takeuchi, and A. C. West, Energy Storage Materials, 39 176 (2021).

Chapter 4:

Z. Hui, X. Zhang, K. S. Mayilvahanan, Z. Ju, K. J. Takeuchi, A. C. Marschilok, E. S. Takeuchi, G. Yu, and A. C. West, Journal of The Electrochemical Society, 168 (10), 100536 (2021).

Chapter 5:

Z. Hui, K. Mayilvahanan, A. Li, T. Jin, M. Preindl, Y. Yang, K. J. Takeuchi, A. C. Marschilok, E. Takeuchi, A. C. West. Electrochemical Characterization of Degradation Modes of High-Voltage NMC Electrodes. *In Preparation.*

Bibliography

1. B. Scrosati, *J Solid State Electr,* **15** (7), 1623 (2011).
2. T. Placke, R. Kloepsch, S. Dühnen, and M. Winter, *J Solid State Electr,* **21** (7), 1939 (2017).
3. K. Brandt, *Solid State Ionics,* **69** (3), 173 (1994).
4. M. S. Whittingham, *Science,* **192** (4244), 1126 (1976).
5. K. Mizushima, P. C. Jones, P. J. Wiseman, and J. B. Goodenough, *Materials Research Bulletin,* **15** (6), 783 (1980).
6. K. S. Akira Yoshino, Takayuki Nakajima, Vol. 4668595, Unite States, 1987.
7. T. Nagaura, *Progress in Batteries & Battery Materials,* **10** (1991).
8. Y. Zhou, M. Wang, H. Hao, L. Johnson, H. Wang, and H. Hao, *Mitigation and Adaptation Strategies for Global Change,* **20** (5), 777 (2015).
9. A. Manthiram, A. Vadivel Murugan, A. Sarkar, and T. Muraliganth, *Energy & Environmental Science,* **1** (6), 621 (2008).
10. X.-B. Cheng, R. Zhang, C.-Z. Zhao, and Q. Zhang, *Chemical Reviews,* **117** (15), 10403 (2017).
11. M. Doyle, T. F. Fuller, and J. Newman, *Journal of the Electrochemical society,* **140** (6), 1526 (1993).
12. T. F. Fuller, M. Doyle, and J. Newman, *Journal of The Electrochemical Society,* **141** (1), 1 (1994).
13. M. S. Whittingham, *Chemical Reviews,* **114** (23), 11414 (2014).
14. G. E. Blomgren, *Journal of The Electrochemical Society,* **164** (1), A5019 (2017).
15. V. Etacheri, R. Marom, R. Elazari, G. Salitra, and D. Aurbach, *Energy & Environmental*

Science, **4** (9), 3243 (2011).

16. L. Lu, X. Han, J. Li, J. Hua, and M. Ouyang, *Journal of power sources,* **226** 272 (2013).
17. J. Liu, Z. Bao, Y. Cui, E. J. Dufek, J. B. Goodenough, P. Khalifah, Q. Li, B. Y. Liaw, P. Liu, and A. Manthiram, *Nature Energy,* 1 (2019).
18. S. Chen, C. Niu, H. Lee, Q. Li, L. Yu, W. Xu, J.-G. Zhang, E. J. Dufek, M. S. Whittingham, and S. Meng, *Joule,* **3** (4), 1094 (2019).
19. R. Marom, S. F. Amalraj, N. Leifer, D. Jacob, and D. Aurbach, *Journal of Materials Chemistry,* **21** (27), 9938 (2011).
20. M. Singh, J. Kaiser, and H. Hahn, *Journal of The Electrochemical Society,* **162** (7), A1196 (2015).
21. M. Hu, X. Pang, and Z. Zhou, *Journal of Power Sources,* **237** 229 (2013).
22. M. D. Radin, S. Hy, M. Sina, C. Fang, H. Liu, J. Vinckeviciute, M. Zhang, M. S. Whittingham, Y. S. Meng, and A. Van der Ven, *Advanced Energy Materials,* **7** (20), 1602888 (2017).
23. L. O. Valøen and J. N. Reimers, *Journal of The Electrochemical Society,* **152** (5), A882 (2005).
24. E. Antolini, *Solid State Ionics,* **170** (3-4), 159 (2004).
25. C. Julien, *Materials Science and Engineering: R: Reports,* **40** (2), 47 (2003).
26. V. Srinivasan and J. Newman, *Journal of the Electrochemical Society,* **151** (10), A1517 (2004).
27. N. W. Brady, Q. Zhang, K. Knehr, P. Liu, A. C. Marschilok, K. J. Takeuchi, E. S. Takeuchi, and A. C. West, *Journal of The Electrochemical Society,* **163** (14), A2890 (2016).
28. N. Yabuuchi and T. Ohzuku, *Journal of Power Sources,* **119** 171 (2003).

29. X. Y. Zhang, W. J. Jiang, A. Mauger, Qilu, F. Gendron, and C. M. Julien, *Journal of Power Sources,* **195** (5), 1292 (2010).

30. P. F. Yang, J. M. Zheng, S. Kuppan, Q. Y. Li, D. P. Lv, J. Xiao, G. Y. Chen, J. G. Zhang, and C. M. Wang, *Chem Mater,* **27** (21), 7447 (2015).

31. W. Weppner and R. A. Huggins, *Journal of The Electrochemical Society,* **124** (10), 1569 (1977).

32. K. W. Knehr, N. W. Brady, C. A. Cama, D. C. Bock, Z. Lin, C. N. Lininger, A. C. Marschilok, K. J. Takeuchi, E. S. Takeuchi, and A. C. West, *Journal of the Electrochemical Society,* **162** (14), A2817 (2015).

33. N. W. Brady, Q. Zhang, A. Bruck, D. C. Bock, C. A. Gould, A. C. Marschilok, K. Takeuchi, E. Takeuchi, and A. C. West, *Journal of The Electrochemical Society,* **165** (2), A371 (2018).

34. B. Paxton, *Journal of The Electrochemical Society,* **144** (11), 3818 (1997).

35. J. Newman and E. Thomas-Alyea. John Wiley & Sons: New York, 2004.

36. N. W. Brady, C. A. Gould, and A. C. West, *Journal of The Electrochemical Society,* **167** (1), 013501 (2020).

37. H. Niederreiter, *Journal of number theory,* **30** (1), 51 (1988).

38. W. K. Hastings, (1970).

39. R. Amin and M. Chiang, *Journal of the Electrochemical Society,* **163** (8), A1512 (2016).

40. Z.-D. Huang, X.-M. Liu, S.-W. Oh, B. Zhang, P.-C. Ma, and J.-K. Kim, *Journal of Materials Chemistry,* **21** (29), 10777 (2011).

41. A. M. Molinaro, R. Simon, and R. M. Pfeiffer, *Bioinformatics,* **21** (15), 3301 (2005).

42. R. Amin and Y. M. Chiang, *Journal of the Electrochemical Society,* **163** (10), X7 (2016).

43. S. Cui, Y. Wei, T. Liu, W. Deng, Z. Hu, Y. Su, H. Li, M. Li, H. Guo, and Y. Duan, *Advanced*

Energy Materials, **6** (4), 1501309 (2016).

44. W. Weppner and R. A. Huggins, *Journal of the Electrochemical Society,* **124** (3), C135 (1977).

45. J. P. Barton and D. G. Infield, *IEEE Transactions on Energy Conversion,* **19** (2), 441 (2004).

46. K. C. Divya and J. Østergaard, *Electric Power Systems Research,* **79** (4), 511 (2009).

47. I. Hadjipaschalis, A. Poullikkas, and V. Efthimiou, *Renewable and Sustainable Energy Reviews,* **13** (6), 1513 (2009).

48. J. M. Tarascon and M. Armand, in *Materials for Sustainable Energy*, p. 171, Co-Published with Macmillan Publishers Ltd, UK, (2010).

49. https://www.energy.gov/sites/prod/files/2016/06/f32/es000_howell_2016_o_web.pdf.

50. G. Berckmans, M. Messagie, J. Smekens, N. Omar, L. Vanhaverbeke, and J. Van Mierlo, *Energies,* **10** (9), (2017).

51. A. Manthiram, X. Yu, and S. Wang, *Nature Reviews Materials,* **2** (4), 16103 (2017).

52. L. O. Valøen and J. N. Reimers, *Journal of The Electrochemical Society,* **152** (5), A882 (2005).

53. C. Yu, S. Ganapathy, E. R. H. v. Eck, H. Wang, S. Basak, Z. Li, and M. Wagemaker, *Nature Communications,* **8** (1), 1086 (2017).

54. M. D. Radin, S. Hy, M. Sina, C. Fang, H. Liu, J. Vinckeviciute, M. Zhang, M. S. Whittingham, Y. S. Meng, and A. Van der Ven, *Advanced Energy Materials,* **7** (20), 1602888 (2017).

55. Z. Hui, K. S. Mayilvahanan, Y. Yang, and A. C. West, *Journal of The Electrochemical Society,* **167** (10), 100542 (2020).

56. H. Zhang, X. Yu, and P. V. Braun, *Nature Nanotechnology,* **6** (5), 277 (2011).

57. N. Li, Z. Chen, W. Ren, F. Li, and H.-M. Cheng, *Proceedings of the National Academy of Sciences,* **109** (43), 17360 (2012).

58. J. Newman, *Journal of The Electrochemical Society,* **142** (1), 97 (1995).

59. W. A. Appiah, J. Park, S. Song, S. Byun, M.-H. Ryou, and Y. M. Lee, *Journal of Power Sources,* **319** 147 (2016).

60. S. De, P. W. C. Northrop, V. Ramadesigan, and V. R. Subramanian, *Journal of Power Sources,* **227** 161 (2013).

61. https://cuit.columbia.edu/shared-research-computing-facility.

62. B. Paxton and J. Newman, *Journal of The Electrochemical Society,* **144** (11), 3818 (1997).

63. Y. Kuang, C. Chen, D. Kirsch, and L. Hu, *Advanced Energy Materials,* **9** (33), 1901457 (2019).

64. K. Mayilvahanan, N. Brady, A. H. McCarthy, L. Wang, A. C. Marschilok, K. Takeuchi, E. Takeuchi, and A. C. West, *Journal of The Electrochemical Society,* **167** (10), 100503 (2020).

65. Z. Ju, X. Zhang, S. T. King, C. D. Quilty, Y. Zhu, K. J. Takeuchi, E. S. Takeuchi, D. C. Bock, L. Wang, A. C. Marschilok, and G. Yu, *Applied Physics Reviews,* **7** (4), 041405 (2020).

66. G. Cunningham, M. Lotya, N. McEvoy, G. S. Duesberg, P. van der Schoot, and J. N. Coleman, *Nanoscale,* **4** (20), 6260 (2012).

67. R. Morasch, J. Landesfeind, B. Suthar, and H. A. Gasteiger, *Journal of The Electrochemical Society,* **165** (14), A3459 (2018).

68. D. A. G. Bruggeman, *Annalen der Physik,* **416** (7), 636 (1935).

69. J. Landesfeind, J. Hattendorff, A. Ehrl, W. A. Wall, and H. A. Gasteiger, *Journal of The Electrochemical Society,* **163** (7), A1373 (2016).

70. N. W. Brady, Q. Zhang, K. W. Knehr, P. Liu, A. C. Marschilok, K. J. Takeuchi, E. S. Takeuchi, and A. C. West, *Journal of The Electrochemical Society,* **163** (14), A2890 (2016).

71. X. Zhang, Z. Ju, L. M. Housel, L. Wang, Y. Zhu, G. Singh, N. Sadique, K. J. Takeuchi, E. S. Takeuchi, A. C. Marschilok, and G. Yu, *Nano Letters,* **19** (11), 8255 (2019).

72. Z. Ju, Y. Zhu, X. Zhang, D. M. Lutz, Z. Fang, K. J. Takeuchi, E. S. Takeuchi, A. C. Marschilok, and G. Yu, *Chem Mater,* **32** (4), 1684 (2020).

73. F. Wang and M. Tang, *Cell Reports Physical Science,* **1** (9), 100192 (2020).

74. H. Zheng, J. Li, X. Song, G. Liu, and V. S. Battaglia, *Electrochimica Acta,* **71** 258 (2012).

75. Z. J. Du, D. Wood, C. Daniel, S. Kalnaus, and J. L. Li, *J Appl Electrochem,* **47** (3), 405 (2017).

76. N. W. Brady, C. A. Gould, and A. C. West, *Journal of The Electrochemical Society,* **167** (1), 013501 (2019).

77. Y. Yang, S. Bremner, C. Menictas, and M. Kay, *Renewable and Sustainable Energy Reviews,* **91** 109 (2018).

78. A. Yoshino, *Angewandte Chemie International Edition,* **51** (24), 5798 (2012).

79. Y. Liang, C.-Z. Zhao, H. Yuan, Y. Chen, W. Zhang, J.-Q. Huang, D. Yu, Y. Liu, M.-M. Titirici, Y.-L. Chueh, H. Yu, and Q. Zhang, *InfoMat,* **1** (1), 6 (2019).

80. M. Yoshio, R. J. Brodd, and A. Kozawa, *Lithium-ion batteries : science and technologies*, p. xxvi, Springer, New York (2009).

81. P. Van den Bossche, F. Vergels, J. Van Mierlo, J. Matheys, and W. Van Autenboer, *Journal of Power Sources,* **162** (2), 913 (2006).

82. K. Young, C. Wang, L. Y. Wang, and K. Strunz, in *Electric Vehicle Integration into Modern Power Networks*, R. Garcia-Valle and J. A. Peças Lopes, eds., p. 15, Springer New York,

New York, NY, (2013).

83. W. Sierzchula, S. Bakker, K. Maat, and B. van Wee, *Energy Policy,* **68** 183 (2014).

84. L. T. Lam and R. Louey, *Journal of Power Sources,* **158** (2), 1140 (2006).

85. M. Faraj and O. Basir, *in* "2016 IEEE Transportation Electrification Conference and Expo (ITEC)", p. 1, 2016.

86. https://www.bloomberg.com/news/articles/2020-12-16/electric-cars-are-about-to-be-as-cheap-as-gas-powered-models.

87. K. Märker, P. J. Reeves, C. Xu, K. J. Griffith, and C. P. Grey, *Chem Mater,* **31** (7), 2545 (2019).

88. M. Wild, L. O'Neill, T. Zhang, R. Purkayastha, G. Minton, M. Marinescu, and G. J. Offer, *Energy & Environmental Science,* **8** (12), 3477 (2015).

89. M. A. Rahman, X. Wang, and C. Wen, *Journal of The Electrochemical Society,* **160** (10), A1759 (2013).

90. J. Wu, X. Zhang, Z. Ju, L. Wang, Z. Hui, K. Mayilvahanan, K. J. Takeuchi, A. C. Marschilok, A. C. West, E. S. Takeuchi, and G. Yu, *Advanced Materials,* **33** (26), 2101275 (2021).

91. V. Srinivasan and J. Newman, *Journal of The Electrochemical Society,* **151** (10), A1530 (2004).

92. J. F. M. Oudenhoven, L. Baggetto, and P. H. L. Notten, *Advanced Energy Materials,* **1** (1), 10 (2011).

93. R. Zhao, J. Liu, and J. Gu, *Applied Energy,* **139** 220 (2015).

94. J. Billaud, F. Bouville, T. Magrini, C. Villevieille, and A. R. Studart, *Nature Energy,* **1** (8), 16097 (2016).

95. Y. Zhu, Z. Ju, X. Zhang, D. M. Lutz, L. M. Housel, Y. Zhou, K. J. Takeuchi, E. S. Takeuchi, A. C. Marschilok, and G. Yu, *Advanced Materials,* **32** (10), 1907941 (2020).

96. L. Li, R. M. Erb, J. Wang, J. Wang, and Y.-M. Chiang, *Advanced Energy Materials,* **9** (2), 1802472 (2019).

97. L.-L. Lu, Y.-Y. Lu, Z.-J. Xiao, T.-W. Zhang, F. Zhou, T. Ma, Y. Ni, H.-B. Yao, S.-H. Yu, and Y. Cui, *Advanced Materials,* **30** (20), 1706745 (2018).

98. W. Mai, F. L. E. Usseglio-Viretta, A. M. Colclasure, and K. Smith, *Electrochimica Acta,* **341** 136013 (2020).

99. Z. Hui, K. S. Mayilvahanan, K. Ganko, Y. Yang, X. Zhang, Z. Ju, K. J. Takeuchi, A. C. Marschilok, G. Yu, E. Takeuchi, and A. C. West, *Energy Storage Materials,* **39** 176 (2021).

100. F. L. E. Usseglio-Viretta, W. Mai, A. M. Colclasure, M. Doeff, E. Yi, and K. Smith, *Electrochimica Acta,* **342** 136034 (2020).

101. K. S. Mayilvahanan, Z. Hui, K. Hu, J. Kuang, A. H. McCarthy, J. C. Bernard, L. Wang, K. Takeuchi, A. Marschilok, E. Takeuchi, and A. C. West, *Journal of The Electrochemical Society,* (2021).

102. J. Wang, J. K. Carson, M. F. North, and D. J. Cleland, *International Journal of Heat and Mass Transfer,* **49** (17), 3075 (2006).

103. Y. K. Lee, *Energies,* **12** (4), (2019).

104. S. Hidayat, T. Cahyono, J. Y. Mindara, N. Riveli, W. Alamsyah, and I. Rahayu, *IOP Conference Series: Materials Science and Engineering,* **196** 012035 (2017).

105. Y. Zhu, L. Peng, D. Chen, and G. Yu, *Nano Letters,* **16** (1), 742 (2016).

106. Z. P. Cano, D. Banham, S. Ye, A. Hintennach, J. Lu, M. Fowler, and Z. Chen, *Nature Energy,* **3** (4), 279 (2018).

107. G. Crabtree, *Science,* **366** (6464), 422 (2019).

108. J. Liu, Z. Bao, Y. Cui, E. J. Dufek, J. B. Goodenough, P. Khalifah, Q. Li, B. Y. Liaw, P. Liu, A. Manthiram, Y. S. Meng, V. R. Subramanian, M. F. Toney, V. V. Viswanathan, M. S. Whittingham, J. Xiao, W. Xu, J. Yang, X.-Q. Yang, and J.-G. Zhang, *Nature Energy,* **4** (3), 180 (2019).

109. K. Liu, Y. Liu, D. Lin, A. Pei, and Y. Cui, *Science Advances,* **4** (6), eaas9820 (2018).

110. P. Sun, R. Bisschop, H. Niu, and X. Huang, *Fire Technology,* **56** (4), 1361 (2020).

111. X. Han, L. Lu, Y. Zheng, X. Feng, Z. Li, J. Li, and M. Ouyang, *eTransportation,* **1** 100005 (2019).

112. A. Barré, B. Deguilhem, S. Grolleau, M. Gérard, F. Suard, and D. Riu, *Journal of Power Sources,* **241** 680 (2013).

113. D. Lin, Y. Liu, and Y. Cui, *Nature Nanotechnology,* **12** (3), 194 (2017).

114. S. Chen, J. Zheng, D. Mei, K. S. Han, M. H. Engelhard, W. Zhao, W. Xu, J. Liu, and J.-G. Zhang, *Advanced Materials,* **30** (21), 1706102 (2018).

115. W. Liu, P. Liu, and D. Mitlin, *Advanced Energy Materials,* **10** (43), 2002297 (2020).

116. J.-L. Shi, D.-D. Xiao, M. Ge, X. Yu, Y. Chu, X. Huang, X.-D. Zhang, Y.-X. Yin, X.-Q. Yang, Y.-G. Guo, L. Gu, and L.-J. Wan, *Advanced Materials,* **30** (9), 1705575 (2018).

117. A. Manthiram, K. Chemelewski, and E.-S. Lee, *Energy & Environmental Science,* **7** (4), 1339 (2014).

118. X. Ren, L. Zou, X. Cao, M. H. Engelhard, W. Liu, S. D. Burton, H. Lee, C. Niu, B. E. Matthews, Z. Zhu, C. Wang, B. W. Arey, J. Xiao, J. Liu, J.-G. Zhang, and W. Xu, *Joule,* **3** (7), 1662 (2019).

119. X. Li, J. Liu, M. N. Banis, A. Lushington, R. Li, M. Cai, and X. Sun, *Energy &*

Environmental Science, **7** (2), 768 (2014).

120. X. Dong, J. Yao, W. Zhu, X. Huang, X. Kuai, J. Tang, X. Li, S. Dai, L. Shen, R. Yang, L. Gao, and J. Zhao, *Journal of Materials Chemistry A,* **7** (35), 20262 (2019).

121. J. Zhu and G. Chen, *Journal of Materials Chemistry A,* **7** (10), 5463 (2019).

122. F. Lin, I. M. Markus, D. Nordlund, T.-C. Weng, M. D. Asta, H. L. Xin, and M. M. Doeff, *Nature Communications,* **5** (1), 3529 (2014).

123. W. Li, A. Dolocan, P. Oh, H. Celio, S. Park, J. Cho, and A. Manthiram, *Nature Communications,* **8** (1), 14589 (2017).

124. T. M. M. Heenan, A. Wade, C. Tan, J. E. Parker, D. Matras, A. S. Leach, J. B. Robinson, A. Llewellyn, A. Dimitrijevic, R. Jervis, P. D. Quinn, D. J. L. Brett, and P. R. Shearing, *Advanced Energy Materials,* **10** (47), 2002655 (2020).

125. C. D. Quilty, G. P. Wheeler, L. Wang, A. H. McCarthy, S. Yan, K. R. Tallman, M. R. Dunkin, X. Tong, S. Ehrlich, L. Ma, K. J. Takeuchi, E. S. Takeuchi, D. C. Bock, and A. C. Marschilok, *ACS Applied Materials & Interfaces,* **13** (43), 50920 (2021).

126. Y. Mao, X. Wang, S. Xia, K. Zhang, C. Wei, S. Bak, Z. Shadike, X. Liu, Y. Yang, R. Xu, P. Pianetta, S. Ermon, E. Stavitski, K. Zhao, Z. Xu, F. Lin, X.-Q. Yang, E. Hu, and Y. Liu, *Advanced Functional Materials,* **29** (18), 1900247 (2019).

127. W. Li, B. Song, and A. Manthiram, *Chemical Society Reviews,* **46** (10), 3006 (2017).

128. Y. Li, C. Zou, M. Berecibar, E. Nanini-Maury, J. C. W. Chan, P. van den Bossche, J. Van Mierlo, and N. Omar, *Applied Energy,* **232** 197 (2018).

129. Y. Deng, H. Ying, J. E, H. Zhu, K. Wei, J. Chen, F. Zhang, and G. Liao, *Energy,* **176** 91 (2019).

130. K. Liu, Y. Shang, Q. Ouyang, and W. D. Widanage, *IEEE Transactions on Industrial*

Electronics, **68** (4), 3170 (2021).

131. K. A. Severson, P. M. Attia, N. Jin, N. Perkins, B. Jiang, Z. Yang, M. H. Chen, M. Aykol, P. K. Herring, D. Fraggedakis, M. Z. Bazant, S. J. Harris, W. C. Chueh, and R. D. Braatz, *Nature Energy,* **4** (5), 383 (2019).

132. Y. Zhang, Q. Tang, Y. Zhang, J. Wang, U. Stimming, and A. A. Lee, *Nature Communications,* **11** (1), 1706 (2020).

133. K. S. Mayilvahanan, K. J. Takeuchi, E. S. Takeuchi, A. C. Marschilok, and A. C. West, *Batteries & Supercaps,* **5** (1), e202100166 (2022).

134. C. R. Birkl, M. R. Roberts, E. McTurk, P. G. Bruce, and D. A. Howey, *Journal of Power Sources,* **341** 373 (2017).

135. K. S. Mayilvahanan, J. Kuang, A. H. McCarthy, L. Wang, K. J. Takeuchi, A. M. Marschilok, E. S. Takeuchi, and A. C. West, *Journal of The Electrochemical Society,* **168** (5), 050525 (2021).

136. J. Wandt, A. Freiberg, R. Thomas, Y. Gorlin, A. Siebel, R. Jung, H. A. Gasteiger, and M. Tromp, *Journal of Materials Chemistry A,* **4** (47), 18300 (2016).

137. T. Joshi, K. Eom, G. Yushin, and T. F. Fuller, *Journal of The Electrochemical Society,* **161** (12), A1915 (2014).